Synthesis of Multi-Layer Frequency Selective Surfaces for Quasi-Optical Systems

by

Loo, Pak Kwan
Submitted for the degree of Doctor of Philosophy

Heriot-Watt University
School of Engineering and Physical Science
June 2020

ABSTRACT

This thesis investigate design techniques for multilayer Frequency Selective Surfaces (FSS) and its applications in quasi-optical (QO) systems. Design challenges that involve higher order filter and practical implementation of multilayer FSS at higher frequencies are reviewed. Multilayer FSS structures are commonly realized by cascading two or more FSS panel to achieve higher order responses, which usually rely on dielectric substrates to support the FSS arrays. It is noted that existing design approaches involved elaborate manufacturing processes as well as the requirement of custom dielectric thickness for the implementation of multilayer FSS. These design issues poses practical problems in the realization of multilayer FSS of higher order and its demonstration at higher frequencies. Furthermore, realization of higher order multilayer FSS with custom dielectric thicknesses are not feasible with low cost Printed Circuit Board (PCB) technology. As a result of this investigation, a novel design and synthesis technique is developed to address the aforementioned design issues. Equivalent circuit modelling and full wave electromagnetic simulation are employed for this purpose. The developed design technique enable practical realization of QO filter to have all transmission lines of predefined fix length. As a result, the proposed technique is able to resolve the limited availability of custom dielectric thicknesses, thus enable demonstration of multilayer FSS of higher order at higher frequencies. Particularly, the proposed design methodology allow rectification by design to adapt to any small variations in the dielectric thicknesses. Subsequently, based on this technique, a novel QO reflector design is developed to demonstrate proof of concept for time delay multiplexing that are employed in a radar system. The implementation of time delay between two polarization multiplexed beams initially requires true time delay structures that are difficult to integrate due to their electrically large structure. In order to address this problem, the designed QO reflector is able to perform same functionalities, i.e. a significant group delay difference for the two orthogonal linear polarization. Specifically, the designed QO reflector has the capability to de-multiplex an incoming wave into two linear polarized waves, whereby one of the reflected wave is time delayed while the other wave is unaffected. A synthesis method for QO reflector design with time delay multiplexing has been presented. Based on the design procedures reported in this thesis, prototypes for both QO filter and QO reflector of fourth order has been developed to operate at 15 GHz with 5% and 3.5% bandwidth respectively. The performances of the developed prototypes are verified with free-space measurement setup. The measured insertion loss of the QO filter is observed to be in the

range of 0.5 dB – 2.83 dB, while the measured return loss of the QO reflector is the range of 1.5 dB – 2.3 dB. In order to demonstrate the effect of the group delay from the QO reflector, frequency domain analysis is performed by post-processing the measured data to obtain the required time domain signals. Overall the experimental measurement results corroborate well with both full-wave and circuit simulation.

ACKNOWLEDGEMENTS

I wish to firstly thank my supervisor Professor Dr George Goussetis for taking me in as his PhD student as well as his advice and support leading up to the completion of this research. Thank you for your kindness and patience, I would be lost without your guidance and motivation. I would also like to thank my second supervisor, Dr Carolina Mateo Segura.

I would like to thank Dr Tang Wen Xing for his kind assistance in measurement setup and for the many fruitful discussions that we had. I would also like to thank Dr Maria Lorente Crespo, for her kind advice during my short stay in Herriot Watt UK. I wish to also extend my gratitude to the laboratory staff at HW UK for the guidance given as well as assistance in fabricating the prototypes for testing.

I would like to thank my alma mater and now employer, Tunku Abdul Rahman University College for funding my PhD at HW UK and to my colleagues and friends in TAR UC who are supportive of my post graduate studies.

To Ivan, for his humour and friendship. Last but certainly not the least, I wish to thank Lexie, Nami, and especially my wife, Li Li for her kind understanding, support, and patience throughout this journey.

Research Thesis Submission

Please note this form should be bound into the submitted thesis.

Name:	LOO, PAK KWAN		
School:	Engineering and Physical Sciences		
Version: *(i.e. First, Resubmission, Final)*	Final	Degree Sought:	PhD. Electrical and Electronics Engineering

Declaration

In accordance with the appropriate regulations I hereby submit my thesis and I declare that:

1. The thesis embodies the results of my own work and has been composed by myself
2. Where appropriate, I have made acknowledgement of the work of others
3. The thesis is the correct version for submission and is the same version as any electronic versions submitted*.
4. My thesis for the award referred to, deposited in the Heriot-Watt University Library, should be made available for loan or photocopying and be available via the Institutional Repository, subject to such conditions as the Librarian may require
5. I understand that as a student of the University I am required to abide by the Regulations of the University and to conform to its discipline.
6. I confirm that the thesis has been verified against plagiarism via an approved plagiarism detection application e.g. Turnitin.

ONLY for submissions including published works

Please note you are only required to complete the Inclusion of Published Works Form (page 2) if your thesis contains published works)

7. Where the thesis contains published outputs under Regulation 6 (9.1.2) or Regulation 43 (9) these are accompanied by a critical review which accurately describes my contribution to the research and, for multi-author outputs, a signed declaration indicating the contribution of each author (complete)
8. Inclusion of published outputs under Regulation 6 (9.1.2) or Regulation 43 (9) shall not constitute plagiarism.

* *Please note that it is the responsibility of the candidate to ensure that the correct version of the thesis is submitted.*

Signature of Candidate:		Date:	01/07/2020

Submission

Submitted By *(name in capitals):*	LOO, PAK KWAN
Signature of Individual Submitting:	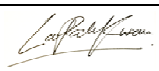
Date Submitted:	

For Completion in the Student Service Centre (SSC)

Limited Access	Requested	Yes		No		Approved	Yes		No	
*E-thesis Submitted (**mandatory for final theses**)*										
Received in the SSC by *(name in capitals):*						Date:				

Inclusion of Published Works

Please note you are only required to complete the Inclusion of Published Works Form if your thesis contains published works under Regulation 6 (9.1.2)

Declaration

This thesis contains one or more multi-author published works. In accordance with Regulation 6 (9.1.2) I hereby declare that the contributions of each author to these publications is as follows:

Citation details	Pak Kwan Loo and George Goussetis, "Asymmetrical Impedance Inverter for Quasi-Optical Bandpass Filters With Transmission Lines of Fixed Length," IEEE Transactions on Microwave Theory and Techniques, Volume: 66, Issue: 11 , Nov. 2018, DOI: 10.1109/TMTT.2018.2873396
Author 1	• Review of previous & existing FSS design • Development of design methodologies • Prototyping • Experimental setup & measurement • Drafting of manuscript and editing
Author 2	• Technical content advisor and final manuscript editing
Signature:	
Date:	01/07/2020

TABLE OF CONTENTS

ACKNOWLEDGEMENTS i
TABLE OF CONTENTS ii
LISTS OF FIGURES iv
LISTS OF TABLES viii
Chapter 1 : Introduction 9
1.1 Introduction to Frequency Selective Surfaces 9
1.2 Motivation 10
1.2.1 Higher Order FSS Filter 11
1.2.2 Quasi Optical Imaging System 11
1.3 Scope of thesis and its content 12
1.4 Research papers produced during working on this thesis 14
Chapter 2 : Multilayer Frequency Selective Surfaces Literature Reviews 15
2.1 Introduction 15
2.2 FSS Based Aperture-Coupled Resonator Structure 16
2.2.1 A FSS using aperture-coupled microstrip patches 16
2.2.2 Antenna–Filter–Antenna Arrays as a Class of Bandpass FSS 19
2.2.3 Design and Analysis of a High-Selectivity Frequency-Selective Surface at 60 GHz 23
2.3 Bandpass Filter Based Miniaturized Element Frequency Selective Surfaces (MEFSS) 28
2.3.1 A Generalized Method for Synthesizing Low-Profile, Band-Pass Frequency Selective Surfaces with Non-Resonant Constituting Elements 29
2.3.2 Inductively-Coupled Miniaturized-Element Frequency Selective Surfaces With Narrowband, High-Order Bandpass Responses 32
2.4 Summary 35
Chapter 3 : Modelling and Analysis of Frequency Selective Surfaces 36
3.1 Introduction 36
3.2 Electric and Magnetic Field Integral Equations (EFIE & MFIE) Formulation 38
3.2.1 Electric Field Integral Equation (EFIE) Formulation 39
3.2.2 Magnetic Field Integral Equation (MFIE) Formulation 41
3.2.3 Method of Moment Solution 42
3.3 Generalized Scattering Matrix (GSM) 44
3.4 Numerical Results & Validation 46
3.5 Filter Theory for Multilayer FSS Design 49
3.5.1 Low-Pass Prototype (LPP) Filter 50
3.5.2 Coupled Resonator Filter with Immittance Inverter 52
3.5.3 Practical Realization of Immittance Inverter 56
3.6 Summary 58

Chapter 4 : Asymmetrical Impedance Inverter for Quasi-Optical Bandpass Filter with Transmission Lines of Fixed Length 59
4.1 Introduction 59
4.2 Theory 62
4.2.1 Definition of the Problem 62
4.2.2 Principles of the Proposed Solution 65
4.2.3 Analysis of the proposed Inverter 66
4.3 Design Examples and Validation of Experimental Result. 68
4.3.1 Design Procedure 69
4.3.2 Numerical and Experimental Results 72
4.4 Summary 76
Chapter 5 : Design of Quasi-Optical Reflector with Customizable Group Delay 77
5.1 Introduction 77
5.2 Operating Principles and Design Procedures 79
5.2.1 Operating Principles 80
5.2.2 Prototype Synthesis Procedure 81
5.2.3 Implementation of Impedance Inverter 84
5.3 Design Examples and Validation of Measurement Results 86
5.3.1 Prototype Design 86
5.3.2 Prototype Implementation 90
5.4 Summary 96
Chapter 6 : Conclusion 97
6.1 Conclusion and Summary of Results 97
6.2 Future Work 99
Appendix A: Electromagnetics Theory for Periodic Surfaces 100
A1: Overview on Maxwell's Equations and Wave Equation 100
A2: Floquet's Theorem and Space Harmonics 102
A3: Modal Field Solution for Two Dimensional Periodic Array 103
A4: Floquet Expansion for Two Dimensional Periodic Array 105
A4.1:TM Modes 107
A4.2: TE Modes 108
Appendix B: Generalized Scattering Matrix (GSM) for Multilayer FSS 110
B1: GSM Cascading Rule 110
B2: Building Blocks for GSM Analysis 112
B2.1: FSS Array 112
B2.2: Dielectric Layer 115
B2.3: Dielectric Interface 116
References 119

LISTS OF FIGURES

Figure 1.1: A conceptual depiction of a capacitive FSS and its frequency response. 10
Figure 1.2: Photograph of the radar system that involved the long quasi-optical waveguide [6]..... 12
Figure 2.1 Geometrical layout of the developed FSS in [33] (a) Top view (b) Side view 17
Figure 2.2 Variation of the frequency response of the FSS with slot length. (L_p = W_p = 17.1 mm, W_s = 0.5 mm, ε_r, = 2.33, d = 1.6 mm,and a = b = 28.3 mm.) [33] 17
Figure 2.3 Variation of the frequency response of the FSS with substrate thickness. (Lp = Wp = 17.1 mm, Ws = 0.5 mm, εr, = 2.33, d = 1.6 mm,and a = b = 28.3 mm.) [33] 18
Figure 2.4 AFA array composed of radiative patch antenna and CPW resonators [34]..... 19
Figure 2.5 Type-I FSS. (a) Unit cell arrangement. (b) Equivalent circuit [34] 20
Figure 2.6 Transmission and reflection coefficients of the Type-I FSS for normal incidence with horizontal polarization [34]..... 20
Figure 2.7 Type-II FSS. (a) Unit cell arrangement (b) Equivalent circuit [34]. 21
Figure 2.8 Transmission and reflection coefficients of Type-II FSS for normal incidence with horizontal polarization [34]..... 22
Figure 2.9 Isometric view of the proposed FSS unit cell [39]..... 23
Figure 2.10 (a) Equivalent-circuit model of the aperture coupled FSS. (b) Simplified equivalent circuit model excluding the mutual inductance Lm1 and the mutual capacitance Cm1. (c) Even-mode circuit. (d) Odd-mode circuit. [39]..... 24
Figure 2.11 Effects of the locations of the coupling apertures on the: (a) simulated overall coupling coefficient k and (b) simulated transmission response of the proposed 60-GHz ACR FSS [39]. 26
Figure 2.12 Comparison results between the measured results and the simulated results obtained by the full-wave EM simulation and the circuit simulation at normal incidence. (a) Transmission response. (b) Reflection response [39]..... 27
Figure 2.13 Topology of the first order bandpass FSS formed by arrays of capacitive patches and inductive grid separated by a dielectric substrate. (a) 3-D view and (b) side view [43]..... 28
Figure 2.14: (a) Exploded view of the proposed FSS topology comprises of successive stacked arrays and dielectric substrates. (b) Side view of the proposed FSS structure. (c) Unit cell of the FSS [46]. 29
Figure 2.15: (a) Equivalent circuit model of the general FSS shown in Figure 2.14(a) for normal angle of incidence. (b) Transmission lines in (a) are replaced by their simple LC equivalent network. (c) Further simplification in (b) by neglecting parasitic capacitances adjacent to inductor wire grid. (d) Inductor coupled bandpass network after T to π transformation from (c) [46]..... 30
Figure 2.16 Reflection and transmission coefficients of the band-pass FSS. Simulation results in HFSS and theoretically predicted ones are compared with the measurement results [46]. 31
Figure 2.17: Generalize structure of the proposed bandpass FSS of N^{th} order filter response, comprises of N dielectric resonator layers and N+1 array layers [38]..... 32
Figure 2.18: Unit cell structure of the proposed 2^{nd} order bandpass FSS with two identical inductive grids introduced in the center to restore the symmetry of the structure. The two wire grid at the center are separated by a bonding layer [38]. 34
Figure 2.19: Comparison between simulations results (circuit and full-wave) with experimental free space measurement [38]..... 34

Figure 3.1 Side profile of the two-dimensional periodic planar array resides at z = 0. 38
Figure 3.2 (a) Exploded view of a three-layer array structure. (b) Two-port network representation of each layer and its entire structure [59]..... 45
Figure 3.3: (a) The geometrical unit cell dimension of the capacitive dipole FSS. The conducting element is represented by yellow region, while blue region denote the vacuum. (b) Reflection & transmission frequency response of fundamental mode due to normal incident plane wave polarized in y-direction, i.e. $Ei = yEy$ at spherical angles $\theta = 0°$ and $\phi = 0°$. 46
Figure 3.4: (a) The geometrical unit cell dimension of the inductive dipole FSS. The conducting element is represented by yellow region, while blue region denote the vacuum. (b) Reflection & transmission coefficient of the fundamental mode due to normal incident plane wave polarized in x-direction, i.e. $Ei = xEx$ at spherical angles $\theta = 0°$ and $\phi = 0°$. 47
Figure 3.5: (a) The geometrical unit cell dimension of the capacitive dipole FSS. The conducting element is represented by yellow region, while brown region denote the dielectric substrate. (b) Reflection & transmission frequency response of fundamental mode due to normal incident plane wave polarized in y-direction, i.e. $Ei = yEy$ at spherical angles $\theta = 0°$ and $\phi = 0°$. 48
Figure 3.6: (a) The geometrical dimensions of the complementary FSS consist of dipole patch and slot that are printed on both side of a substrate. The conducting element is represented by yellow region, while brown region denote the dielectric substrate. (b) Reflection & transmission coefficient of the fundamental mode due to normal incident plane wave polarized in y-direction, i.e. $Ei = yEy$ at spherical angles $\theta = 0°$ and $\phi = 0°$..... 49
Figure 3.7 Low-pass prototype ladder network. (a) With first element shunt capacitor after the source resistor, g_0. (b) With first element series inductor after the source resistor, g_0 [47]. 51
Figure 3.8 Classical lumped element bandpass filter 52
Figure 3.9 (a) Application of impedance inverter to convert a series inductor to a shunt capacitor. (b) Application of admittance inverter to convert a shunt capacitor to series inductor [45]. 53
Figure 3.10 (a) Bandpass filter consist only series resonators with impedance inverters (b) Bandpass filter consist only parallel resonators with admittance inverters [45]. 54
Figure 3.11 Generalized resonator coupled bandpass filter (a) with impedance inverter (b) with admittance inverter [45]. 55
Figure 3.12 Lumped element inverters [64] 57
Figure 3.13 Coupled resonator circuits realized by lumped element inverters [64]. 57
Figure 3.14 Mixed lumped and distributed element immittance inverters [45]. 58
Figure 4.1 General topology of quasi-optical filters comprises of multilayer stacked two dimensional periodic surfaces..... 59
Figure 4.2 Generalized impedance inverter (K-inverter) structure with series coupled-resonator bandpass filter circuit..... 61
Figure 4.3 (a) Equivalent circuit for a typical impedance inverter involving a shunt suscptance between transmission lines of a given electrical length. (b) Bandpass filter network exploiting the impedance inverter of Fig. 3(a). Note that the i^{th} resonators absorb electrical lengths associated with impedance inverters $Ki - 1, i$ and $Ki, i + 1$ and hence has electrical length αi. 63

Figure 4.4 Graphical representation for a range of attainable numerical values for the normalized impedance inverter, K/Z_s and phase, ϕ of the classical impedance inverter in Fig. 3(a) for different value of normalized susceptance, B/Y_S. 63
Figure 4.5 (a) The proposed asymmetrical impedance inverter consists of transmission line with electrical length, ϕ_l and susceptance of Y_p and Y_q that can be implemented using either lumped capacitor or inductor. (b) Bandpass filter network using proposed asymmetrical impedance inverter where now all resonators have the same length as all resonators are absorbing a constant phase. Note also that ϕ_l is constant for all impedance inverters. 64
Figure 4.6 Color-map and the contour lines represent the normalized impedance inverter and phases of ϕ_p and ϕ_q respectively for the range of susceptance values assigned to Y_p and Y_q. 68
Figure 4.7 Contour of ϕp and ϕq for specific normalized impedance inverter values. 70
Figure 4.8 Contour lines for specific normalized impedance inverter values and selected phase of ϕ_p and ϕ_q based on Figure 4.6. 71
Figure 4.9 (a) FSS unit cell for inductive grids. (b) FSS unit cell capacitive grids. 73
Figure 4.10 Side view of the fourth order bandpass FSS filter depicting relative position of the FSS array, substrate and spacer resonator. 73
Figure 4.11 Photograph of the fabricated 4th order QO bandpass filter prototype. The inset shows a zoomed area of the first layer array. 74
Figure 4.12 (a) Photograph of the measurement setup to characterize the transmission coefficient, S_{21} of the 4th order QO bandpass filter, where the prototype is positioned at the window opening between the transmit and received antennas. (b) Side view of the measurement setup illustrating the relative position of the transmit and received antennas. 75
Figure 4.13 Comparison between measured results of the fourth-order prototype with full-wave and circuit simulation for (a) TE polarization. (b) TM polarization. 75
Figure 5.1 Schematic diagram representation of the multiplexing standoff radar system in [41] with proposed replacement using quasi-optical reflector 78
Figure 5.2 Illustration of a reflector surface. An incident of electric field composed of a Gaussian pulse tilted at an angle, γ with respect to y direction. The reflected field decomposes into vertical and horizontal polarization field, where the vertical Gaussian pulse is delay by some amount of time with respect to the incident pulse. 79
Figure 5.3 (a) Generalized one port series coupled resonator bandpass filter equivalent circuit model. (b) Single port canonical low-pass network (c) Bandpass circuit via frequency transformation of the low-pass network in (b). 81
Figure 5.4 (a) Proposed asymmetrical impedance inverter comprises of a transmission line with electrical length η and susceptance of YU and YV that can be implemented using either lumped capacitor or inductor. (b) One port reflector network using the proposed asymmetrical impedance inverter, where now all resonators have the same length as all resonators are absorbing a constant phase, δ. Also, note that η is constant for all impedance inverters. 85
Figure 5.5 Comparison between the prescribed phase and the phases of the first four order of the generated Hurwitz polynomial. 87
Figure 5.6 Comparison of phase and group delay responses between LPP circuit and prescribed equations. 88

Figure 5.7 Contour lines for specific normalized impedance inverter values and selected phases of ψL and ψR. 89
Figure 5.8 Comparison between phase and group delay responses between L-C and distributed bandpass (BP) circuit simulation. 90
Figure 5.9 (a) FSS unit cell for inductive grids. (b) FSS unit cell capacitive grids. 91
Figure 5.10 Side view of the fourth order bandpass FSS filter depicting relative position of the FSS array, substrate and spacer resonator. 92
Figure 5.11 (a) Measurement setup (b) Photograph of the fabricated fourth-order reflector prototype. Inset: zoomed area of the first-layer. 93
Figure 5.12 Comparison between measured (M) results of the fourth-order reflector prototype with full-wave (F) and circuit simulation (Circ) for both Vertical (V) and Horizontal (H) polarization. (a) Magnitude (b) Phases (degree) (c) Group delay 95
Figure 5.13 Time domain representation of the reflected output measured (M) results and full-wave (F) for both Vertical (V) and Horizontal (H) polarization of the fourth-order reflector prototype for an Incident (Inc) Gaussian pulse. 95
Figure A.1Arbitrary periodic array between two distinct media 103
Figure A.2: Periodic array of arbitrary lattice arrangement 106
Figure B.1: Incident, reflected, and transmitted voltage vectors of two cascaded layers [59]. 111
Figure B.2: Travelling waves did not undergo any changes in a dielectric layer of thickness *d*, thus the propagating modes suffer a phase delay only, while evanescent modes are attenuated [59]. 115
Figure B.3: Incident and reflected voltage vectors at the interface of two dielectric medium [59] 117

LISTS OF TABLES

Table 2.1: Tuned Inductances for 2nd Order Bandpass Filter Design with Substrate Thickness 1.9mm Implemented in [38] 33
Table 3.1: Comparison of Computational Time 48
Table 3.2: Summary of Prototype Filter Transformations $\Delta = \omega 2 - \omega 1 \omega 0$ [47] 51
Table 4.1 Computed Phases of Φ_P and Φ_Q 71
Table 4.2 Susceptance Values For Fourth-Order Filter 71
Table 4.3 Circuits Parameters and Geometrical Dimensions for Fourth-Order Filter 73
Table 5.1 Computed Phases of ψU and ψV 89
Table 5.2 Susceptance Values For The Asymmetrical Impedance Inverter 90
Table 5.3 Circuits Parameters and Geometrical Dimensions for Fourth-Order Reflector 92

Chapter 1: **Introduction**

1.1 **Introduction to Frequency Selective Surfaces**

In contrast to radio frequency systems relying on transmission lines and guided waves, quasi-optical systems typically involve on electromagnetic waves propagating in free space. [1]. These architectures are commonly employed in the fields of radio astronomy [2], remote sensing [3], [4] radar [5], [6] terrestrial and satellite telecommunications as well as plasma diagnostics [7], [8] and utilize an antenna to collect radiation over a frequency range from the environment. Periodic electromagnetic structures and Frequency Selective Surfaces (FSS) can play a significant role in such systems, e.g. in de-multiplexing the beams in e.g. polarisation or frequency [9], [10].

FSS are two dimensional periodic planar array that can be realized with printed conducting elements on dielectric substrate (patch type) or perforated geometries on conducting plane (aperture type). These elements can be periodically arranged in arbitrary lattice geometry, in e.g. a square or triangular lattice. FSS are commonly used as spatial filters due to their ability to modify the spectral content for an incident of propagating electromagnetic (EM) wave. Their spectral response can depend not only on frequency but also the polarization and angle of incident of an EM wave [11]. Specifically, when a FSS is exposed to an illumination of EM waves, currents are induced on the array elements. Consequently, these elements behave as an EM sources and generate scattered fields by virtue of the induced currents [11]. Therefore, the resulting fields in the vicinity of the FSS constitute both the incident and scattered EM waves. In view of this, the desired polarization and direction of the scattered fields as well as the spectral responses can be engineered by designing appropriately the array elements together with proper selection of substrate material.

In a broader context, periodic structures used to scatter electromagnetic waves can be classified to two broad categories depending on whether they involve non-resonant or resonant elements. Examples of non-resonant arrays are inductive or capacitive grids [12] and meshes [13]. Inductive grids function as a high-pass filter when the geometry of the grid is oriented parallel to the incident electric field, while capacitive grids perform like

a low-pass filter when the orientation of the grid is perpendicular with respect to polarization incident electric field. On the other hand, FSS typically comprise resonant elements; examples that have been conventionally employed and extensively studied are dipoles [14]–[16] and other variants such as cross-dipoles [17]–[19], tri-poles [20]–[22], square [23]–[25] and circular ring [26]–[28]. FSS comprising double periodic arrays of electrically isolated conducting elements (inductive arrays) perform as reflecting surface at resonance, while FSS arrays of apertures in otherwise connected metallic surface behave as transparent surface at its resonant frequency for an incoming EM wave. Thus at resonance, the conductive element and aperture array FSS depict characteristics of bandstop and bandpass response respectively. The typical frequency response of a capacitive FSS is depicted in Figure 1.1, which illustrates a free standing FSS of arbitrary periodic elements and its frequency response.

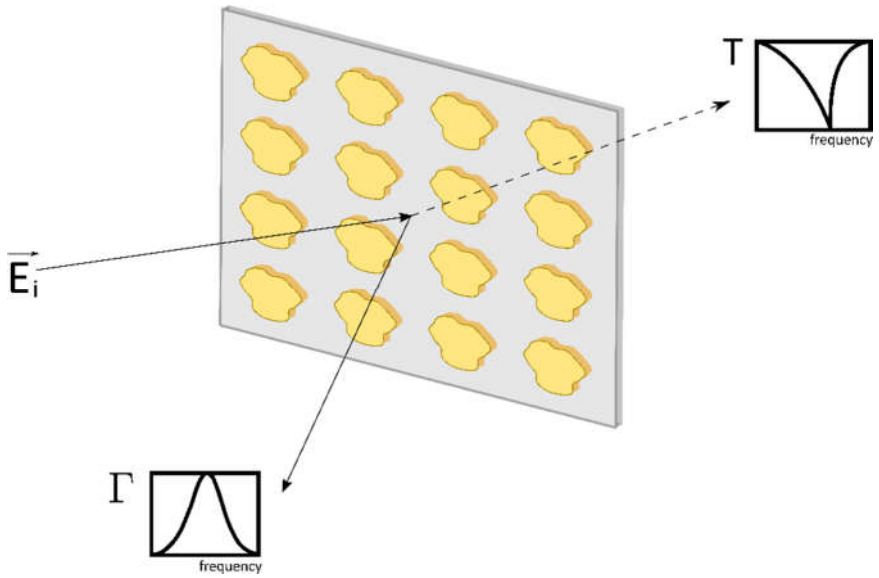

Figure 1.1: A conceptual depiction of a capacitive FSS and its frequency response.

1.2 **Motivation**

The motivation of this thesis is to develop efficient synthesis techniques for multilayer periodic electromagnetic structures that are designed to simplify the implementation of quasi-optical systems. In this respect the research has focused on two particular aspects:

1.2.1 Higher Order FSS Filter

The frequency characteristic of a single planar resonant FSS resemble those of a first order bandpass or bandstop filter response depending on the type of FSS elements. Traditionally, higher order filter can be realized by cascading multiple single planar resonant FSS to tailor desired frequency responses [29], [30]. In particular, to improve the bandwidth and roll-off rate of the filter response [31], [32]. While, classical filter theory enable higher order filter design by means of cascading successive single resonant FSS with quarter wavelength spacer [11]. The quarter wavelength separation functions as an admittance inverter that allow controlled coupling between the resonator elements. Other alternative design for higher order FSS filter based on coupled resonator method has been proposed in several frameworks [33]–[39]. While, these existing design approaches may lead to electrically acceptable responses, however there are still many challenges remain unsolved in particular in the aspect of design strategy and practical realizations of higher order FSS filter particularly at higher frequencies. For example, existing strategies may require e.g. dielectric spacers of custom thickness that may not be readily available. Addressing this requirement, the work carried out in this research focuses on exploiting design approaches that simplify the realization of FSSs exploiting predefined dielectric substrates.

1.2.2 Quasi Optical Imaging System

Recently, radar imaging systems developed by Jet Propulsion Laboratory [5], [6], [40]–[42] have demonstrated two approaches to increase the radar frame rate with the aim to improve the quality of the scanned images and also enable wider imaging area. One of the method is based on fast scanning optics that depends on motor acceleration and high speed galvanometers. However, the aforementioned implementation is not cost effective [41]. Moreover, increasing the scanning speed also causes the reduction of dwell time per image pixel and consequently, the quality of the scanned images are jeopardized. While the other method exploit time delay two beam multiplexing to double the radar frame rate. This can be achieved by splitting a linear polarized beam into two components by means a of beam splitter. One of the components propagate through the wire grid unimpeded, while the other component experiences a time delay before recombine with the unimpeded component. Despite the advantages of the proposed architecture in [6], its implementation involves a long optical path for one polarization, as illustrated in Figure

1.2. This has been achieved by an assembly of reflectors and true time delay optical paths in [40]. Consequently, the compact integration of such system becomes cumbersome. Therefore, the subsequent research work utilizes the design strategy mentioned above to address these challenges.

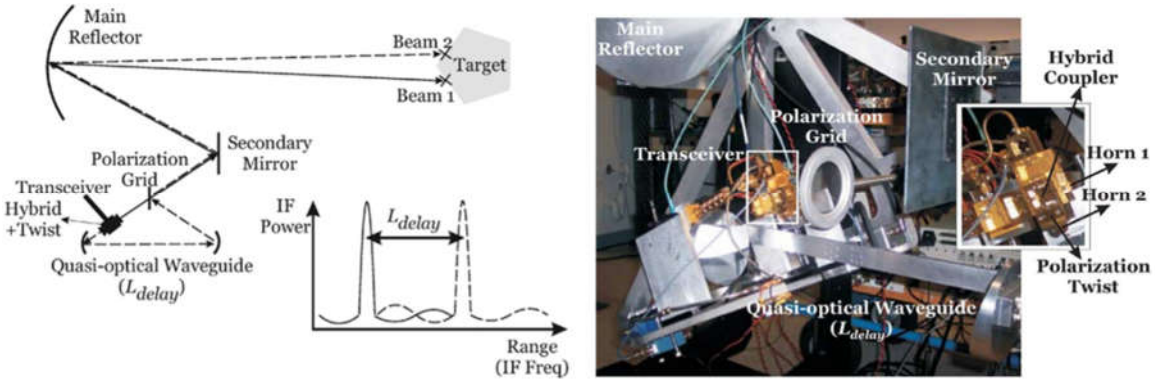

Figure 1.2: Photograph of the radar system that involved the long quasi-optical waveguide [6].

1.3 Scope of thesis and its content

As reviewed in the previous sections, the objective of this research work is to develop and progress the current state of art in quasi-optical filters by addressing the existing design drawbacks. The subsequent chapters entail the studies and synthesis development for multilayer quasi-optical filter. A brief overview of each chapter is as follows:

Chapter 1: Introduction

The present chapter provides a top level introduction into the area where this PhD thesis has focused and motivation of the work performed.

Chapter 2: Literature Review

This chapter present a review of existing framework of multilayer FSS synthesis and design that are relevant to this research. In particular, the resonator coupled filter topology is the focus in this chapter.

Chapter 3: Analysis and Modelling of Frequency Selective Surfaces

This chapter provides some background theory that has been implemented during this work to enable the efficient modelling and synthesis of multilayer FSS. The first part of this chapter introduces the general formulations of electric and magnetic field integral equations (EFIE & MFIE) for the analysis of capacitive and inductive FSS that have been

developed respectively for this work. The EFIE and MFIE are used to determine the unknown electric and magnetic currents on the array. The determined complex current are then utilized to calculate the scattered coefficients of reflection and transmission fields with respect to the incident field. The scattered coefficients can in turn be employed to generate the generalized scattering matrix (GSM) of a single periodic array, which can be used for rapid and efficient calculation for cascaded multilayer structure. Implementations of numerical computations based on Galerkin method of moments to solve EFIE and MFIE have been developed using MATLAB. Validation of the numerical computation results of transmission and reflection coefficients have been compared with commercial software full wave EM solver. The developed numerical in-house computation are in good agreement with full-wave EM simulation results. The second part of this chapter provides the underpinning filter theory that is pertinent for the design of multilayer FSSs. In particular, the resonator coupled immittance inverter network serves as the starting point for many synthesis and design of multilayer FSS.

Chapter 4: Asymmetrical Impedance Inverter for Quasi-Optical Bandpass Filters with Transmission Lines of Fixed Length

Quasi-optical filter design is commonly based on the direct coupled bandpass filter topology with distributed resonator elements. Conventionally, prototypes with symmetrical impedance inverters are employed during synthesis, and as a result this leads to resonators with custom lengths across the filter. This can be impractical from a quasi-optical filter implementation perspective, since spacers of arbitrary thickness may not be readily available. A novel impedance inverter equivalent network is proposed which allows the development of prototypes where transmission lines across the filter structure to have predefined fixed lengths. Based on this technique, a fourth order quasi-optical filter prototype is developed that composed of two-dimensional periodic arrays with sub-wavelength features. Its performance is verified with free-space measurement and the measured results shows good agreement with both full-wave and circuit simulation.

Chapter 5: Design of Quasi-Optical Reflector with Customizable Group Delay

In this chapter, a novel QO reflector based on fixed transmission lines is proposed with the capability to de-multiplex an incoming wave into two linear polarized waves. One polarization will be reflected unimpeded, while the other polarization experience a specified time delay. As a result, the QO reflector able to demonstrate identical functionalities as the aforementioned time delay multiplexing technique. A synthesis

procedure for designing QO reflector for a prescribed time delay has been presented. Based on this procedure, a fourth-order QO reflector prototype comprises of 2-D periodic arrays has been developed. The performance of the developed prototype is validated with free-space measurement, and the measured results show good agreement with both full-wave and circuit simulation.

Chapter 6: Conclusion and Future Work

The conclusion summarises the accomplishment and achievements with regards to each research objective with possible future work and improvements proposed.

1.4 Research papers produced during working on this thesis

- Wenxing Tang, Pak Kwan. Loo, George Goussetis, "Time-delay reflector for time-domain pulse splitting, Loughborough Antennas and Propagation Conference (LAPC), 10-11 Nov. 2014, DOI: 10.1109/LAPC.2014.6996338

- Pak Kwan Loo and George Goussetis, "Asymmetrical Impedance Inverter for Quasi-Optical Bandpass Filters With Transmission Lines of Fixed Length," IEEE Transactions on Microwave Theory and Techniques, Volume: 66, Issue: 11 , Nov. 2018, DOI: 10.1109/TMTT.2018.2873396

- Pak Kwan Loo and George Goussetis, "Design of Quasi Optical Reflector with Customizable Group Delay," IEEE Transactions on Antennas and Propagation (Major Revision)

Chapter 2: **Multilayer Frequency Selective Surfaces Literature Reviews**

2.1 **Introduction**

Traditional single layer resonant FSS exhibit first order bandpass or bandstop filter response, which are inherently narrow band. Thus, the frequency response of a single layer FSS is often too narrowband for practical applications. Moreover, their frequency responses are potentially susceptible to the angle of incoming EM wave. In order to address these drawbacks, multilayer FSSs have been employed to achieve higher order filter responses. As has been stated in previous chapter, higher order filter responses is conventionally realized through cascading single resonant FSS array with the quarter wavelength apart between adjacent arrays [11].

A different class of multilayer FSS comprises a panel of non-radiating aperture [33] or coplanar waveguide (CPW) resonator [34] that is placed in between two radiating patch layers to achieve higher order filter response and selectivity. The proposed technique basically entail exploiting coupling apertures or resonators of the middle panel to engineer multipole filter response.

Another class of FSS reported in [43], consist of sub-wavelength capacitive and inductive meshes printed on both sides of a dielectric substrate which exhibits first order bandpass filter response. This feature has enable multilayer FSS designs with overall low-profile structure as report in [36]–[38], [44]. As a result, the frequency response associated with this class of FSS is less susceptible with the angle of incoming EM wave, while maintaining stable bandwidth.

In this chapter, the review focuses on design techniques for the above mentioned FSS structure. Specifically, the aperture coupled resonator and miniaturized FSS structure are reviewed in section 2.2 and 2.3 respectively. These reviews were carefully considered in order to generate new ideas and develop synthesis technique with the aim to simplify the design of multilayer FSS.

2.2 **FSS Based Aperture-Coupled Resonator Structure**

This class of FSS bandpass filter are realized with resonant metallized array. The design strategy exploits resonant elements transmit and received antennas coupled to a non-resonating or resonating planar layer implementation where frequency selectivity is performed. These filters, printed in a radiating [34] or non-radiating [33], [39] layer between two antenna layers, can be tailored to achieve higher order filter response. This approach has enabled simple and compact QO filter structure. The frequency response demonstrated in [33], [34] shows high selectivity and promising polarization characteristics. Three types of FSS design of this class are addressed below.

2.2.1 A FSS using aperture-coupled microstrip patches

A single polarization FSS structure reported in [33] comprises of three periodic arrays, which consist of a dipole slot array placed in between two rectangular array of conducting patches printed on dielectric substrates. The overall construction of the device is shown on Figure 2.1.

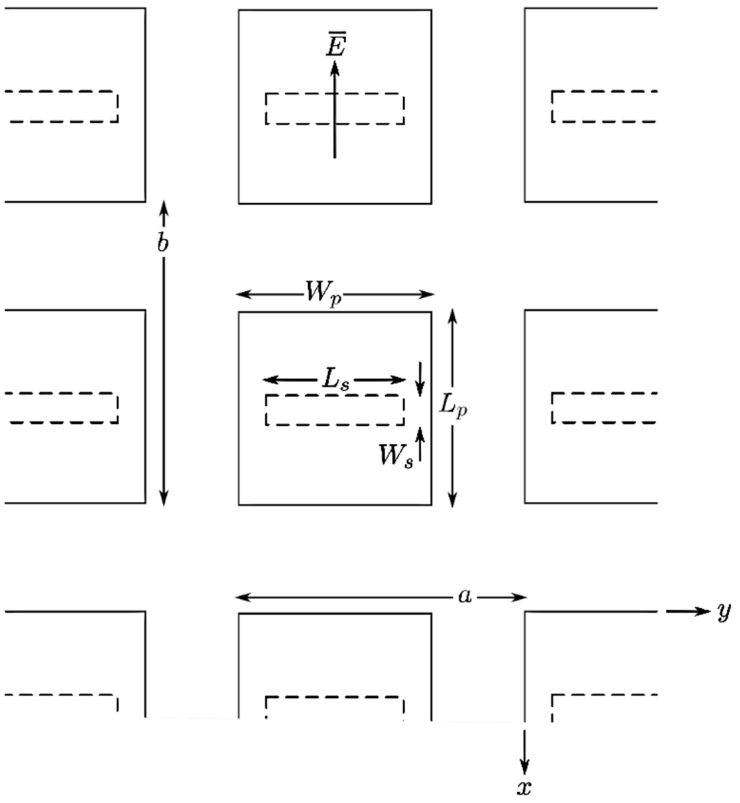

(a)

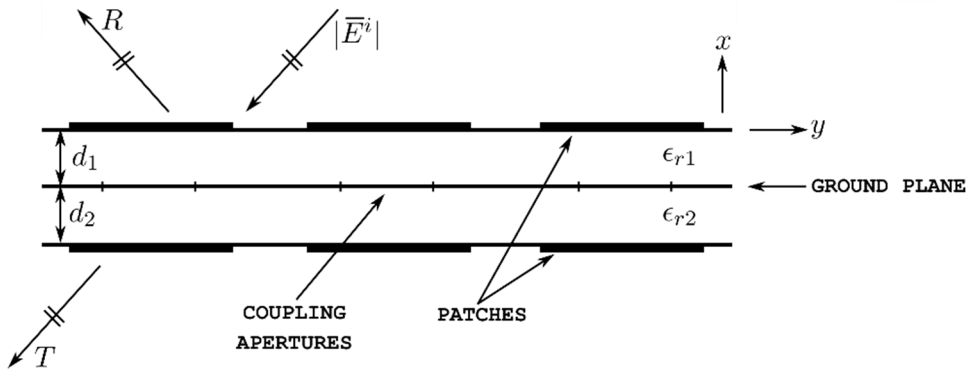

(b)

Figure 2.1 Geometrical layout of the developed FSS in [33] (a) Top view (b) Side view

The resonant frequency mainly depend on the dimension of the rectangular patches. On the other hand, the dipole slot length is responsible for the coupling level between the two resonant patches. At optimum length, the resonator is critically couple to produce unity transmission coefficient. However, if the slot length is further increases beyond the optimum length, a secondary resonance present at lower frequency relative to the main resonance. While, if the slot length is below optimum length, the incident energy are not fully transmitted and as a result the transmission coefficient is below unity. The aforementioned frequency responses with the dipole variations are illustrated in Figure 2.2.

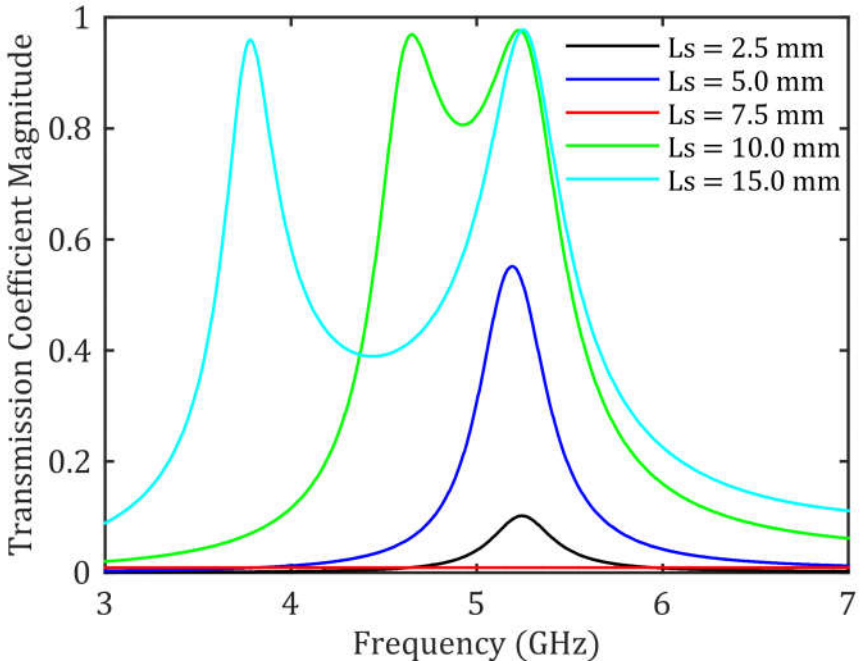

Figure 2.2 Variation of the frequency response of the FSS with slot length, L_s. (L_p = W_p = 17.1 mm, W_s = 0.5 mm , ε_r, = 2.33, d = 1.6 mm, and a = b = 28.3 mm.) [33]

Moreover, the frequency response also relies on the substrate thickness. In particular, the thickness also affect the degree of coupling between the two resonators as demonstrated in Figure 2.3. While, variations of others parameters such as dipole width and dielectric constant affects the coupling level at a lesser degree relatively.

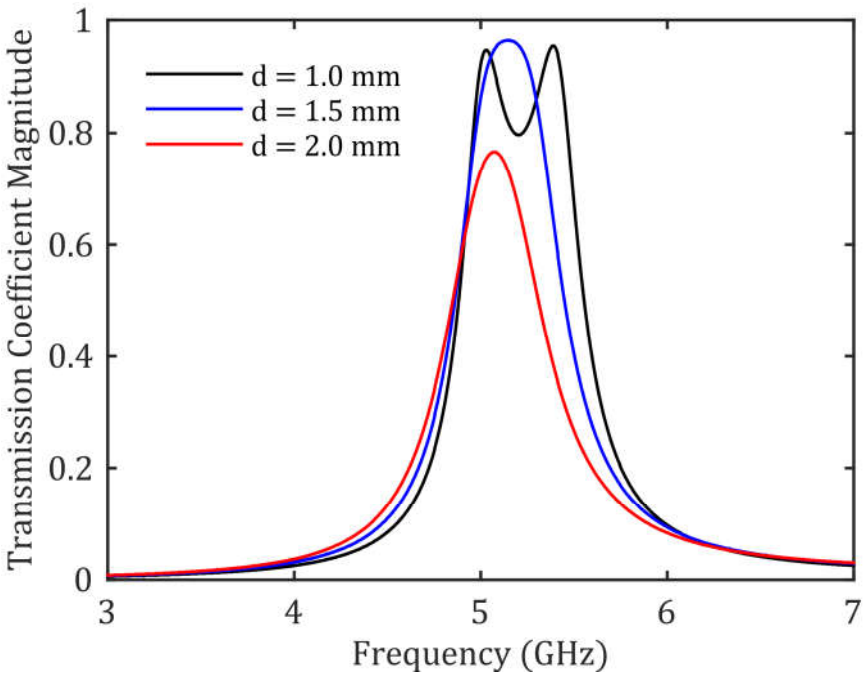

Figure 2.3 Variation of the frequency response of the FSS with substrate thickness, d. ($L_p = W_p =$ 17.1 mm, $L_s = 7$ mm, $W_s = 0.5$ mm, $\varepsilon_r = 2.33$, $d = 1.6$ mm, and $a = b = 28.3$ mm.) [33]

2.2.2 Antenna–Filter–Antenna Arrays as a Class of Bandpass FSS

A different design approach based on aperture coupled FSS structure was proposed in [34]. Instead of a non-resonant slot as demonstrated in [33], an implementation with a coplanar waveguide (CPW) structure for the middle array is proposed in [34] as conceptually shown in Figure 2.4.

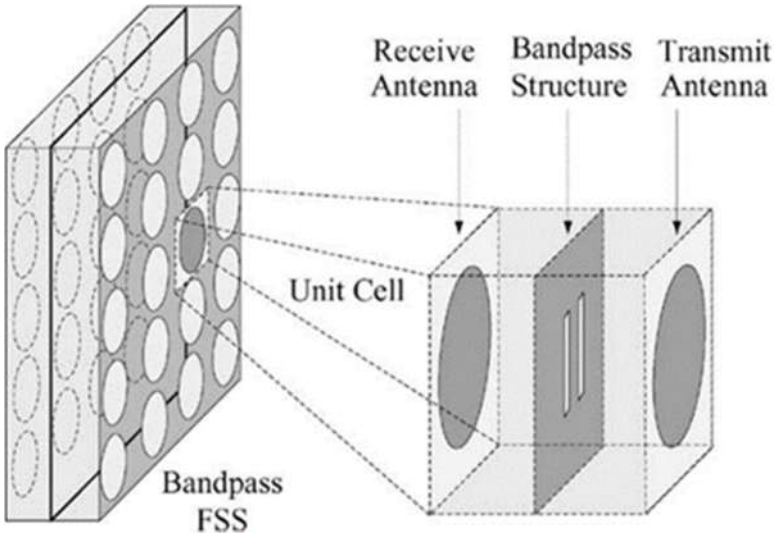

Figure 2.4 AFA array composed of radiative patch antenna and CPW resonators [34]

The functions of CPW layer are two fold, which is to couple the two outer radiative resonant elements and also perform as resonator at the designed operating frequency. Geometry of the CPW and its arrangement with respect to the radiative elements can be design appropriately to produce transmission zeros near the edges of the passband to improve frequency selectivity. Two design examples extracted from [34] are discussed below to illustrate the design features.

The first design example (Type-I) demonstrated in [34] is a three pole Chebyshev filter with 8% bandwidth at operating frequency 35 GHz. Figure 2.5(a) illustrates the unit cell arrangement along and its equivalent circuit in Figure 2.5(b). The equivalent circuit model composed of two series resonant elements and a shunt quarter wavelength CPW resonator. The quarter wave CPW resonator and the resonant patches is coupled through the open end of the CPW resonator and its relative position determine the degree of coupling. Therefore, the important design parameter in this case depends on the relative position of the slot after the radiating patches and CPW line dimensions have been determined. The simulated and measured frequency response for this design is presented in Figure 2.6.

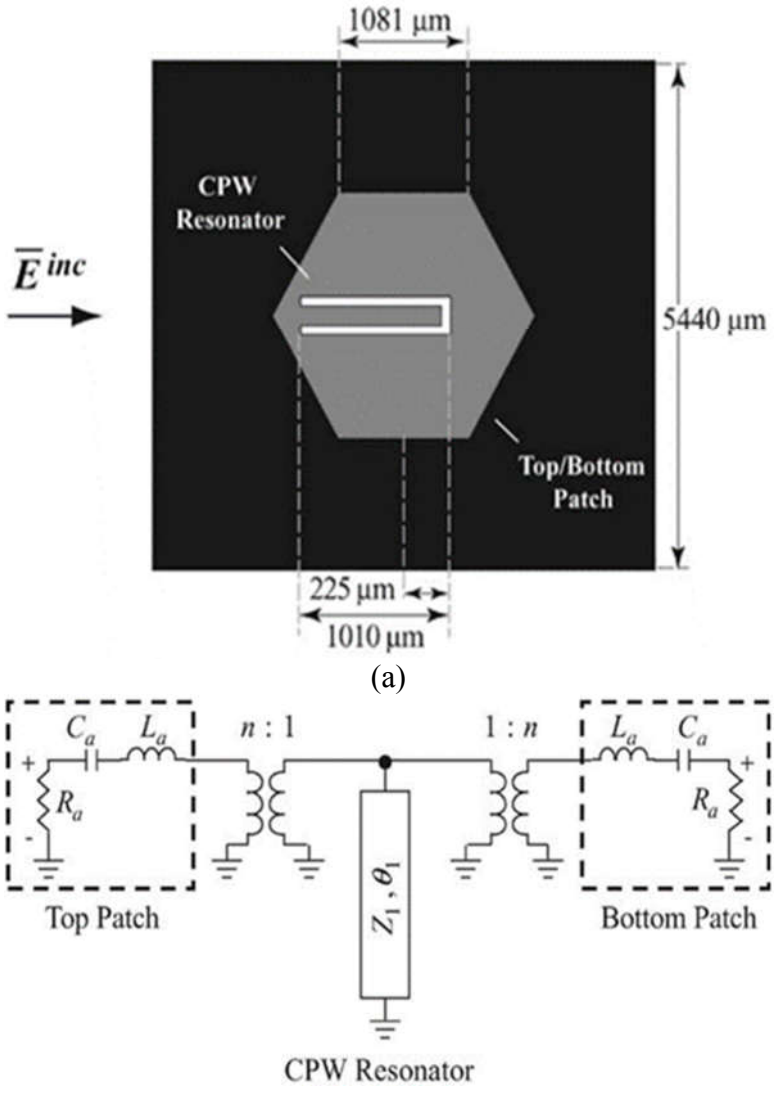

Figure 2.5 Type-I FSS. (a) Unit cell arrangement. (b) Equivalent circuit [34]

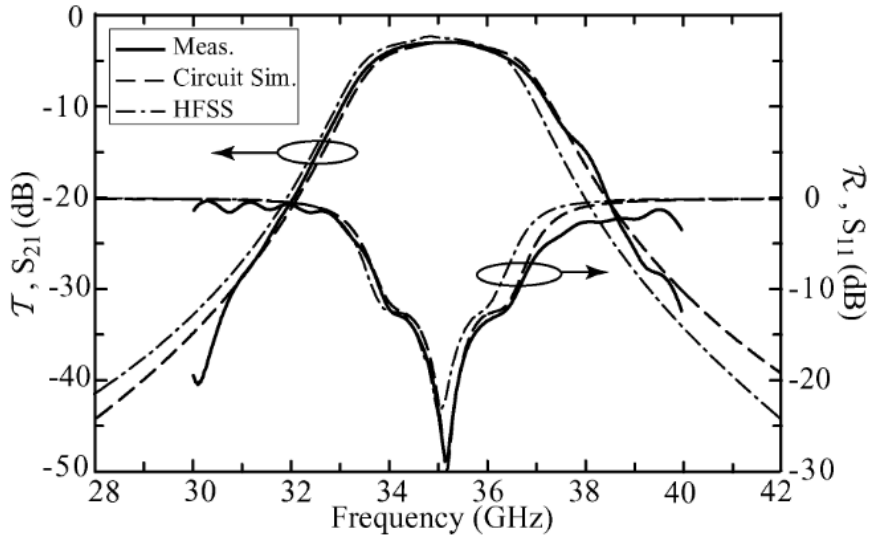

Figure 2.6 Transmission and reflection coefficients of the Type-I FSS for normal incidence with horizontal polarization [34]

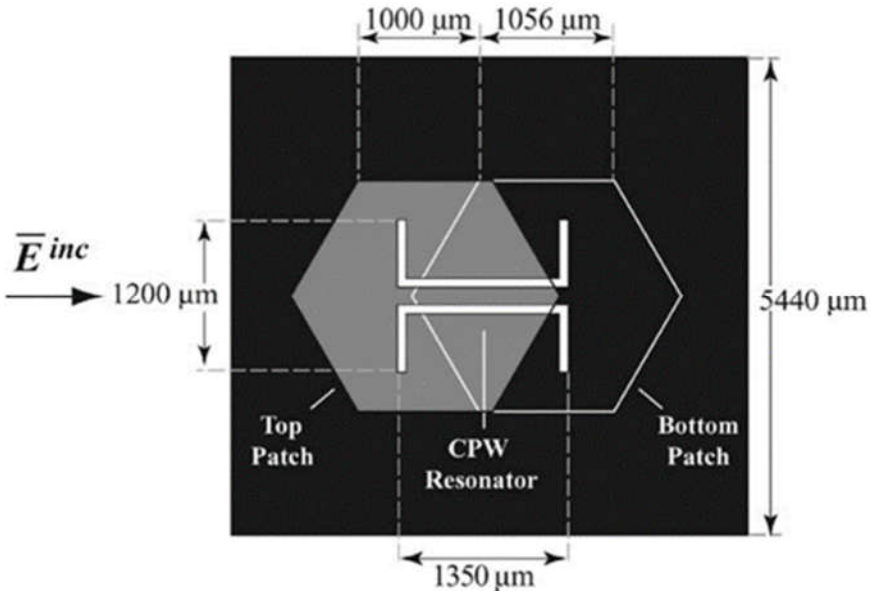

(a)

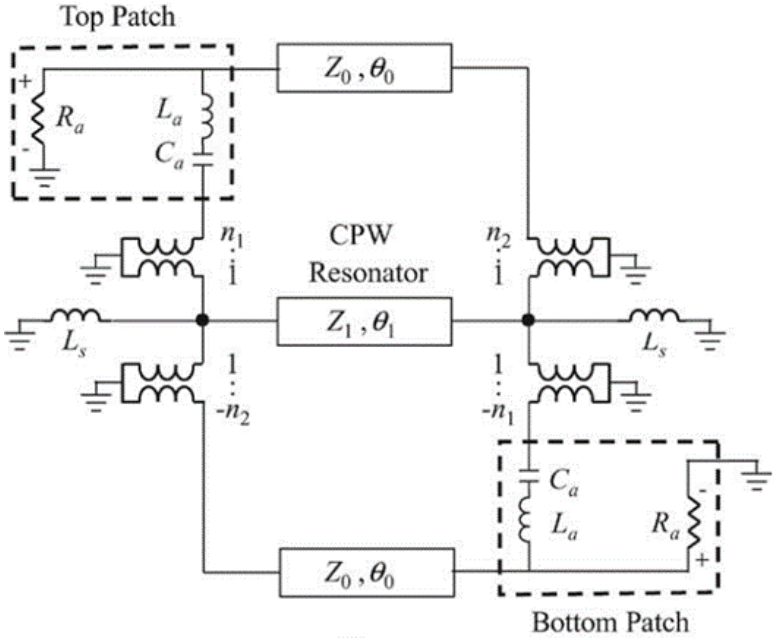

(b)

Figure 2.7 Type-II FSS. (a) Unit cell arrangement (b) Equivalent circuit [34].

The second design example (Type-II) involved a half-wavelength CPW resonator with top and bottom patch elements are displaced horizontally to form an asymmetric arrangement with respect to the CPW layer. Figure 2.7 shows the FSS unit cell arrangement and its equivalent circuit. The resonant patches are coupled with the CPW resonator through the vertical slots of the CPW layer. Basically the main coupling exist between the radiating patches and the vertical slot. However, additional coupling also exist due to the opposite slot. Consequently, the presence of this coupling causes in a 180° transmission phase difference between the two patches [34] and as a result a

transmission zero appear at the lower side band. Optimization using full wave simulation to determine the dimensions of the coupling slots, CPW resonator and its position with respect to the patches are required before practical realization. Figure 2.8 displayed the simulated and measured frequency response of the Type-II FSS design.

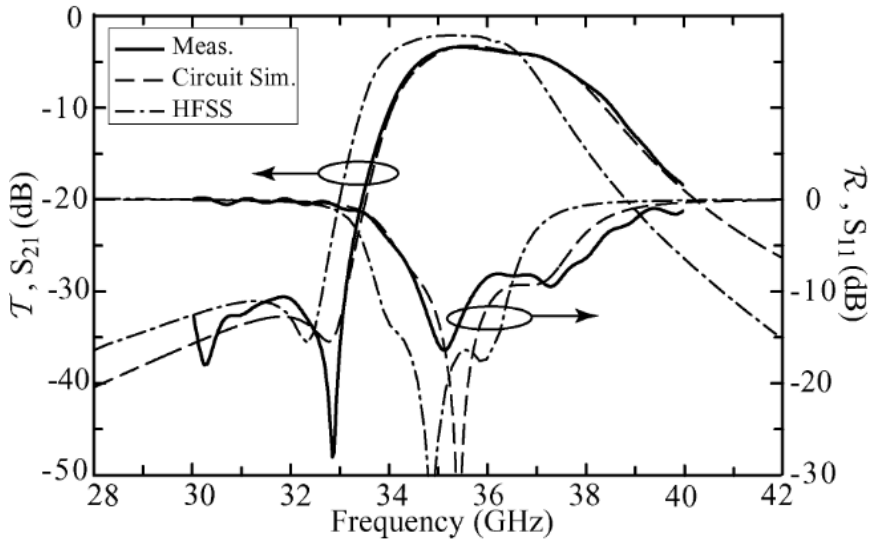

Figure 2.8 Transmission and reflection coefficients of Type-II FSS for normal incidence with horizontal polarization [34]

The proposed technique has demonstrated design flexibility by utilizing the geometry of the CPW and its relative position with respect to the two radiating patch layer to achieve better frequency selectivity. Moreover, unlike the traditional multilayer FSS design, higher order filter response can also be realize by adding resonator components in CPW layer.

However, the unit cell dimension for this class of filter have to make equal to the radiative aperture antenna area [34], which result in the unit cell periodicity larger than half wavelength. Therefore, this poses problem with early onset grating lobes when the FSS is subjected to angle of incidence. Furthermore, intricate fabrication technique is required to avoid geometrical defect on the CPW layer to prevent undesirable parasitic couplings that jeopardize the frequency responses. As noted in [34], this approach also strongly depends on the substrate thickness.

2.2.3 *Design and Analysis of a High-Selectivity Frequency-Selective Surface at 60 GHz*

A different implementation of aperture coupled FSS was proposed in [39], using crossed-dipole resonator arrays for the outer layers and coupled by rectangular apertures in the middle layer. Figure 2.9 illustrate the unit cell of this FSS. Contrary to the work in [34], the proposed FSS is a symmetrical structure that are able to filter both vertical and horizontal polarizations.

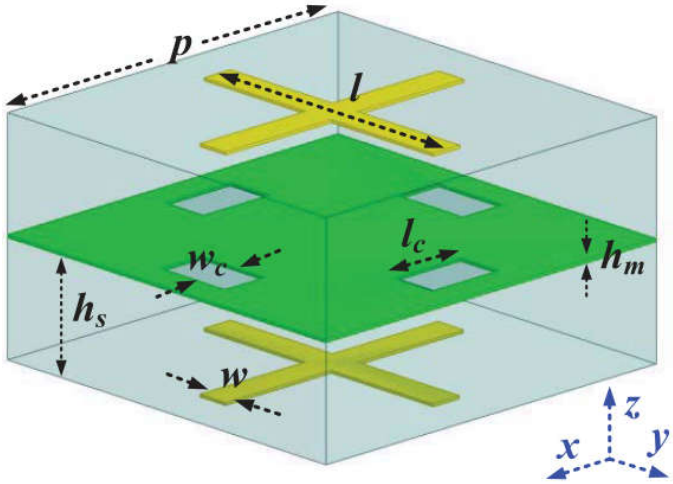

Figure 2.9 Isometric view of the proposed FSS unit cell [39].

The working principles of this FSS can be understood using equivalent circuit model shown in Figure 2.10(a). The series resonator represent the resonant patch elements while the coupling aperture is designated as the shunt resonator. Magnetic and electrical coupling paths between series resonators are denoted by mutual inductance, L_m and capacitance, C_m respectively. Similarly, L_{m1} and C_{m1} are the mutual inductance and capacitance that represent the magnetic and electrical couplings between aperture and resonator accordingly.

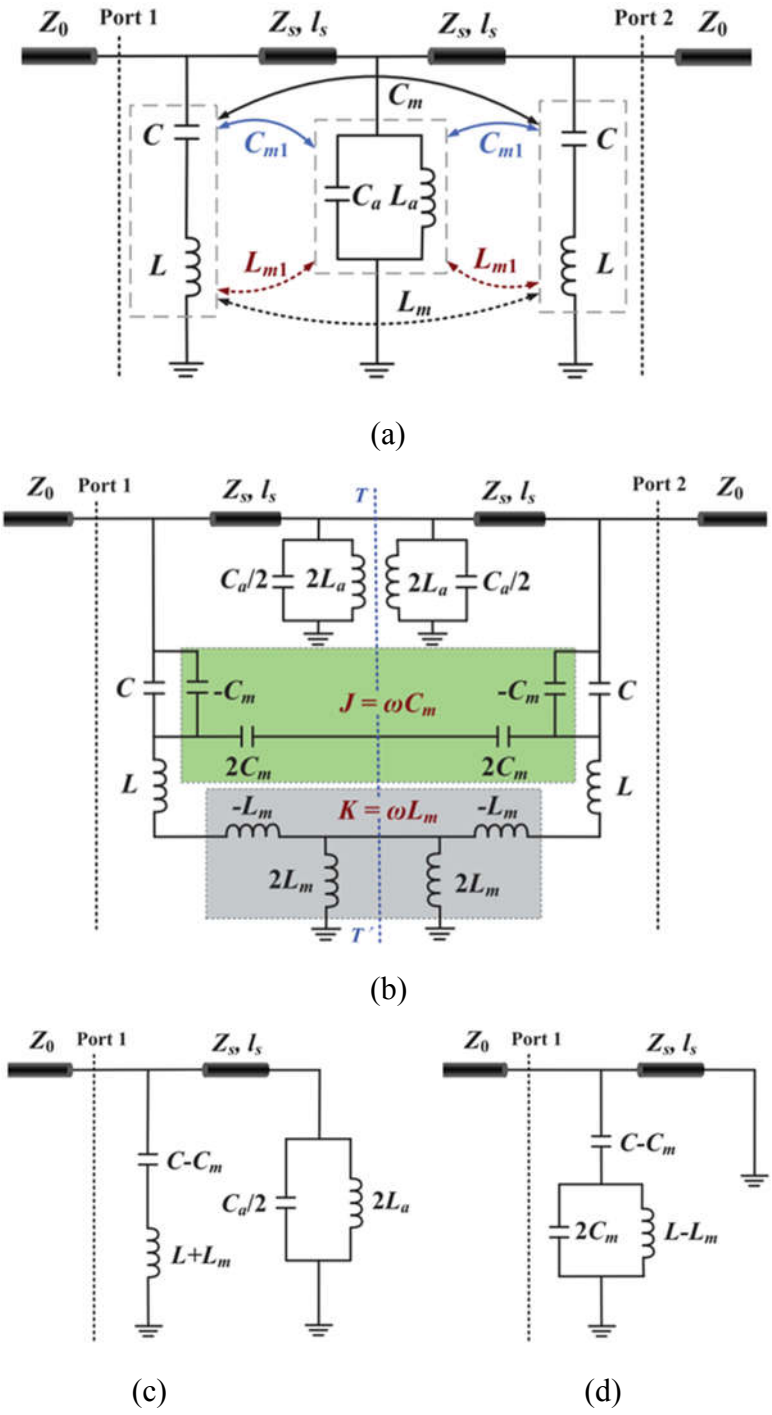

Figure 2.10 (a) Equivalent-circuit model of the aperture coupled FSS. (b) Simplified equivalent circuit model excluding the mutual inductance Lm1 and the mutual capacitance Cm1. (c) Even-mode circuit. (d) Odd-mode circuit. [39]

However, the aperture couplings are negligible compared to the couplings between the series resonators. Therefore, based on this assumption the mutual inductance, L_{m1} and capacitance, C_{m1} parameters are excluded in simplified circuit model shown in Figure 2.10(b). While, the mutual inductance, L_m and capacitance, C_m are replaced with equivalent immittance inverter circuit [45].

Applying open and short circuit on the symmetry plane of the simplified circuit model leads to even and odd mode circuit, as illustrated in Figure 2.10(c) and Figure 2.10(d) respectively. These equivalent circuits enable analysis to determine the pair of even and odd mode resonant frequencies. These pair of frequencies are found as

$$f_{even} \approx \frac{1}{2\pi\sqrt{(L_0 + 2L_m)(C_0 - 2C_m)}} \tag{2.1}$$

$$f_{odd} \approx \frac{1}{2\pi\sqrt{L_0 C_0}} \tag{2.2}$$

The parameters L_0 and C_0 that are present in expressions (2.1) – (2.2) corresponds to the inductance and capacitance of the resonator without the coupling aperture. The expressions are independent from the aperture couplings. Subsequently, these pair of frequencies are utilized to compute the overall coupling coefficient, k [39]

$$\begin{aligned} k &= \frac{f_{odd}^2 - f_{even}^2}{f_{odd}^2 + f_{even}^2} \\ &= \frac{\frac{L_m}{L_0 + L_m} - \frac{C_m}{C_0 - C_m}}{1 - \left(\frac{L_m}{L_0 + L_m}\right)\left(\frac{C_m}{C_0 - C_m}\right)} \end{aligned} \tag{2.3}$$

The magnetic and electric coupling coefficients are defined as $k_m = L_m/(L_0 + L_m)$ and $k_e = C_m/(C_0 - C_m)$ respectively [39]. Using these definition, the overall coupling coefficient, k reduces to

$$k = \frac{k_m - k_e}{1 - k_m k_e} \tag{2.4}$$

The overall coupling is dependent on both electric and magnetic coupling paths. Therefore, desirable frequency response can be engineered by adjusting the coupling levels for different values of k_e and k_m respectively. It is noted that when electric coupling is dominant transmission zeros appear at the lower and upper side of the passband. On the other hand, no transmission zero is observed when magnetic coupling is dominant. These transmission zeros are produced when the magnetic and electric coupling signal path are out of phase [39]. Moreover, L_a and C_a values of the aperture equivalent circuit should not be zero, however their resonance should be far away from the passband to

prevent unwanted harmonics in the frequency response. For this reason, the design of this FSS focuses on the apertures dimension as well as their relative position with respect to the centre of the unit cell.

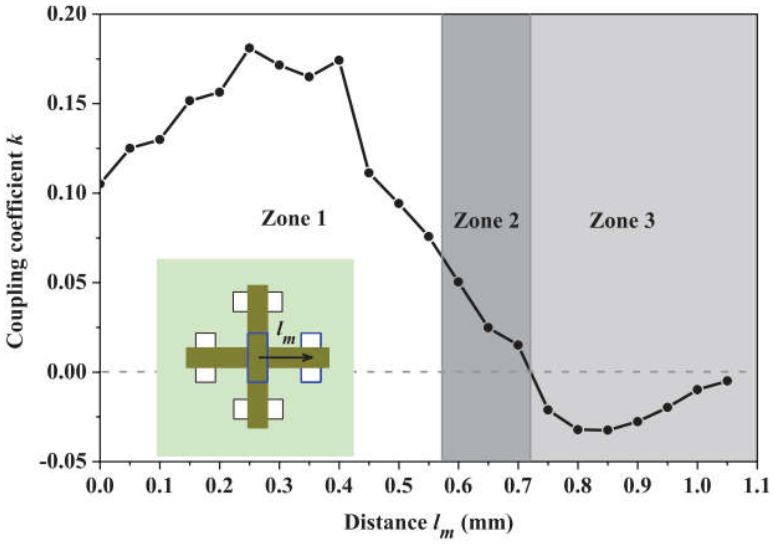

(a)

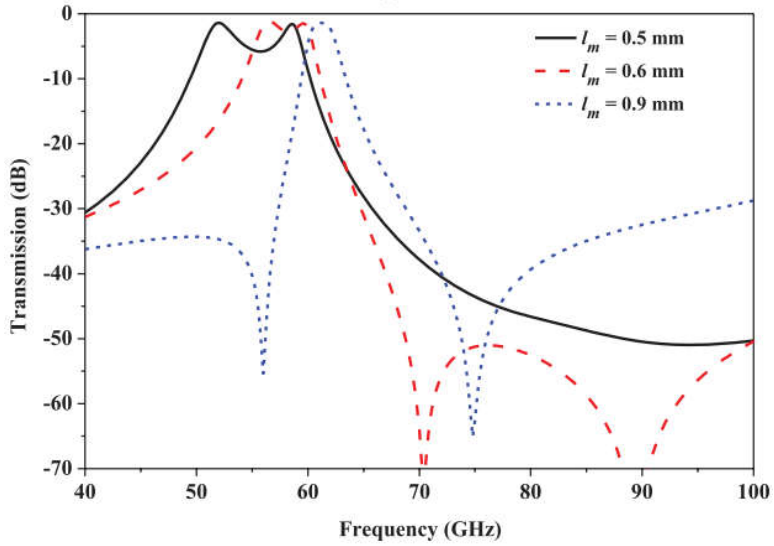

(b)

Figure 2.11 Effects of the locations of the coupling apertures on the: (a) simulated overall coupling coefficient k and (b) simulated transmission response of the proposed 60-GHz ACR FSS [39].

It is noted that the length of the aperture, l_c affects the frequencies location of the two transmission zeros, while the width of the aperture, w_c directly affect the coupling strength. More importantly the position of the aperture affects in greater extend the overall coupling coefficients as illustrated in Figure 2.11. Zone 1 and 2 correspond to magnetic coupling dominant regions, while Zone 3 is electric coupling dominant region. In addition to the coupling apertures, the used of substrates also affect the mutual couplings between

the top and bottom resonators [39].The initial cross-dipole dimension is set slightly less than half-wavelength for a specified frequency response and subsequently the final dimension of the FSS, in particular the cross dipole and aperture coupling are obtained with successive optimization using full-wave simulation. Figure 2.12 present the measured frequency responses, EM and circuit simulations at normal incident. The slight disagreement of the measured result with both the EM and circuit simulation is attributed to the mutual couplings (L_{m1} and C_{m1}), which is not taken into account in the equivalent circuit [39].

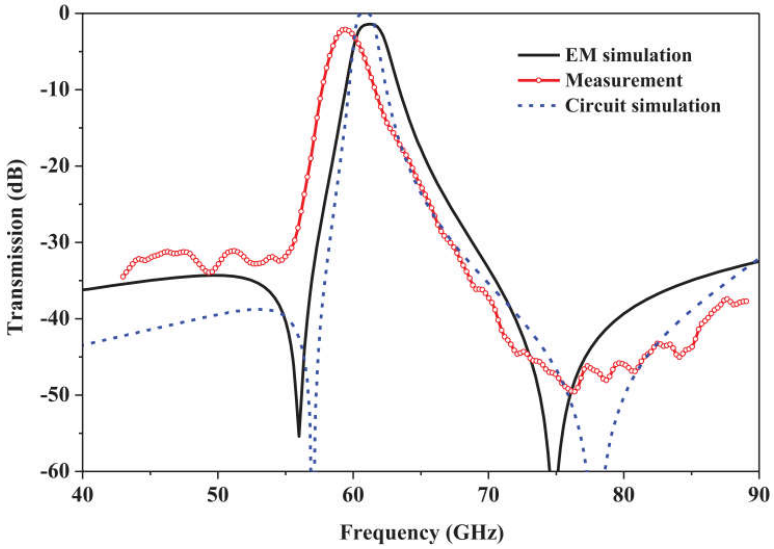

(a)

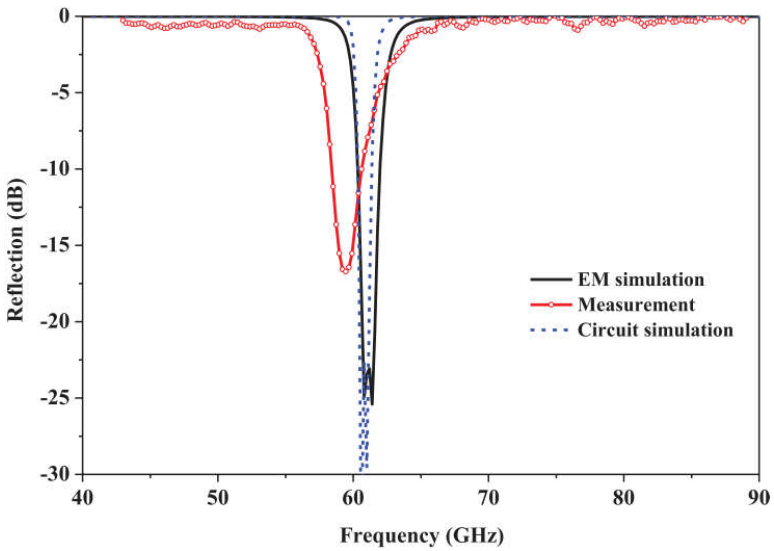

(b)

Figure 2.12 Comparison results between the measured results and the simulated results obtained by the full-wave EM simulation and the circuit simulation at normal incidence. (a) Transmission response. (b) Reflection response [39].

2.3 Bandpass Filter Based Miniaturized Element Frequency Selective Surfaces (MEFSS)

An engineered surface perform as first order bandpass filter comprises of doubly periodic arrays printed on a thin dielectric substrate was proposed by [43]. The printed arrays are assumed to have the same periodicity. On one side of substrate consist of array of conducting patches, while the other side consist of wire grid. When transverse electromagnetic waves interact on the surface, the conducting patches and wire grid behave as capacitor and an inductor, respectively as depicted in Figure 2.13. Hence, such arrays arrangement can be seen as a parallel LC resonator.

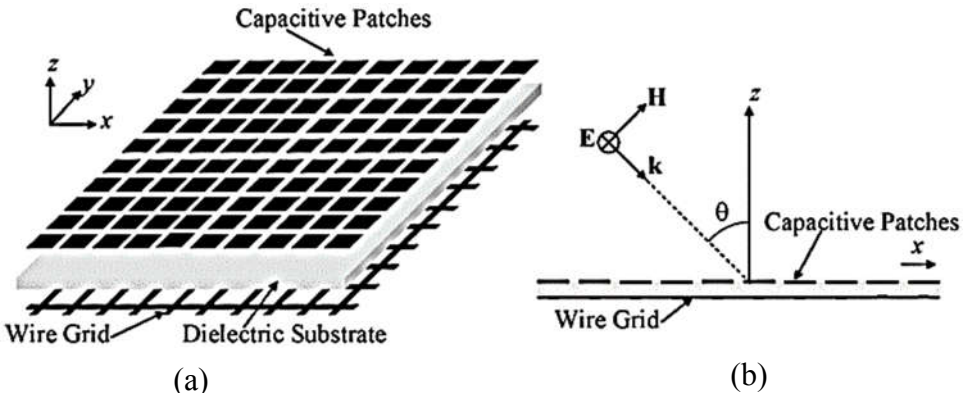

Figure 2.13 Topology of the first order bandpass FSS formed by arrays of capacitive patches and inductive grid separated by a dielectric substrate. (a) 3-D view and (b) side view [43].

It is noted that the unit cell area for this class of FSS is significantly reduce compared to the conventional constituting resonant element as described in the earlier section 2.1. As a result, the periodic surface is less susceptible to variation of incident angle. These attractive features have enable novel and higher order filter design as reported in [36], [44], [46]. Two design strategies for bandpass filter adotping this class of FSS are discussed below.

2.3.1 A Generalized Method for Synthesizing Low-Profile, Band-Pass Frequency Selective Surfaces with Non-Resonant Constituting Elements

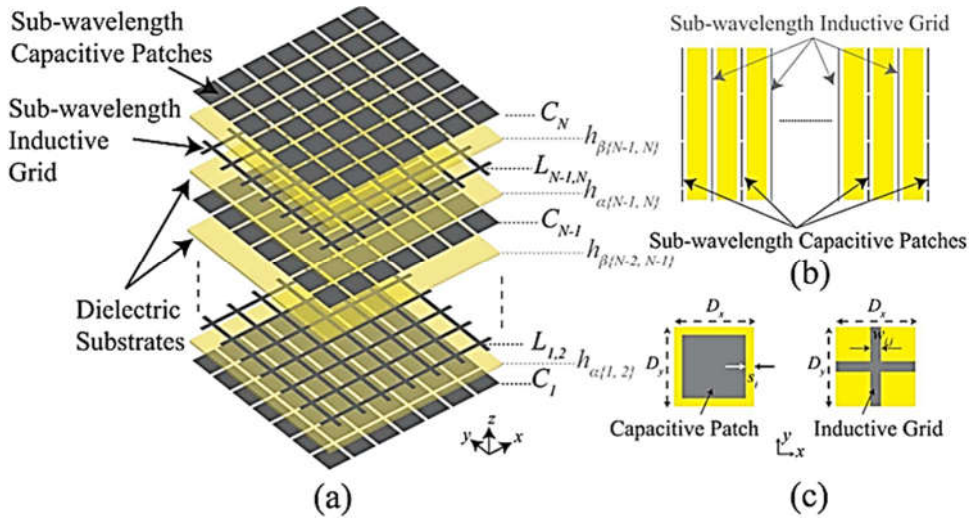

Figure 2.14: (a) Exploded view of the proposed FSS topology comprises of successive stacked arrays and dielectric substrates. (b) Side view of the proposed FSS structure. (c) Unit cell of the FSS [46].

The generalized synthesis procedures reported in [46] enable bandpass FSS filter design of arbitrary order and transfer function. The proposed FSS structure implement cascaded capacitive patches and inductive wire grid periodic arrays that are separated by thin dielectric substrates. Regardless of the filter order, the arrays of the first and last layer always corresponds to capacitive patches in this proposed FSS topology. Figure 2.14 depict the 3-D architecture of the proposed FSS alongside with its side view and unit cell structure for both capacitive patch and inductive grid.

Figure 2.15(a) represent the equivalent circuit of the proposed FSS structure, where all the transmission lines are assumed to be non-identical. The electrical length of the transmission lines are assumed to be lesser than 30° in order for the employed equivalent circuit model to be valid. Therefore, based on this assumption the transmission lines are replaced with their equivalent π-network [47], as illustrated in Figure 2.15(b). The capacitor elements from the short transmission lines that are adjacent to the capacitive layers are absorbed into a single capacitor. While, the other pairs that are adjacent to the inductive layers are neglected since the susceptance magnitude of the capacitors are negligible compare to the inductors. The subsequent simplified model is depicted in Figure 2.15(c). Moreover, the equivalent circuit can be further transformed by converting the inductive T-network to their equivalent π-network. As a result of these simplification,

the equivalent circuit reduces to the conventional coupled-resonator bandpass filter, as depicted in Figure 2.15(d).

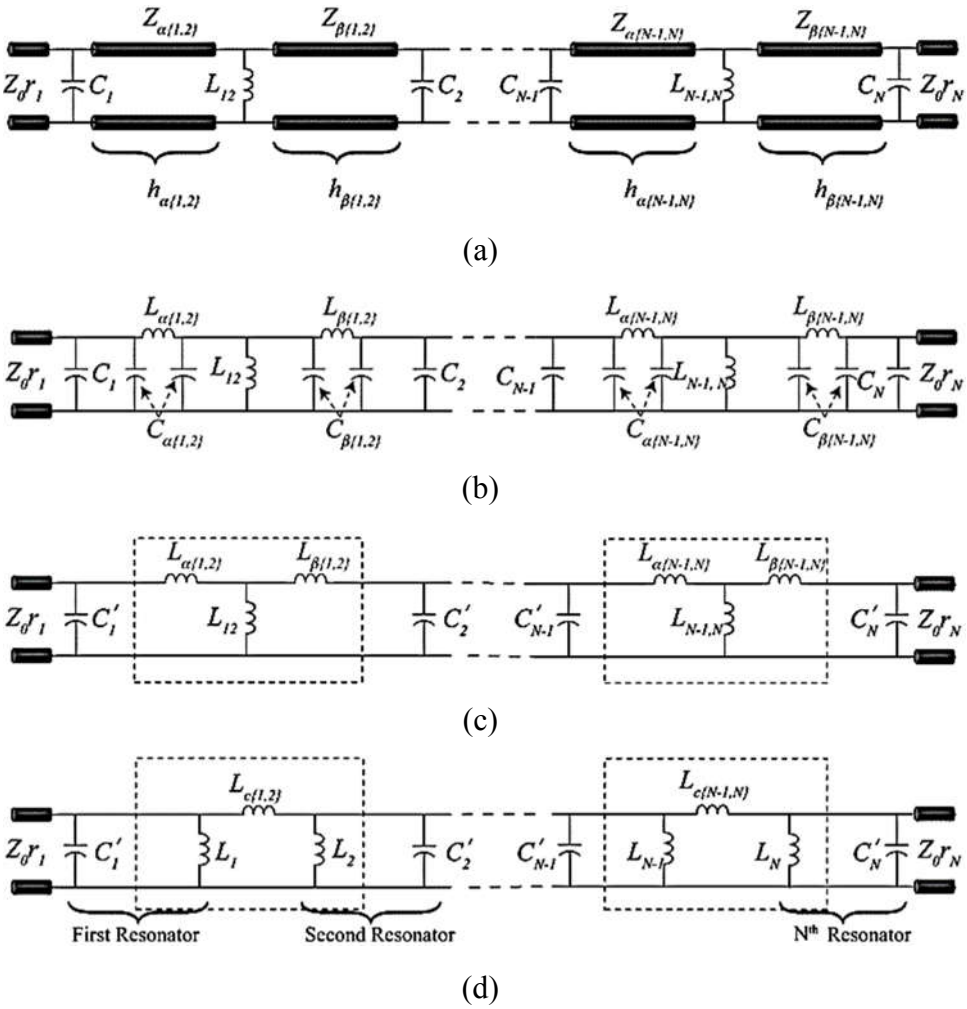

Figure 2.15: (a) Equivalent circuit model of the general FSS shown in Figure 2.14(a) for normal angle of incidence. (b) Transmission lines in (a) are replaced by their simple LC equivalent network. (c) Further simplification in (b) by neglecting parasitic capacitances adjacent to inductor wire grid. (d) Inductor coupled bandpass network after T to π transformation from (c) [46].

Therefore, for given specifications such as operating frequency, bandwidth, response type and order, the lumped elements correspond to the conventional coupled resonator bandpass filter in Figure 2.15(d) can be calculated. Subsequently, the circuit parameters in Figure 2.15(a) can be determined [46]. The obtained capacitances and inductances corresponds to Figure 2.15(a) are then map to geometrical dimensions for rectangular patches and wire grid of the FSS using approximation formula from [48]. These estimated geometrical dimensions for the constituting elements are then optimized successively using full-wave simulation to match the frequency response of the equivalent circuit model of Figure 2.15(d). An example of third-order band-pass FSS with a 0.1 dB ripple Chebyshev response, center frequency of operation of 10.82 GHz, and fractional

bandwidth of 21.7% was demonstrated in [46]. The measured frequency response of this bandpass FSS along with its full wave and equivalent circuit simulations are shown in Figure 2.16.

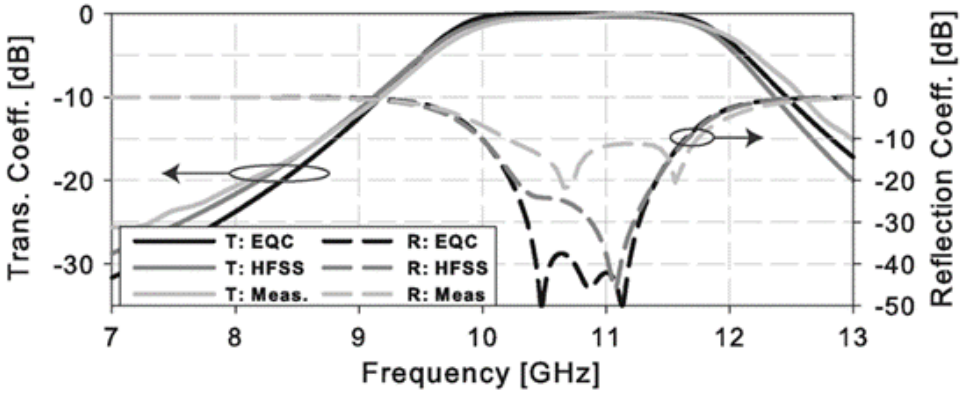

Figure 2.16 Reflection and transmission coefficients of the band-pass FSS. Simulation results in HFSS and theoretically predicted ones are compared with the measurement results [46].

Indeed the proposed techniques lead to FSS design with overall low profile structure that are able to provide stable frequency responses with respect to angle of incident. The aforementioned features offer practical advantages at lower operating frequency compare to the traditional FSS with resonant constituting elements. However, if the designed FSS to be realized at higher operating frequency for narrow bandwidth application, practicability issues arises. To illustrate this, consider a design example utilizing the same material and periodicity reported in [36] for second order Butterworth response bandpass FSS operating at 30GHz with 5% fractional bandwidth. Based on the design equations, it is found that the overall profile thickness and gap spacing for the capacitive periodic array are approximately 109 μm and 58 μm respectively. The overall profile is considerably smaller compare to the wavelength. This attribute may offer stable frequency response with respect to the angle of incident, however structural reliability is a concern. Additionally, the minimal gap spacing attainable in standard low cost PCB fabrication is 150 μm. Therefore, in order to achieve a gap spacing approximately three times smaller than the minimum feature may not be feasible with the conventional low cost PCB fabrication.

2.3.2 *Inductively-Coupled Miniaturized-Element Frequency Selective Surfaces With Narrowband, High-Order Bandpass Responses*

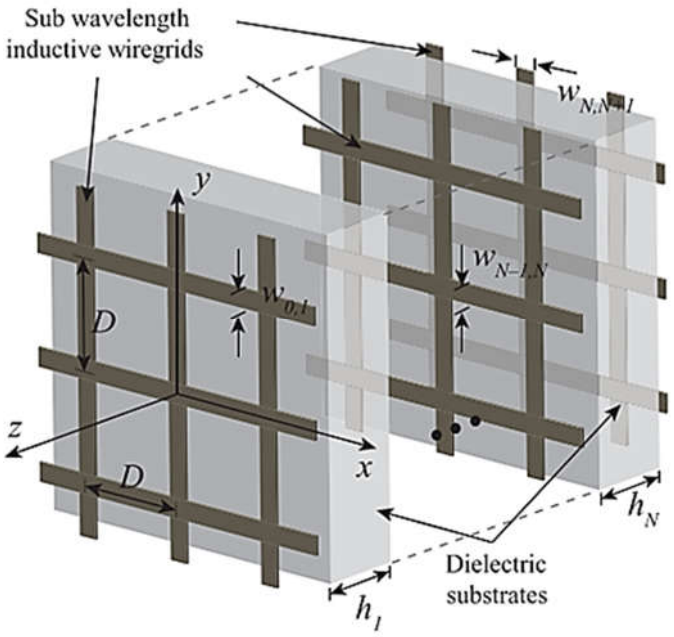

Figure 2.17: Generalize structure of the proposed bandpass FSS of N[th] order filter response, comprises of N dielectric resonator layers and N+1 array layers [38].

The work reported in [38] exploit direct coupled cavity filter prototype that enables the deterministic design using classical equivalent circuit approaches. According to the approach proposed in [38], the inverters are realized as periodic inductive grids and the dielectric substrate as half-wavelength cavities resonator. This strategy enables higher quality factors even at mm-wave frequencies and the realization of narrowband filters. It is noted that the permittivity and permeability of the implemented dielectric substrate is identical throughout the filter structure. The design equations that determined the inductive inverters are as follows:

$$L_{0,1} = \frac{Z_0}{2\pi f_0 \sqrt{\frac{1+\epsilon_r}{2}}} \frac{\sqrt{\frac{\pi\delta}{2g_0 g_1}}}{1 - \frac{\pi\delta}{2g_0 g_1}} \tag{2.5}$$

$$L_{N,N+1} = \frac{Z_0}{2\pi f_0 \sqrt{\frac{1+\epsilon_r}{2}}} \frac{\sqrt{\frac{\pi\delta}{2g_N g_{N+1}}}}{1 - \frac{\pi\delta}{2g_N g_{N+1}}} \tag{2.6}$$

$$L_{j,j+1} = \frac{Z_0}{2\pi f_0 \sqrt{\epsilon_r}} \frac{\frac{\pi\delta}{2\sqrt{g_j g_{j+1}}}}{1 - \left(\frac{\pi\delta}{2 g_j g_{j+1}}\right)^2}, \quad j = 2, \ldots, N-1 \tag{2.7}$$

The parameters Z_0, ε_r and δ represent the free space impedance, dielectric permittivity of the substrate and fractional bandwidth respectively, While, $g_0, g_1, \ldots, g_j, \ldots, g_N$ parameters are the N[th] order low-pass prototype element values that dictate the filter response. Subsequently, once the inductances are determined according to equations (2.5) – (2.7), the substrate thickness can be calculated [38]

$$h_j = \left(\frac{\lambda_0}{2\pi\sqrt{\epsilon_r}}\right) \times \left(\pi - \frac{1}{2}\left[\tan^{-1}\left(\frac{2L_{j-1,j}\sqrt{\epsilon_{f_{j-1,j}}}}{2\pi f_0 Z_0}\right) + \tan^{-1}\left(\frac{2L_{j,j+1}\sqrt{\epsilon_{f_{j,j+1}}}}{2\pi f_0 Z_0}\right)\right]\right) \tag{2.8}$$

However, this approach leads to the requirement that each dielectric spacer to have a custom electrical length. To illustrate, using the equations outlined above for the same design specifications in [38], the initial values of the inductances and substrate thickness are tabulated in the Table 2.1.

Table 2.1: Initial Calculated Inductances and Substrate Thickness for 2[nd] Order Bandpass Filter Design Implemented in [38]

Parameter	$L_{0,1}$	$L_{1,2}$	$L_{2,3}$	h_1	h_2
Value	0.3013 nH	0.0498 nH	0.3013 nH	2.2365 mm	2.2365 mm

The calculated substrate thickness may not be available commercially. The dielectric substrate used in this design is Rogers RT/duroid 6010 with permittivity, ε_r = 10.2 and the closest thickness available is 1.9 mm [38]. Therefore, practical implementation for different substrate thickness compare to the theoretical calculations above, require tuning on the inductances values as to preserve the desired filter response. The tuned inductance values of the designed filter correspond to the implemented substrate thickness are tabulated in Table 2.2.

Table 2.1: Tuned Inductances for 2[nd] Order Bandpass Filter Design with Substrate Thickness 1.9mm Implemented in [38]

Parameter	$L_{0,1}$	$L_{1,2}$	$L_{2,3}$	h_1	h_2
Value	0.4 nH	0.05 nH	0.4 nH	1.9 mm	1.9 mm

Subsequently, these inductances are then mapped to the geometrical dimensions of the inductive wire grid array. The grid arrays can be etched on single side or both sides of the substrates. Thus in order to realize this multilayer structure, the arrays are secured with bonding materials. However, the filter response is affected due to the bonding material. To circumvent this, two closely spaced identical wire grids on the two sides of the middle bonding layer is exploited, as depicted in Figure 2.18. The measured and simulated transmission coefficient of this filter is displayed in Figure 2.19.

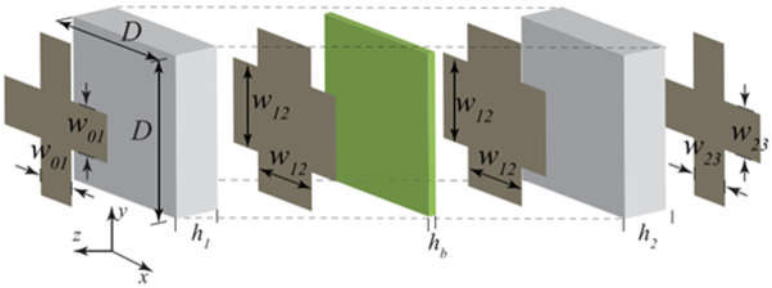

Figure 2.18: Unit cell structure of the proposed 2nd order bandpass FSS with two identical inductive grids introduced in the center to restore the symmetry of the structure. The two wire grid at the center are separated by a bonding layer [38].

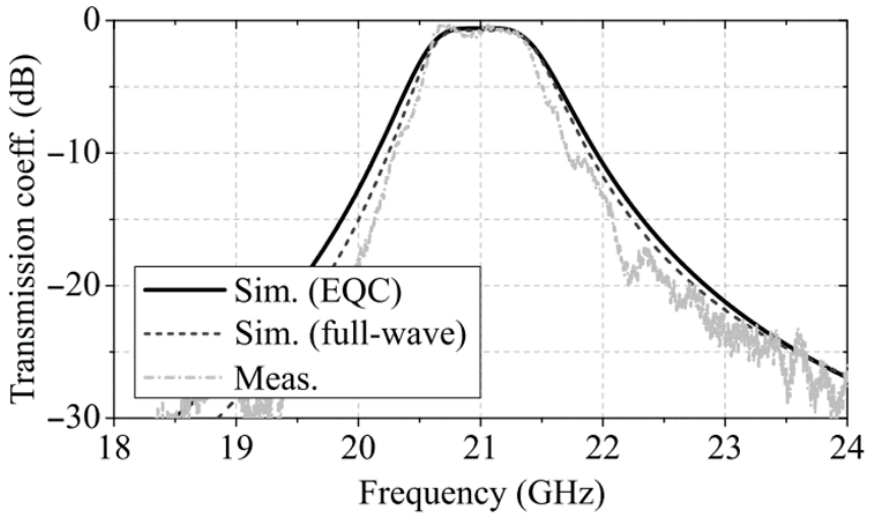

(b)

Figure 2.19: Comparison between simulations results (circuit and full-wave) with experimental free space measurement [38].

2.4 **Summary**

The aperture coupled techniques presented in section 2.2 is versatile and leads compact FSS structures. Basically, the aperture coupled approaches allows the exploitation of receive and transmit antennas as part of the filter structures, with additional resonators printed in CPW or aperture in a non-radiating layer. As noted, all approaches strongly depends on the substrate thickness. Indeed the developed prototypes were produced with an elaborated thin-film processes, which can accurately control the geometrical parameters to very small scale. As a result, this has driven the technical literature to approaches compatible with PCB technologies.

While in section 2.3, the design strategies that utilizes MEFSS structure have been reviewed. Both design techniques layout deterministic synthesis procedures derived from coupled resonator bandpass filter that enable design for arbitrary order and transfer function. While, recognizing the design method may be employable for higher order bandpass FSS design, however it has been noted that the procedures does not provide flexibility in adapting to the desired substrate thickness for practical realization. Eventually, the design relies on fine tuning of the lumped elements and successive optimization using circuit and full-wave simulation respectively. As a result, the demonstration of practical bandpass FSS is only up to third order. Other advantages and potential limitations of each design technique has been addressed above.

Chapter 3: **Modelling and Analysis of Frequency Selective Surfaces**

3.1 **Introduction**

This chapter presents the theory underlying analysis and design tools developed to enable the research during the thesis. Electromagnetics modelling of FSS enable characterization of scattered electromagnetic fields from the planar periodic structures. The results of the characterization facilitate the analysis and design of planar periodic structures. Electromagnetics modelling of FSS is based on Maxwell's equations, which involves solving mathematical formulations pertinent to the electromagnetic problem of periodic structure. The solutions to these formulation involves numerical techniques to accurately predict the frequency responses of the FSS structures. Various numerical methods have been developed over the years with the aim to improve the convergence rate in solving the differential or integral equations. These numerical techniques are Finite Element Method (FEM) [49], [50], Finite Difference Time Domain Method (FDTD) [51], [52], Transmission Line Method (TLM) [53], [54] and Method of Moments (MoM) [55], [56]. The fundamental idea of all these methods relies on the technique of discretization or meshes of the unknown electromagnetic property such as surface current and electric field [57].

Computational electromagnetic software packages such as CST, HFSS, COMSOL, FEKO and etc. offer wide range of solvers to compute scattered electromagnetic fields for general arbitrary shaped objects. Generally, these software packages incorporate computer-aided design (CAD) capabilities with the aforementioned numerical techniques. While these software packages could provide excellent accuracy with respect to experimental measurement, however their computational speed is compromised. This is because higher accuracy require finer discretization and as a result higher computational resources are required. Therefore, the performances of these numerical tools are assessed based on attributes such as computational efficiency and accuracy. However, these attributes cannot be satisfied simultaneously, hence, concession have to be made according to preferences.

Developing a numerical tool targeted for a particular structure would be preferable for the consideration of fast computation of the scattered fields and rapid design. For this reason, a numerical in-house tool has been developed and employed to some extent for

this work. The developed numerical tools covers only limited constituting FSS elements. Therefore, the disadvantages of the developed numerical tool compared with the aforementioned general purpose commercial packages are mainly due to the versatility of electromagnetics modelling for general shape objects.

Formulations of electric field integral equation (EFIE) and magnetic field integral equation (MFIE) for a single free standing FSS for both patch and aperture type were carried out respectively in this research. This study provide a fundamental analytical knowledge and background for multilayer FSS design. The metalized region of the arrays are assumed to be infinitely thin and perfectly conducting. The EFIE and MFIE are solved by using Galerkin MoM to determine the unknown electric and magnetic currents on the array [58]. The computed currents are then utilized to calculate the scattered transmission and reflection coefficients with respect to the incident field. Subsequently, the calculated scattered coefficients are employed to form the GSM, which is essential for analysis of cascaded FSS structures. Implementations of numerical computations are coded in MATLAB and the simulation results are validated with full wave EM commercial software CST. Equally important modelling technique for FSS is based on equivalent circuit model. This technique is built on filter theory, which help to establish an understanding of FSS behaviour with circuital analysis. Furthermore, filter theory provides a reliable intuitiveness for multilayer FSS design.

Section 3.2 presents the theory and formulation of two integral equations, which involve patch and aperture element arrays. Subsequently, numerical solutions for the integral equations based on Galerkin MoM are discussed. The application of GSM for multilayer periodic arrays analysis is reviewed in section 3.3. Comparison of the in-house simulation results with full-wave simulations are presented in section 3.4. While section 3.5 present the essential filter theories that are relevant for the modelling of multilayer FSS design.

3.2 Electric and Magnetic Field Integral Equations (EFIE & MFIE) Formulation

The following formulation is based on a single layer free standing two dimensional periodic array resides at $z = 0$ in between two infinite half space as illustrated in Figure 3.1. The left half space from the array is label as Region A and the remaining half space is label as Region B. Region A and Region B are filled dielectric with permittivity $\epsilon_{r_1}\epsilon_0$ and $\epsilon_{r_2}\epsilon_0$ respectively, but with the same permeability, μ_0. In order to derive the integral equations, total tangential electric and magnetic fields in both region A and region B have to be obtained. In region A, the total field constitute of incident and reflected fields. On the other hand, region B consist only of the transmitted fields. This is because of the infinite extend of dielectric half space, which is equivalent to a match termination [59].

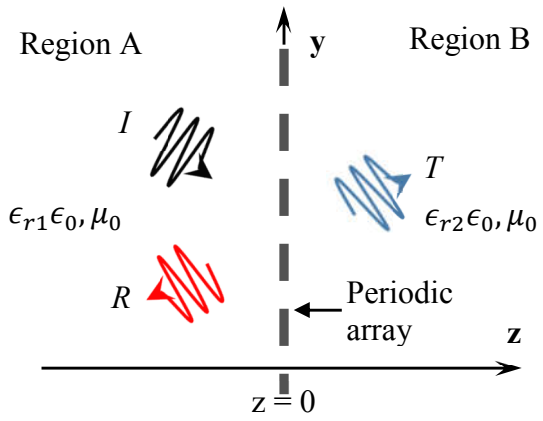

Figure 3.1 Side profile of the two-dimensional periodic planar array resides at z = 0.

The incident of electric and magnetic field can be expressed as summation of Floquet harmonics instead of a single plane wave [60]. Assuming there are (p, q) Floquet harmonics impending from Region A onto the array and as a result (n, m) Floquet harmonics scattered in both Region A and Region B respectively. Therefore, the total tangential electric and magnetic fields in both region A and B can be expressed as [58]

Region A:

$$\vec{E}_{A_{total}}(x,y,z) = \sum_{vpq} I_{v_{pq}} e^{-jk^A_{z_{pq}} z} \psi_{pq}(x,y)\vec{u}_{v_{pq}} + \sum_{vnm} R_{vnm} e^{+jk^A_{z_{nm}} z} \psi_{nm}(x,y)\vec{u}_{v_{nm}} \quad (3.1a)$$

$$\vec{H}_{A_{total}}(x,y,z) = \sum_{nm} Y^{A}_{v_{pq}} I_{v_{pq}} e^{-jk^{A}_{z_{pq}} z} \psi_{pq}(x,y)\left(\hat{z} \times \vec{u}_{v_{pq}}\right) - \sum_{nm} Y^{A}_{vnm} R_{vnm} e^{+jk^{A}_{z_{nm}} z} \psi_{nm}(x,y)\left(\hat{z} \times \vec{u}_{v_{nm}}\right) \tag{3.1b}$$

Region B:

$$\vec{E}_{B_{total}}(x,y,z) = \sum_{vnm} T_{vnm} e^{-jk^{B}_{z_{pq}} z} \psi_{nm}(x,y)\vec{u}_{v_{nm}} \tag{3.2a}$$

$$\vec{H}_{B_{total}}(x,y,z) = \sum_{vnm} Y^{B}_{v_{nm}} T_{vnm} e^{-jk^{B}_{z_{pq}} z} \psi_{nm}(x,y)\left(\hat{z} \times \vec{u}_{v_{nm}}\right) \tag{3.2b}$$

3.2.1 Electric Field Integral Equation (EFIE) Formulation

The subsequent formulation in this subsection assume the periodic array in Figure 3.1 as conducting elements printed on a dielectric substrate. Applying the boundary condition of field continuity for both electric and magnetic field at the interface z = 0 lead to [58]

$$\sum_{vpq} I_{vpq} \psi_{pq}(x,y)\vec{u}_{v_{pq}} + \sum_{vnm} R_{vnm} \psi_{nm}(x,y)\vec{u}_{v_{nm}} = \sum_{vnm} T_{vnm} \psi_{nm}(x,y)\vec{u}_{v_{nm}} \tag{3.3}$$

$$\sum_{vpq} Y^{A}_{vpq} I_{vpq} \psi_{pq}(x,y)\left(\hat{z} \times \vec{u}_{v_{pq}}\right) - \sum_{vnm} Y^{A}_{vnm} R_{vnm} \psi_{nm}(x,y)(\hat{z} \times \vec{u}_{vnm}) = \hat{z} \times \vec{J}_s(r,0) + \sum_{vnm} Y^{B}_{vnm} T_{vnm} \psi_{nm}(x,y)(\hat{z} \times \vec{u}_{vnm}) \tag{3.4}$$

Utilizing the orthogonal properties of Floquet modes, equations (3.3) – (3.4) can be further simplify by multiplying $\psi^{*}_{nm}(x,y)\vec{u}_{v_{nm}}$ and integrate over the unit cell area, A_{uc}, i.e. $\iint_{A_{uc}} \psi_{pq}(x,y)\,\psi^{*}_{nm}(x,y)ds = A_{uc}\delta_{nl}\delta_{mk}$, yield the following equations [58]

$$I_{v_{pq}}\delta_{np}\delta_{mq} + R_{vnm} = T_{vnm} \tag{3.5}$$

$$Y^{A}_{vpq} I_{vpq}\delta_{np}\delta_{mq} - Y^{A}_{vnm} R_{vnm} = Y^{B}_{v_{nm}} T_{vnm} + \frac{J_{vnm}}{A_{uc}} \tag{3.6}$$

where, J_{vnm} represent the induced spectral current of the conducting element [58]

$$\vec{J}_{nm} = \iint_{A_{uc}} \vec{J}_S(x,y,0)\,\psi^*_{nm}(x,y)ds \tag{3.7}$$

$$J_{v_{nm}} = \vec{J}_{nm} \cdot \vec{u}_{v_{nm}} \tag{3.8}$$

On the other hand, imposing the boundary condition of zero tangential electric fields for the conducting element at interface z = 0, produces [58]

$$\sum_{vpq} I_{vpq}\psi_{pq}(x,y)\vec{u}_{v_{pq}} + \sum_{vnm} R_{vnm}\psi_{nm}(x,y)\vec{u}_{v_{nm}} = \sum_{vnm} T_{vnm}\psi_{nm}(x,y)\vec{u}_{v_{nm}} = 0 \tag{3.9}$$

Manipulating algebraically for equations (3.5) and (3.6) to express the reflected and transmitted complex amplitudes in terms of incident and current terms yields [58]

$$R_{vnm} = I_{vpq}\delta_{np}\delta_{mq}\left(\frac{Y^A_{v_{pq}} - Y^B_{vpq}}{Y^A_{vpq} + Y^B_{vpq}}\right) - \frac{J_{v_{nm}}}{A}\left(\frac{1}{Y^A_{vnm} + Y^B_{vnm}}\right) \tag{3.10}$$

$$T_{vnm} = I_{vpq}\delta_{np}\delta_{mq}\left(\frac{2Y^A_{v_{pq}}}{Y^A_{vpq} + Y^B_{vpq}}\right) - \frac{J_{v_{nm}}}{A}\left(\frac{1}{Y^A_{vnm} + Y^B_{vnm}}\right) \tag{3.11}$$

Using the expression of reflection amplitude in (3.10), equation (3.9) can be rewritten as [58]

$$\sum_{vpq} I_{vpq}\left(1 + \Gamma^{AB}_{v_{pq}}\right)\psi_{pq}(x,y)\vec{u}_{v_{pq}} = \sum_{vnm} Z^{AB}_{v_{nm}}\frac{J_{v_{nm}}}{A}\psi_{nm}(x,y)\vec{u}_{v_{nm}} \tag{3.12}$$

where,

$$\Gamma^{AB}_{v_{pq}} = \frac{Y^A_{v_{pq}} - Y^B_{v_{pq}}}{Y^A_{v_{pq}} + Y^B_{v_{pq}}} \tag{3.13}$$

$$Z^{AB}_{v_{nm}} = \frac{1}{Y^A_{v_{nm}} + Y^B_{v_{nm}}} \tag{3.14}$$

3.2.2 Magnetic Field Integral Equation (MFIE) Formulation

The approach of the formulation in this case is similar to the previous section, however the periodic array of Figure 3.1 is now considered as aperture elements on a conducting plane. The boundary conditions for field continuity is still valid for aperture case, however, induced aperture field will be treated instead [58]. This implies

$$\sum_{vpq} I_{v_{pq}} \psi_{pq}(x,y)\vec{u}_{v_{pq}} + \sum_{vnm} R_{vnm}\psi_{nm}(x,y)\vec{u}_{v_{nm}} = \sum_{vnm} T_{vnm}\psi_{nm}(x,y)\vec{u}_{v_{nm}} = \vec{E}_a(x,y,0) \tag{3.15}$$

$$\sum_{vpq} Y^A_{vpq} I_{vpq}\psi_{pq}(x,y)\left(\hat{z}\times\vec{u}_{v_{pq}}\right) - \sum_{vnm} Y^A_{vnm} R_{vnm}\psi_{nm}(x,y)\left(\hat{z}\times\vec{u}_{v_{nm}}\right) = \sum_{vnm} Y^B_{vnm} T_{vnm}\psi_{nm}(x,y)\left(\hat{z}\times\vec{u}_{v_{nm}}\right) \tag{3.16}$$

Applying orthogonal properties of Floquet modes as before, equations (3.15) is simplify to

$$I_{v_{pq}}\delta_{np}\delta_{mq} + R_{vnm} = T_{vnm} = \frac{E^a_{vnm}}{A} \tag{3.17}$$

where, E^{ap}_{vnm} represent the induced field of the aperture

$$\vec{E}_{nm} = \iint_{A_{uc}} \vec{E}_a(x,y,0)\,\psi^*_{nm}(x,y)ds \tag{3.18}$$

$$E^a_{vnm} = \vec{E}_{nm}\cdot\vec{u}_{\mathrm{vnm}} \tag{3.19}$$

Substitute equation (3.17) into equation (3.16) produces the expression for MFIE

$$2\sum_{vpq} Y^A_{vpq} I_{vpq}\psi_{pq}(x,y)\left(\hat{z}\times\vec{u}_{v_{pq}}\right) = \sum_{vnm}\frac{1}{Z^{AB}_{vnm}}\frac{E^a_{vnm}}{A}\psi_{nm}(x,y)\left(\hat{z}\times\vec{u}_{v_{nm}}\right) \tag{3.20}$$

3.2.3 Method of Moment Solution

Expressions (3.9) and (3.20) represent the EFIE and MFIE respectively of a single layer periodic array that resides in between two infinite half space. The unknown electric current density $J_{v_{nm}}$ in equation (3.9) and unknown aperture field $E^{ap}_{v_{nm}}$ in equation (3.20) can be approximated using either entire domain basis function or sub-domain basis functions depending on the geometries of the elements. Entire domain basis functions are preferable for canonical geometry element (rectangular, circular, etc), while for non-canonical geometry shape element, sub-domain have to be used where a suitable set of entire domain basis functions may not be available. The unknown current density or unknown aperture field can be expressed as a series function of a linear combination product of k^{th} known vector basis function and k^{th} unknown complex amplitude which to be determined. Therefore, the basis function has a form [58], [59]

$$\vec{f}(x,y,0) = \sum_{k=1}^{k=N} c_k \vec{h}_k(x,y) \tag{3.21}$$

Where, $\vec{h}_k$ is the k[th] known vector basis function and c_k is the k[th] unknown complex amplitude that represent complex electric current or aperture field coefficients, depending on solving EFIE or MFIE respectively. Utilizing equation (3.21) for EFIE case in equation (3.9) yields [54]

$$\begin{aligned} &\sum_{vpq} I_{vpq}\left(1+\Gamma^{AB}_{v_{pq}}\right)\psi_{pq}(x,y)\vec{u}_{v_{pq}} \\ &= \sum_{vnm}\frac{Z^{AB}_{v_{nm}}}{A}\sum_{k=1}^{N} c_k\left[\iint_{A_{uc}} \vec{h}_k(x,y)\,\psi^*_{nm}(x,y)ds\right]\psi_{nm}(x,y)\vec{u}_{v_{nm}} \end{aligned} \tag{3.22}$$

Following Galerkin's procedure [61], a test function $\vec{h}^*_l(x,y)$ is multiply to equation (3.22) as inner product and integration over a unit cell area is performed. As a result, equation (3.22) transform into a general matrix equation which has a form [54]

$$Z_{in}\sum_{k=1}^{N} c_k = \sum_{vpq} I_{v_{pq}}\left(1+\Gamma_{v_{pq}}\right)\widetilde{H}^*_l(x,y) \tag{3.23}$$

where,

$$Z_{in} = \sum_{vnm} \frac{Z_{vnm}}{A_{uc}} \widetilde{H}_k(x,y)\widetilde{H}_l^*(x,y) \tag{3.24}$$

$$\widetilde{H}_k(x,y) = \iint_{A_{uc}} \vec{h}_k(x,y)\, \psi_{nm}^*(x,y) \cdot \vec{u}_{v_{nm}} ds \tag{3.25}$$

$$\widetilde{H}_l^*(x,y) = \iint_{A_{uc}} \vec{h}_l^*(x,y)\, \psi_{nm}(x,y) \cdot \vec{u}_{v_{nm}} ds \tag{3.26}$$

In a similar manner, exploiting the basis function in (3.21) for the MFIE case in equation (3.20) lead to [54]

$$\begin{aligned} &2\sum_{vpq} Y_{vpq}^A I_{vpq} \psi_{pq}(x,y) \left(\hat{z} \times \vec{u}_{v_{pq}}\right) \\ &= \sum_{vnm} \frac{1}{Z_{vnm}^{AB} A} \sum_{a=1}^{M} c_a \left[\iint_{A_{uc}} \vec{h}_a(x,y)\, \psi_{nm}^*(x,y) ds\right] \psi_{nm}(x,y)\left(\hat{z} \times \vec{u}_{v_{nm}}\right) \end{aligned} \tag{3.27}$$

Apply the aforementioned Galerkin's method as above with a testing function $\vec{h}_m^*(x,y)$, equation (3.27) can be rewritten a [54]

$$Y_M \sum_{a=1}^{M} c_a = \sum_{vpq} Y_{vpq} I_{vpq} \widetilde{H}_a^*(x,y) \tag{3.28}$$

where,

$$Y_M = \frac{1}{A_{uc}} \sum_{vnm} \frac{1}{Z_{vnm}} \widetilde{H}_a(x,y)\widetilde{H}_M^*(x,y) \tag{3.29}$$

$$\widetilde{H}_a(x,y) = \iint_{A_{uc}} \vec{h}_a(x,y)\, \psi_{nm}^*(x,y) \cdot \vec{u}_{v_{nm}} ds \tag{3.30}$$

$$\widetilde{H}_m^*(x,y) = \iint_{A_{uc}} \vec{h}_m^*(x,y)\, \psi_{nm}(x,y) \cdot \vec{u}_{v_{nm}} ds \tag{3.31}$$

Equations (3.23) and (3.28) have a general matrix form $[L][C] = [E]$. Thus, the unknown currents or aperture field represented by matrix $[C]$ can be obtained by conventional inverse matrix technique [54]

$$[C] = [L]^{-1}[E] \tag{3.32}$$

Equation (3.32) is an algebraic equation in matrix form, where $[L]$ is the linear operator of square matrix $(N \times N)$, $[C_N]$ is $(N \times 1)$ column matrix of the unknown complex coefficients to be determined and $[E]$ is the equivalent excitation source which has dimension matrix of $(N \times 1)$. Thus, the unknown complex coefficients can be easily determined by conventional matrix inversion or other iterative methods. The choice of the basis function determines the convergence of an accurate solution [58]. Entire domain basis functions are preferable choice for typical canonical shaped array elements such as dipole, rectangular, circular and etc by virtue of computational efficiency. However, for non-canonical shaped array elements, subdomain basis functions are usually employed, because a suitable set of entire domain basis functions may not be available [58]. The accuracy of the solution depends on the number of applied basis functions. Thus, once the current coefficients are computed from (3.32), it is then used to evaluate the reflection and transmission amplitudes respectively. The determined values of reflection and transmission amplitudes are then employed to form the Generalized Scattering Matrices (GSM).

3.3 **Generalized Scattering Matrix (GSM)**

GSM technique enable analysis of multilayer structure consist of stacked periodic arrays and dielectric substrates that interlay between each other. This technique utilizes matrix description that characterize the output of the scattered modes when subjected to incident Floquet modes. Therefore, for a structure consisting several interlay layers, the GSM of overall structure can be obtained by combining the GSMs of all layers. The overall GSM essentially provides the input–output characteristics with respect to the Floquet modes [59]. To illustrate the GSM approach, an exploded view of a three-layer periodic array structure (array–dielectric–array) is shown in Figure 3.2(a). The periodic arrays are assumed to be infinite with the same periodic spacing and lattice arrangement. Each layer is represented as a two-port network and are combined together to provide the GSM of the entire structure as depicted in Figure 3.2(b) [59].

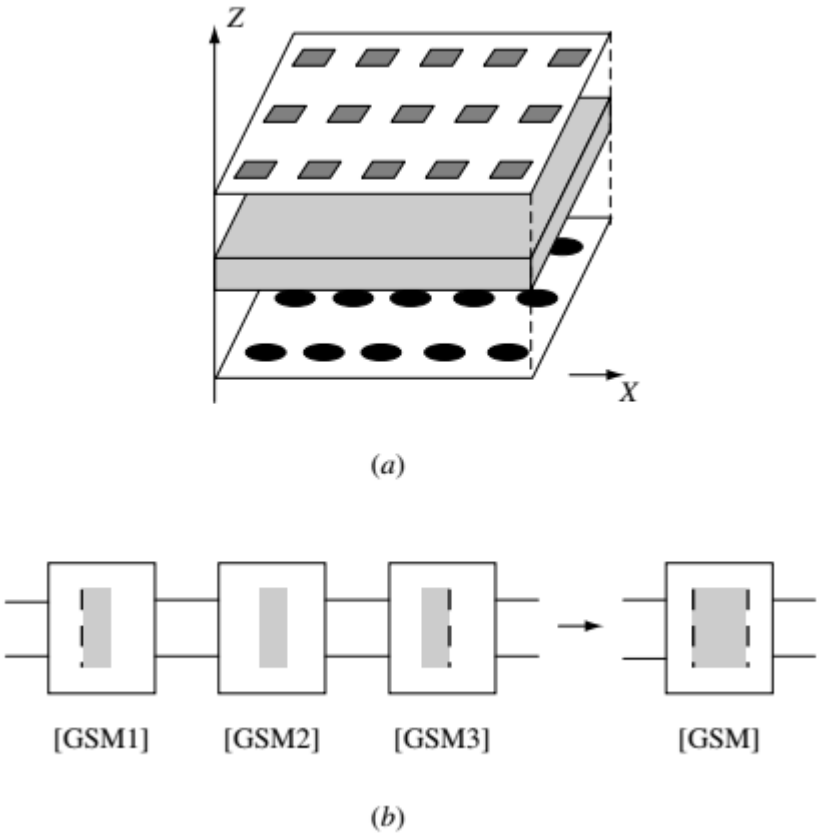

Figure 3.2 (a) Exploded view of a three-layer array structure. (b) Two-port network representation of each layer and its entire structure [59].

The definition of GSM of a layer is defined with the relation between incident and reflected voltages as [59]

$$\begin{bmatrix} a_1^- \\ a_2^- \end{bmatrix} = \begin{bmatrix} [S_{11}] & [S_{12}] \\ [S_{21}] & [S_{22}] \end{bmatrix} \begin{bmatrix} a_1^+ \\ a_2^+ \end{bmatrix} \tag{3.33}$$

The incident Floquet voltage waves the two sides of the ports are represented by $[a_1^+]$ and $[a_2^+]$, while $[a_2^-]$ and $[a_2^-]$ corresponds to the reflected voltage vectors. The [S] matrix on the right-hand side of (3.33) is called the GSM of the layer. The overall GSM consists of four sub-matrices, which are $[S_{11}]$, $[S_{12}]$, $[S_{21}]$, and $[S_{22}]$, respectively. In general, dissimilar number of modes are handled at the two ports, and usually $[S_{12}]$ and $[S_{21}]$ are not square matrices while $[S_{11}]$ and $[S_{22}]$ are square matrices of different orders. For example, if *N* and *M* number of modes are considered at port 1 and 2 respectively, the resulting matrix dimension for $[S_{12}]$ and $[S_{21}]$ are $(N \times M)$ and $(M \times N)$ order correspondingly. On the other hand, $[S_{11}]$ and $[S_{22}]$ would result in $(N \times N)$ and $(M \times M)$ order respectively [59].

3.4 **Numerical Results & Validation**

The following numerical results are based on single layer free standing capacitive and inductive FSS dipoles. The dipole is oriented along the y-direction for both the capacitive and inductive case. Essentially, dipole is a single resonant element and depends on the polarization of the incident field. Therefore for computation purposes, the electric field polarization of the incident wave is aligned along the dipole length for dipole patch case, while across the dipole length for aperture case. Plane wave incident (|p| = |q| = 0) normal to the array and 20 Floquet Space Harmonics (|n| = |m| = 20) are considered for the numerical computation. Five entire domain sinusoidal basis functions are used to evaluate the complex current coefficients. The numerical results of the developed in-house codes presented here are validated with CST simulations. The first FSS structure considered here is the capacitive dipole lie between two infinite half spaces as reported framework in [62]. The unit cell dimension associated to the dipole capacitive FSS is specified in Figure 3.3(a). Figure 3.3(b) illustrate the comparison between the in-house computation and CST simulation results for the far field reflection and transmission coefficients of the fundamental mode. Based on the dimension parameters shown in Figure 3.3, the frequency of the first grating lobe and resonant frequency is determined at 28.3 GHz and 22.14 GHz respectively for this FSS structure.

Example 1

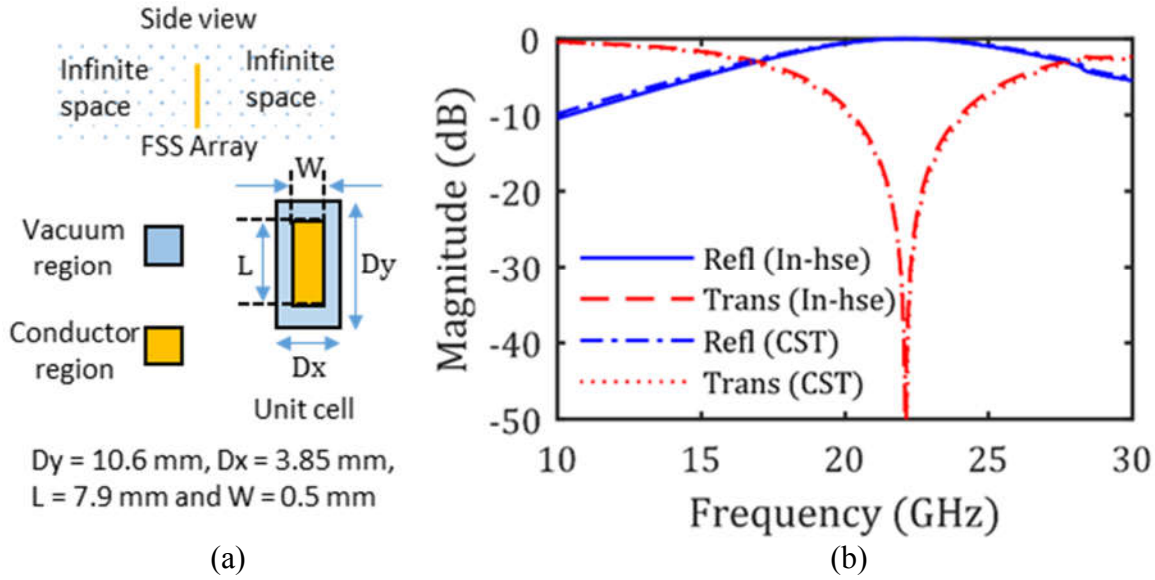

Figure 3.3: (a) The geometrical unit cell dimension of the capacitive dipole FSS. The conducting element is represented by yellow region, while blue region denote the vacuum. (b) Reflection & transmission frequency response of fundamental mode due to normal incident plane wave polarized in y-direction, i.e. $\vec{E}_i = \hat{y}E_y$ at spherical angles $\theta = 0°$ and $\phi = 0°$.

The next numerical case similarly involved a dipole slot FSS structure that lie between two infinite half space that follows an example given in [63]. The unit cell dimension of the dipole slot FSS is shown in Figure 3.4(a). Figure 3.4(b) show the comparison between the in house codes and CST computation for the far field reflection and transmission coefficient of the dipole slot under x-polarized plane wave excitation at normal incident. The resonant frequency is determined to be at 41.4 GHz.

Example 2

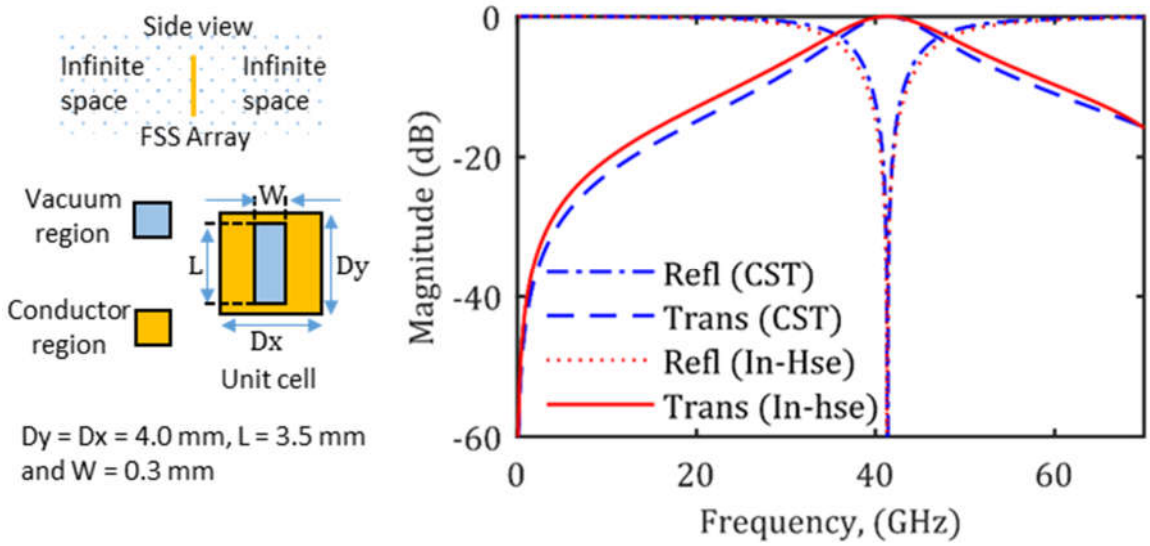

(a) (b)

Figure 3.4: (a) The geometrical unit cell dimension of the inductive dipole FSS. The conducting element is represented by yellow region, while blue region denote the vacuum. (b) Reflection & transmission coefficient of the fundamental mode due to normal incident plane wave polarized in x-direction, i.e. $\vec{E}_i = \hat{x}E_x$ at spherical angles $\theta = 0°$ and $\phi = 0°$.

The following numerical example involve a cascaded structure that consist a capacitive dipole FSS printed on a dielectric substrate with relative permittivity of 2.2 and thickness of 1.5 mm. Utilizing the GSM technique outlined in subsection 3.3, the spectral transmission and reflection coefficients are computed and illustrated in Figure 3.5, together with CST computation for the far field reflection and transmission coefficient of this FSS structure. The FSS structure resonate at 17.71 GHz under y-polarized plane wave excitation at normal incident.

Example 3

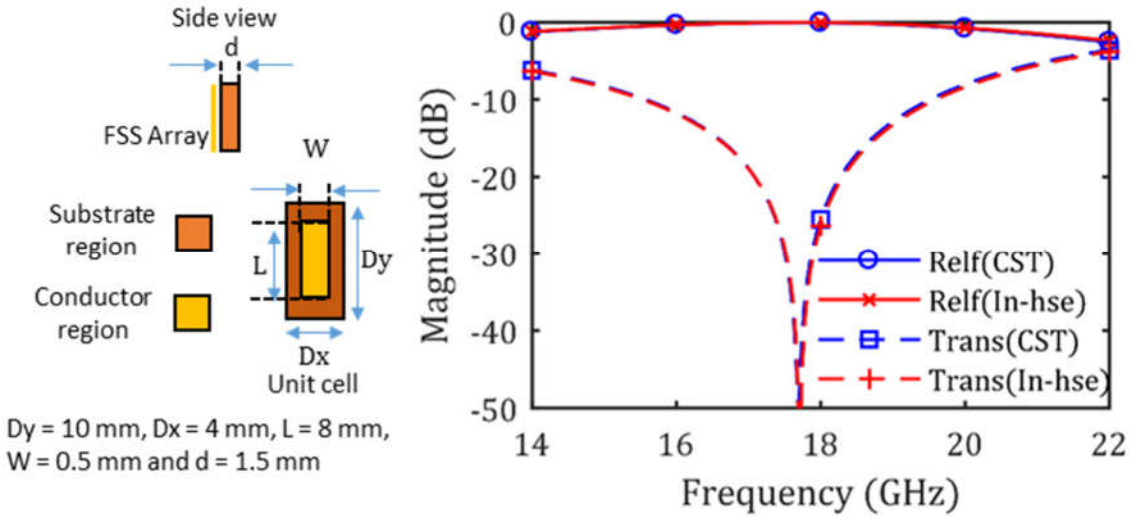

(a) (b)

Figure 3.5: (a) The geometrical unit cell dimension of the capacitive dipole FSS. The conducting element is represented by yellow region, while brown region denote the dielectric substrate. (b) Reflection & transmission frequency response of fundamental mode due to normal incident plane wave polarized in y-direction, i.e. $\vec{E}_i = \hat{y}E_y$ at spherical angles $\theta = 0°$ and $\phi = 0°$.

The last numerical case to demonstrate the validity of the developed in-house codes in this section follow an example from [63]. It involves a multilayer FSS, which is called Complementary FSS (CFSS) structure. CFSS comprises a capacitive and inductive dipole array printed on both side of a dielectric substrate. The architecture of the FSS structure and its geometrical dimensions are shown in Figure 3.6(a). The orientation of the capacitive and inductive dipole induces the CFSS to be resonant at 14.2 GHz and 49.2 GHz respectively, as shown in Figure 3.6(b). Transmission zero is observed at 24.65 GHz mainly due the array behaviour of being partially reflective at this frequency [63]. While, the location of the transmission zero as well as its bandwidth relies on the coupling between the FSS dipole array.

Table 3.1: Comparison of Computational Time

Example	Developed codes execution time [s]	CST execution time [s]
1	1.5	221
2	2.0	984
3	5.3	214
4	12	1230

Example 4

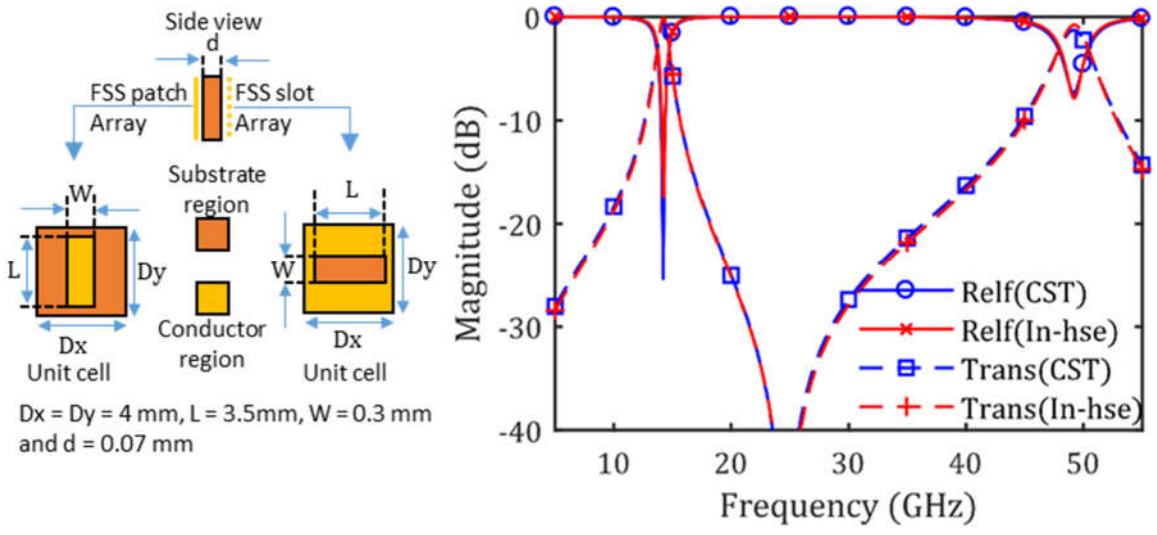

(a) (b)

Figure 3.6: (a) The geometrical dimensions of the complementary FSS consist of dipole patch and slot that are printed on both side of a substrate. The conducting element is represented by yellow region, while brown region denote the dielectric substrate. (b) Reflection & transmission coefficient of the fundamental mode due to normal incident plane wave polarized in y-direction, i.e. $\vec{E}_i = \hat{y}E_y$ at spherical angles $\theta = 0°$ and $\phi = 0°$.

Four numerical examples are presented in this section to demonstrate the performance of the developed codes. It is observable that the generated spectral responses from the developed codes for all the examples corroborate well with the commercial EM full-wave numerical package software CST. The setting of the mesh density control in CST is 20 steps per unit wavelength with minimum of 10 number of steps. The execution time of the developed codes are gauged by the built-in "tic toc" function in MATLAB, while the CST execution time is found based on the report generated in the log file of the solver result. Both the developed codes and CST execution time for all the four examples are tabulated in Table 3.1. One can concluded that the advantage of in-house codes over CST is the reduced computational time offered by the developed codes.

3.5 Filter Theory for Multilayer FSS Design

Filters are essentially frequency selective devices that are used in all frequency ranges. There are four types of filters, namely lowpass, highpass, bandpass and bandstop. Ideally, the characteristics of a filter should exhibit zero transmission loss, linear phase response within the required passband and infinite attenuation in the stopband regions. Practically, such ideal filter characteristics cannot be achieved. Therefore, practical filter design

usually relies on approximation to the ideal case within acceptable tolerances. Conventionally, insertion loss method is used to define the passband characteristics, which involved rational function approximation. Thus, the characteristics of a filter passband response depends on the employed rational function. Commonly employed rational functions are Chebysheff, Butterworth and Bessel. Filter design at low frequencies regime can be realized efficiently with lumped elements such as resistors, capacitors and inductors. This is only feasible when the operating wavelength is much longer that the physical circuits dimensions. However, at higher frequency, for example at millimetre or sub-millimetre operating wavelength, realization with conventional lumped elements would be impossible due to induced parasitic capacitances and inductances that affects the filter responses. Therefore, filter design at high frequency regime generally relies on distributed elements. Nevertheless, due to complex frequency responses of the distributed elements, generalized and complete synthesis procedures are non-existence [64]. Despite with the above mentioned design difficulties, there are number of useful techniques that have been developed in several frameworks such as [45], [65].

Insertion loss method provide a systematic procedure that enable control on the amplitude and phase of a filter over a desired frequency band. Therefore, the insertion loss method allows filter performance to be improved in a straightforward manner with the expense of a higher order filter. In what follows, basic theories and concepts such as inverter coupled bandpass, immittance inverter, and common circuit transformations are the focused theme and are discussed below. The aforementioned concepts and theories are essential to facilitate the design of multilayer FSS and also the proposed works in this thesis.

3.5.1 Low-Pass Prototype (LPP) Filter

Low-pass prototype (LPP) ladder network comprises of reactive elements arrange in cascaded configuration with shunt capacitor and series inductor alternatively as illustrated in Figure 3.7. LPP filter has normalized source resistance or conductance, $g_0 = 1$ and has characteristic of cut-off angular frequency at $\Omega_c = 1$ rad/s. While, the reactance elements denoted by g_i for $i = 1 \rightarrow n$, characterized the transfer function of the LPP network. Commonly known transfer functions available in the literatures are Butterworth, Chebyshev, Bessel and Gaussian. The LPP can be transformed to low pass, high pass,

bandpass and bandstop filters respectively via elements transformations. The elements transformations involve both frequency transformation and impedance scaling. Frequency transformation involved a frequency mapping of the LPP frequency to the required frequency band of the design filter, while impedance scaling is to adjust the impedance level of the filter network to the required source and load impedances. The frequency transformation and impedance scaling affect each reactance elements values of the LPP. A summary for the reactance elements transformation are shown in Table 3.2 [47].

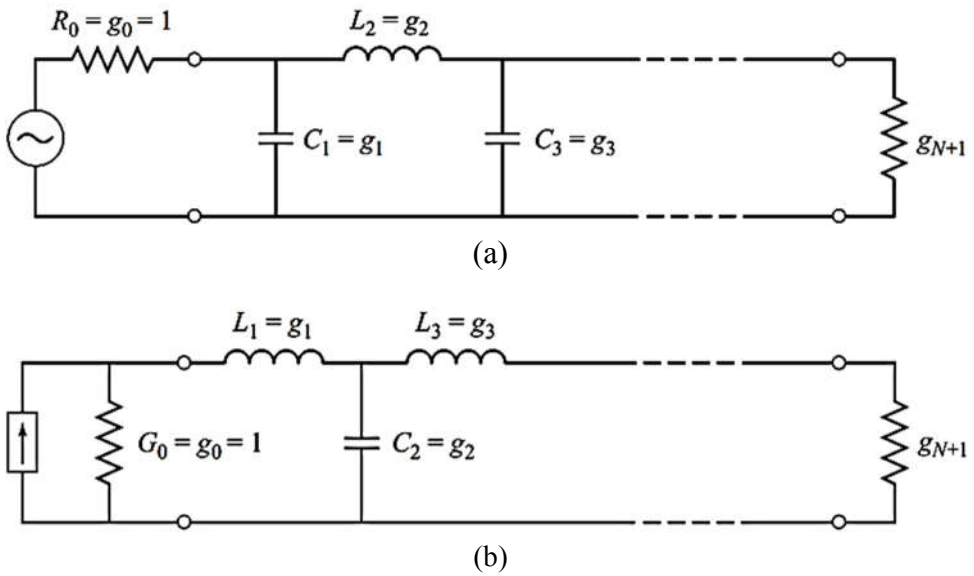

Figure 3.7 Low-pass prototype ladder network. (a) With first element shunt capacitor after the source resistor, g_0. (b) With first element series inductor after the source resistor, g_0 [47].

Table 3.2: Summary of Prototype Filter Transformations $\left(\Delta = \frac{\omega_2 - \omega_1}{\omega_0}\right)$ [47]

Low-Pass	High-Pass	Bandpass	Bandstop
$\frac{Z_o L}{\omega_c}$	$\frac{1}{\omega_c L Z_o}$	$\frac{LZ_o}{\omega_o \Delta}$ $\frac{\Delta}{\omega_o L Z_o}$	$\frac{1}{\omega_o L \Delta Z_o}$ $\frac{L \Delta Z_o}{\omega_o}$
$\frac{C}{Z_o \omega_c}$	$\frac{Z_o}{\omega_c C}$	$\frac{C}{\omega_o \Delta Z_o}$ $\frac{\Delta Z_o}{\omega_o C}$	$\frac{Z_o}{\omega_o C \Delta}$ $\frac{C\Delta}{\omega_o Z_o}$

Thus far, the element transformations result in classical lumped elements network conform the passband and stopband characteristics of the filter. Figure 3.8 illustrate a filter structure consist of series and shunt resonators arrangement after applying bandpass element transformation to the LPP network.

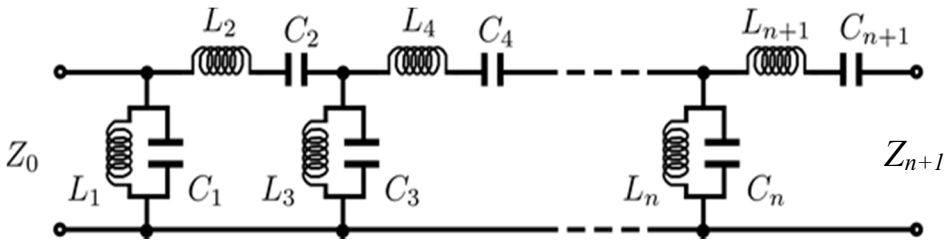

Figure 3.8 Classical lumped element bandpass filter

However, the realization of the classical filter with periodic array is not feasible in this form. Therefore, in order to implement a practical FSS spatial filter, it is desirable to transform the filter network consist only series or shunt elements network. This can be achieved using immittance inverter, which to be review in next subsection.

3.5.2 Coupled Resonator Filter with Immittance Inverter

Immittance inverter can be represented as a two port network that can perform either as an impedance or admittance inverter. Conventionally, impedance and admittance inverter are symbolized by *K* and *J* respectively. Any impedance or admittance connected at one port of the inverter network, the impedance or admittance seen looking at the other port is inverted and scale to real value of *K* or *J* with reference to the terminated impedance or admittance. This properties allows a series inductor can be model as a shunt capacitor with both ends terminated with a *J* inverter, and similarly a shunt capacitor is equivalent to a series inductor with both ends terminated with a *K* inverter, as illustrated in Figure 3.9 [45].

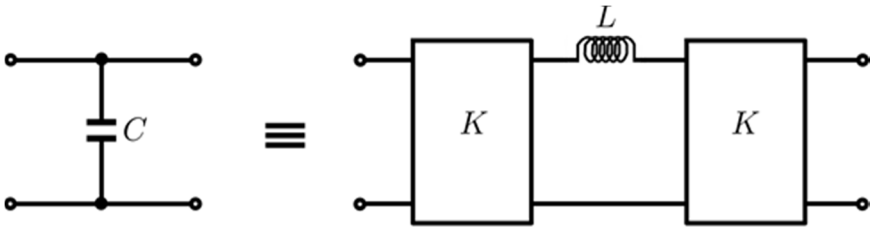

(a)

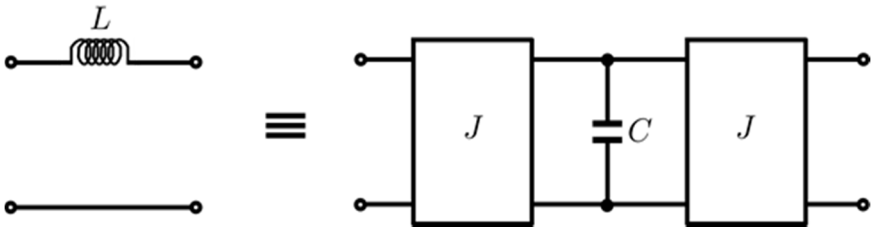

(b)

Figure 3.9 (a) Application of impedance inverter to convert a series inductor to a shunt capacitor. (b) Application of admittance inverter to convert a shunt capacitor to series inductor [45].

Utilizing the aforementioned properties, circuit filter of any form can be converted into a more appropriate arrangement for FSS implementation. For example, the classical lumped element bandpass filter topology shown in Figure 3.8, can be transformed to another topology consist only series resonators with impedance inverters or parallel resonators with admittance inverters, as illustrated in Figure 3.10. Basically, both topologies are equivalent, one being the dual to the other topology. The impedance, *Z* and admittance, *Y* for series and parallel resonator respectively can be expressed as [64]

$$Z = j\omega L\left(1 - \frac{\omega_0^2}{\omega^2}\right) \tag{3.34}$$

$$Y = j\omega C\left(1 - \frac{\omega_0^2}{\omega^2}\right) \tag{3.35}$$

where, ω_0 denote as the resonance frequency of the resonator.

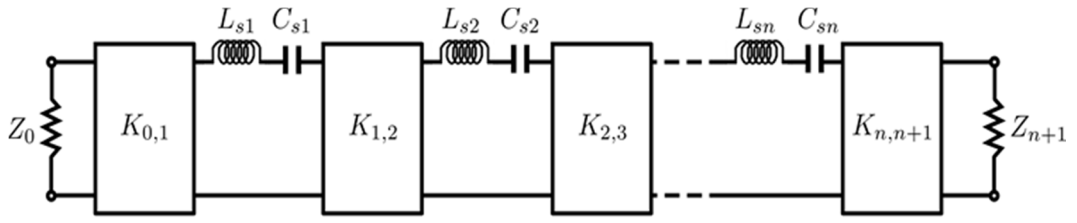

$$K_{0,1} = \sqrt{\frac{Z_0 \Delta\omega_0 L_{s1}}{\Omega_c g_0 g_1}}, \quad K_{i,i+1} = \frac{\Delta\omega_0}{\Omega_c}\sqrt{\frac{L_{si}L_{s(i+1)}}{g_i g_{i+1}}}\Bigg|_{i=1\rightarrow n-1}, \quad K_{n,n+1} = \sqrt{\frac{Z_{n+1}\Delta\omega_0 L_{sn}}{\Omega_c g_n g_{n+1}}}$$

$$C_{si} = \frac{1}{\omega_o^2 L_{si}}\Bigg|_{i=1\rightarrow n-1}$$

(a)

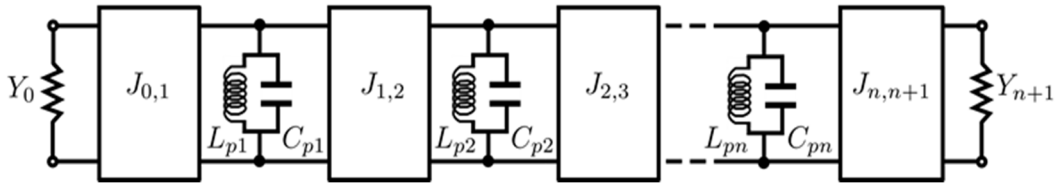

$$J_{0,1} = \sqrt{\frac{Y_0 \Delta\omega_0 C_{p1}}{\Omega_c g_0 g_1}},\ J_{i,i+1} = \frac{\Delta\omega_0}{\Omega_c}\sqrt{\frac{C_{pi}C_{p(i+1)}}{g_i g_{i+1}}}\Bigg|_{i=1\rightarrow n-1},\ J_{n,n+1} = \sqrt{\frac{Y_{n+1}\Delta\omega_0 C_{pn}}{\Omega_c g_n g_{n+1}}}$$

$$L_{pi} = \frac{1}{\omega_o^2 C_{pi}}\Bigg|_{i=1\rightarrow n-1}$$

(b)

Figure 3.10 (a) Bandpass filter consist only series resonators with impedance inverters (b) Bandpass filter consist only parallel resonators with admittance inverters [45].

Generally, it is more convenient to construct the resonators using distributed elements such as cavities, transmission lines and other relevant resonance structures. In practical cases, the distributed elements only approximate the reactances or suspectances of the *LC* resonator near resonance frequency. Hence, their implementations are only suitable for narrow to moderate bandwidth filter design [65]. Figure 3.11 show two topologies of generalized coupled resonator bandpass filter using distributed elements, which clearly seen as replacing the *LC* resonators in Figure 3.10. It is noteworthy that immittance inverter equations in Figure 3.11 are obtained using expressions in Figure 3.10 by replacing $\omega_0 L$ and $\omega_0 C$ with the slope parameters x_i and b_i [45].

Parameters in the equations associated with the *K*-inverters and *J*-inverters in Figure 3.10 and Figure 3.11 can be chosen arbitrary except for the g_i values that determined the passband and stopband characteristics of the filter. This implies that the impedance or admittance level of the resonators can be altered for design conveniences, in particular associated with the choices of resonators. Applied changes in impedance or admittance level of the resonator will not affect filter response as long as the immitance inverters equations indicated in Figure 3.14 holds. The properties of resonator are usually specified by their resonance frequency, ω_0 and slope parameter. Specifically, any form of resonator with series resonance characteristic, the reactance slope parameter, *x* is defined as [45]

$$x = \frac{\omega_0}{2}\frac{dX(\omega)}{d\omega}\Bigg|_{\omega=\omega_0} \tag{3.36}$$

While for resonator with parallel resonance, the susceptance slope parameter, *b* is defined as [45]

$$b = \frac{\omega_0}{2}\frac{dB(\omega)}{d\omega}\bigg|_{\omega=\omega_0} \tag{3.37}$$

The terms *X(ω)* and *B(ω)* that appears in (3.36) – (3.37) are associated with the series reactance and parallel susceptance of the resonator. In the case of series and parallel lumped *LC* resonator, their slope parameters is found equal to $\omega_0 L$ and $\omega_0 C$ respectively.

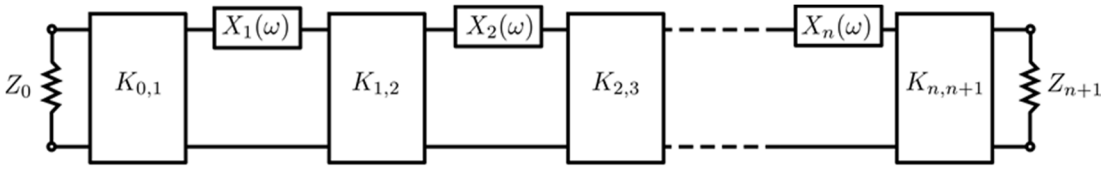

$$K_{0,1} = \sqrt{\frac{Z_0 \Delta x_1}{\Omega_c g_0 g_1}}, \qquad K_{i,i+1} = \frac{\Delta}{\Omega_c}\sqrt{\frac{x_i x_{i+1}}{g_i g_{i+1}}}\bigg|_{i=1\rightarrow n-1}, \qquad K_{n,n+1} = \sqrt{\frac{Z_{n+1}\Delta x_n}{\Omega_c g_n g_{n+1}}}$$

$$x_i = \frac{\omega_0}{2}\frac{dX_i(\omega)}{d\omega}\bigg|_{\omega=\omega_0}$$

(a)

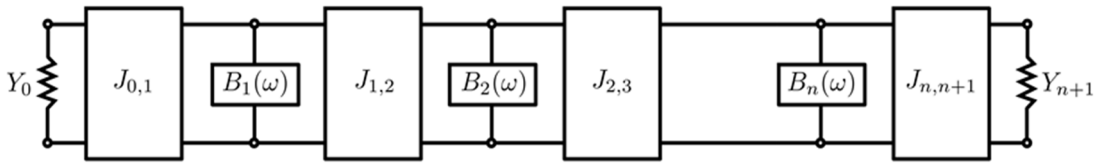

$$J_{0,1} = \sqrt{\frac{Y_0 \Delta b_1}{\Omega_c g_0 g_1}}, \qquad J_{i,i+1} = \frac{\Delta}{\Omega_c}\sqrt{\frac{b_i b_{i+1}}{g_i g_{i+1}}}\bigg|_{i=1\rightarrow n-1}, \qquad J_{n,n+1} = \sqrt{\frac{Y_{n+1}\Delta b_n}{\Omega_c g_n g_{n+1}}}$$

$$b_i = \frac{\omega_0}{2}\frac{dB_i(\omega)}{d\omega}\bigg|_{\omega=\omega_0}$$

(b)

Figure 3.11 Generalized resonator coupled bandpass filter (a) with impedance inverter (b) with admittance inverter [45].

3.5.3 Practical Realization of Immittance Inverter

The ABCD matrix of an ideal impedance inverter can be expressed as [45]

$$\begin{bmatrix} A & B \\ C & D \end{bmatrix} = \begin{bmatrix} 0 & \mp jK \\ \pm\dfrac{1}{jK} & 0 \end{bmatrix} \tag{3.38}$$

While, ideal admittance inverter have ABCD matrix

$$\begin{bmatrix} A & B \\ C & D \end{bmatrix} = \begin{bmatrix} 0 & \pm\dfrac{1}{jJ} \\ \mp jJ & 0 \end{bmatrix} \tag{3.39}$$

Ideal impedance and admittance inverter have properties of phase shift with odd multiple of $\pm\pi/2$. Quarter-wave transmission line with characteristic impedance, $K = Z_c$ or characteristic admittance, $J = Y_c$ performed as impedance or admittance inverter respectively. However, their implementations are normally targeted for narrowband filters [45].

Figure 3.12 illustrate lumped element circuits that perform as impedance and admittance inverters, which are usually suitable to be applied to filter topology shown in Figure 3.10. These circuits are frequency dependent and comprises of negative elements. When these circuits are applied as immittance inverter, the negative elements will be absorbed into adjacent lumped element resonator of the filter. As a result, the final circuit consist of tuned resonator coupled by series or shunt lumped elements across the filter network. Figure 3.13 demonstrate applications of tuned coupled resonators by a single reactive element [64].

Another commonly employed immittance inverter comprises of mixed lumped and distributed element as depicted in Figure 3.14 are suitable to be implement for filter topology shown in Figure 3.11. These inverters involved a lumped element embedded into a transmission line of electrical length, ϕ with characteristic impedance, Z_0 or characteristic admittance, Y_0. Similarly, when these circuits are applied to the filter with distributed elements, the electrical length contributed by these inverters are absorbed into adjacent distributed elements with the same characteristic impedance or admittance [45].

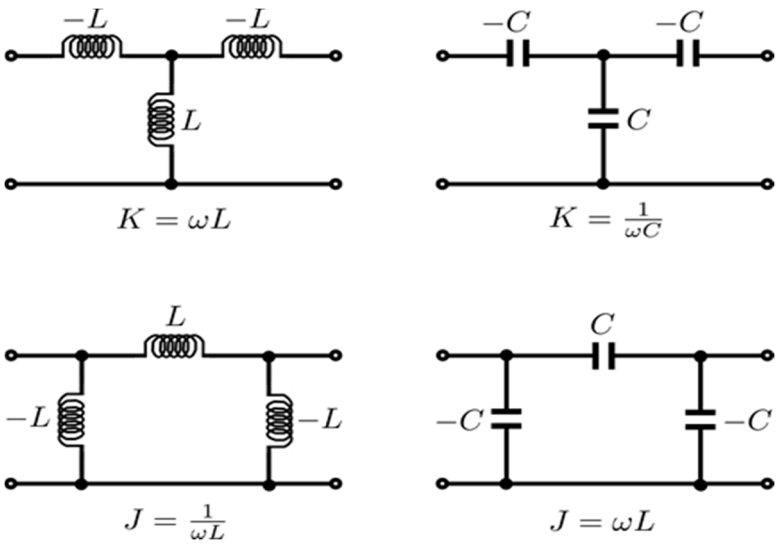

Figure 3.12 Lumped element inverters [64]

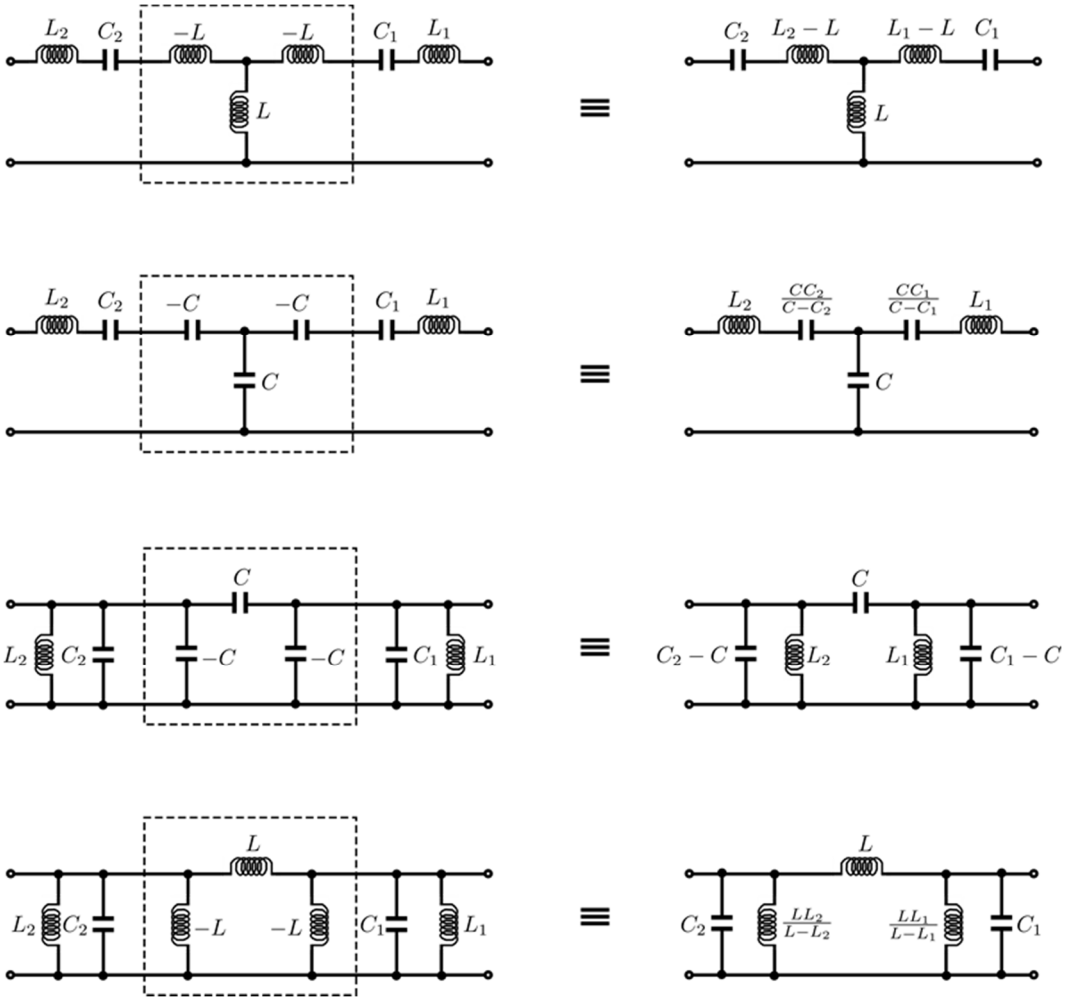

Figure 3.13 Coupled resonator circuits realized by lumped element inverters [64].

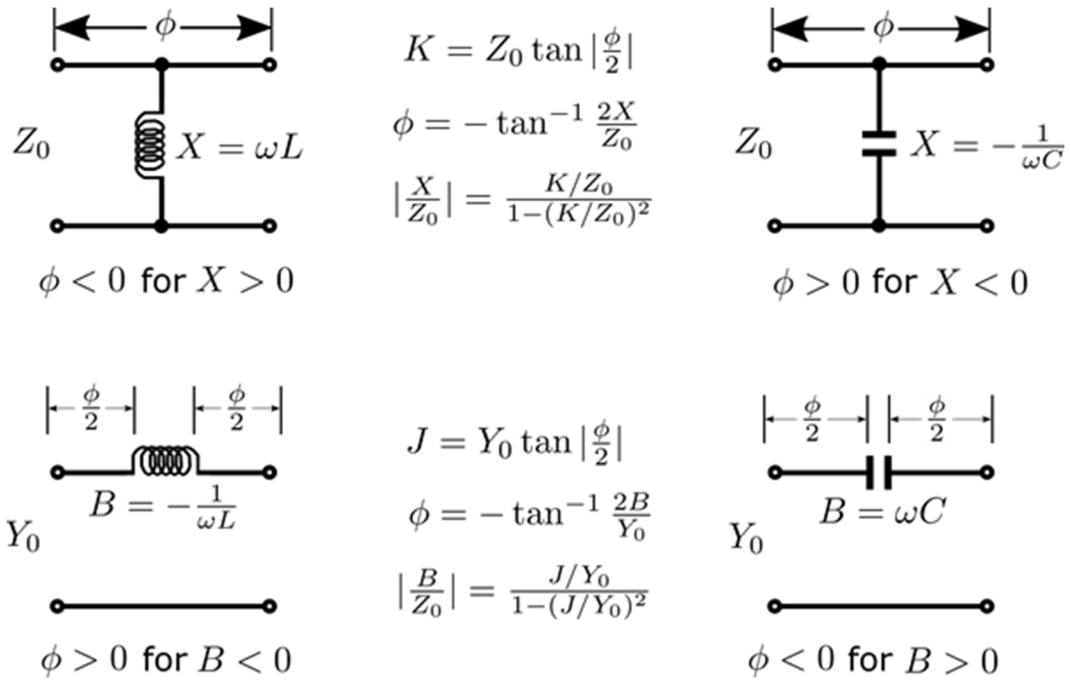

Figure 3.14 Mixed lumped and distributed element immittance inverters [45].

3.6 **Summary**

The objective of this chapter is to provide theory and modelling techniques for 2-D periodic structures that were studied for this research work. Section 3.2 present the formulations of EFIE and MFIE, which stem from the application of mode matching with boundary condition for both electric field and magnetic field are presented. These integral equations are then solved using numerical technique known as Galerkin's MoM. The purpose of this numerical procedure is to determine the unknown induced currents or aperture fields of the elements array. The accuracy of the method depends on the number of basis functions involved in the calculations. While section 3.3 covered brief theory of GSM, which is essential for modelling and analysis for cascaded periodic structures. Developed in-house codes based on theories in section 3.2 and 3.3 are validated by comparing its computed spectral responses with numerical EM software CST for four numerical examples, are presented in section 3.4. The performance of the developed codes agrees well with CST and has the advantage of computational speed over CST. Finally, the fundamental filter theories that are important for modelling of multilayer FSS structures are presented in section 3.5. In particular, practical implementation of immittance inverter for coupled filter topologies are discussed.

Chapter 4: Asymmetrical Impedance Inverter for Quasi-Optical Bandpass Filter with Transmission Lines of Fixed Length

4.1 Introduction

Quasi-optical (QO) filters are engineered surfaces that selectively transmit or reflect different frequencies of incoming free-space waves. They are employed in diverse applications including e.g, earth observation radiometry [3], [66], antenna radomes [67], [68], and imaging systems [69]. Dichroic film is an established technology for QO filter realization applicable more commonly at optical [70], [71] and THz frequencies [72], [73]. At lower frequencies, periodic metallized patterns supported by dielectric substrates, as depicted in Figure 4.1 are preferred technology for QO filters. They benefit from mature manufacturing processes (e.g. photolithography), thereby providing significant design flexibility with the geometries that can be etched. This class of structures has been used for the implementations of several QO filters [9], [74], [75] and other derivative applications such as absorber [76]–[78], polarizer [19], [27], [79] and as beam splitters [80]–[82] across RF and mm-wave frequencies.

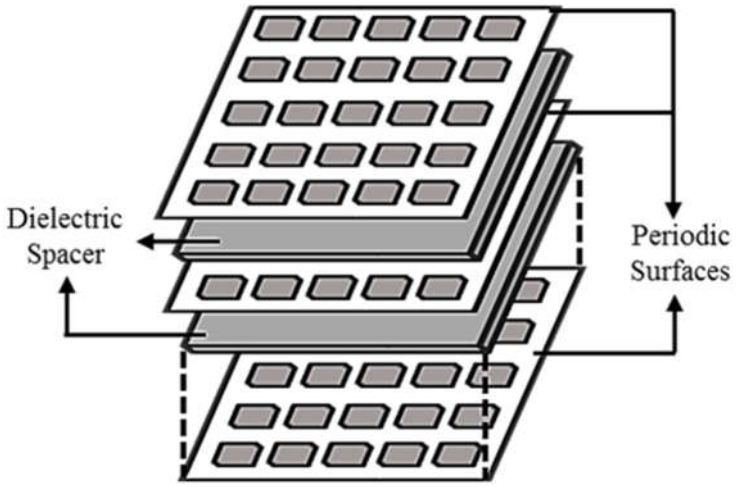

Figure 4.1 General topology of quasi-optical filters comprises of multilayer stacked two dimensional periodic surfaces.

A single planar periodic metallized array is able to provide up to first-order bandpass response. This response may not be suitable for more broadband applications or for those application out of band rejection level is desirable. In order to achieve higher order responses and to address the poor out of band rejection level, multiple arrays can be

cascaded. One classical approach for the design of higher order responses relies on coupling successive resonant metallized arrays with quarter-wavelength spacers, which act as admittance inverters [11].

To elaborate further on the limitations of the approach presented in [11] it is noted that the aforementioned filter implementations rely on admittance inverter (J-inverter) values that are all equal to the characteristic impedance of the quarter-wavelength spacers ($J = Z_0$) [65]. The coupling coefficient value, p, between resonators (n, n+1) is therefore determined by the reactance slope parameters, x of the resonators according to [65]

$$p = \frac{K}{\sqrt{x_n x_{n+1}}} \tag{4.1}$$

While full-wave techniques allow the estimation of the reactance slope parameter associated with a 2D periodic metallized pattern, the inverse problem of designing a unit cell geometry that produces a specific reactance slope parameter value and a given resonant frequency is not trivial. As a result, this implementation is not readily compatible with a deterministic synthesis technique, thereby posing challenges for transfer functions of higher order and heavily relying on the experience of the designer. Additional challenges related to the aforementioned implementation strategy arise as operating frequencies shift to mm-waves and beyond. On one hand, as the operating frequency increases the etching tolerances of conventional processes give rise to the increased degradation of the unloaded quality factor (Q-factor), which deteriorates the filter selectivity. Moreover, and as discussed in more detail in [83], this approach has ultimate limits in the upper values of the reactance slope parameters than can be achieved. As a result, the realization of narrowband transfer functions becomes cumbersome.

An alternative realization based on resonant metallized arrays is described in [33], [34]. This design strategy exploits transmit and received antennas coupled to a planar filter implementation where frequency selectivity is performed. These filters, printed in a non-radiating layer between two antenna layers, can be tailored to achieve higher order filter response. This approach has enabled simple and compact QO filter structure. The frequency response demonstrated in [33], [34] shows high selectivity and promising polarization characteristics. While recognizing the advantages of this approach, it is noted

that the realization of this class of filter also strongly dependent the substrate thickness and elaborate manufacturing processes to achieve desirable external Q-factor.

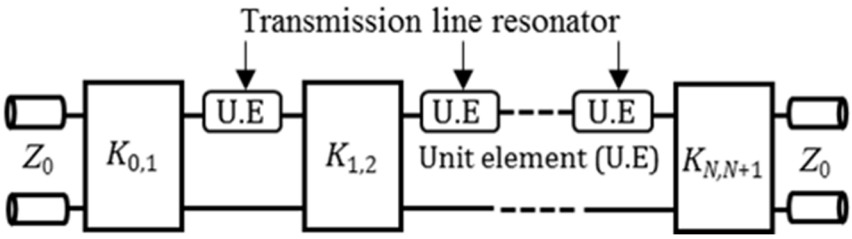

Figure 4.2 Generalized impedance inverter (K-inverter) structure with series coupled-resonator bandpass filter circuit.

More recently based on the framework presented in [38], the authors exploited direct coupled cavity filter prototype that enables the deterministic design of this class of filters using classical equivalent circuit approaches, e.g. [65]. According to this approach, the inverters are realized as periodic grids and the resonator as half-wavelength cavities. This strategy enables higher quality factors even at mm-wave frequencies and the realization of narrowband filters. This approach however leads to the requirement for each dielectric spacer to have a custom electrical length. This poses practical difficulties in the manufacturing as dielectric spacers at custom thicknesses are not readily available in standard PCB technology. Consequently, the demonstration of QO filters with this approach is limited up to 2nd order response [38].

Addressing the aforementioned challenge, in this chapter a new class of impedance inverters is proposed that enable direct coupled cavity filter prototypes with transmission lines of predefined fixed length. The proposed impedance inverters employ an asymmetrical π-equivalent network comprising a transmission line and two shunt susceptances at pre-selected electrical separation. It is demonstrated that by careful selection of the shunt susceptances, this class of impedance inverters enable filter prototypes where all resonators have a fixed and predefined length. Exploiting this class of prototypes, it is demonstrate for the first time experimental results using conventional PCB technology for a QO filter based on direct coupled transmission line resonators of 4th order. The rest of the chapter is organized as follows; section 4.2 reviews the classical impedance inverter prototype for direct coupled filters and introduces the proposed impedance inverter circuit. Subsequently by means of a specific example involving a filter at 15 GHz with fractional bandwidth 5%, section 4.3 demonstrates the design procedure for the proposed filters and validates the design by means of experimental results.

4.2 **Theory**

4.2.1 Definition of the Problem

Impedance inverters enable bandpass filter prototypes with only series resonators, thereby facilitating the implementation of direct-coupled cavity filters using the generic equivalent prototype shown in Figure 4.2. By definition, an impedance inverter is a two-port network, which presents at its input an impedance value, Z_{in} , that is dual of the load impedance, Z_L, connected at the other end [45]:

$$Z_{in} = \frac{K^2}{Z_L} \tag{4.2}$$

where the scaling factor, K, is a real value referred to as characteristic impedance of the inverter. As discussed in the introduction, a quarter wavelength transmission line acts as a narrowband impedance inverter. Another commonly employed impedance inverter comprises a susceptance symmetrically embedded in a transmission line of electrical length ϕ, Figure 4.3(a). Substituting for the circuit of Figure 4.3(a) to the prototype of Figure 4.2 leads to the equivalent prototype shown in Figure 4.3(b) for the direct coupled filter.

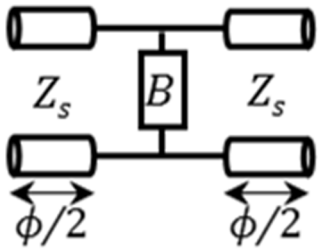

$$\left|\frac{B}{Y_s}\right| = \frac{1}{(K/Z_s)} - \left(K/Z_s\right)$$

$$\phi = \tan^{-1}\left[\frac{1}{(B/Y_s)}\right]$$

(a)

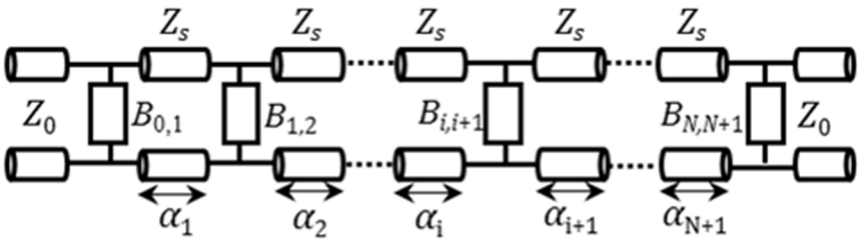

$$\alpha_i = \pi + \frac{\phi_{i-1,i}}{2} + \frac{\phi_{i,i+1}}{2}$$

(b)

Figure 4.3 (a) Equivalent circuit for a typical impedance inverter involving a shunt suscptance between transmission lines of a given electrical length. (b) Bandpass filter network exploiting the impedance inverter of Fig. 3(a). Note that the i^{th} resonators absorb electrical lengths associated with impedance inverters $K_{i-1,i}$ and $K_{i,i+1}$ and hence has electrical length α_i.

As shown in Figure 4.3(a), the *K*-value and the electrical length, ϕ, are dependent on the susceptance value. For illustration purposes, the range of K-values and phase, ϕ values are plotted against the normalized susceptance, B/Y_S for a range of ([-10, 10]) in Figure 4.4.

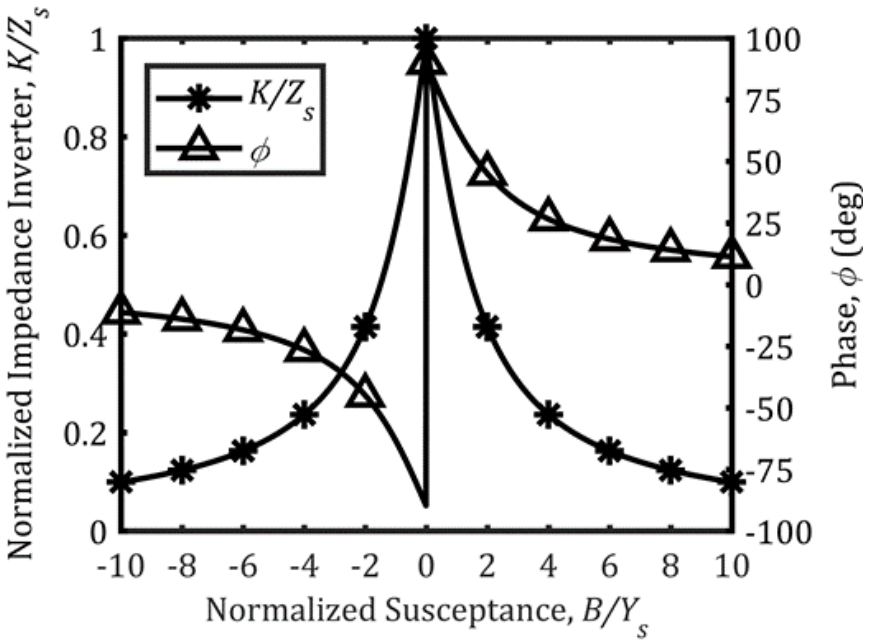

Figure 4.4 Graphical representation for a range of attainable numerical values for the normalized impedance inverter, K/Z_s and phase, ϕ of the classical impedance inverter in Fig. 3(a) for different value of normalized susceptance, B/Y_S.

It is observable from Figure 4.4 that when the susceptance is capacitive (positive value), the phase ϕ is positive. Contrarily, the phase, ϕ is negative for an inductive susceptance (negative value). The electrical length, ϕ contributed by the impedance inverter is

absorbed within the adjacent resonators (which are otherwise half wavelength) such that the electrical length, α_i of the i^{th} transmission line resonator in Figure 4.3(b) becomes

$$a_i = \pi + \frac{\phi_{i-1,i} + \phi_{i,i+1}}{2} \tag{4.3}$$

For filters of higher order, *K*-values across the filter respect the symmetry condition:

$$K_{(i,i+1)} = K_{(N+1-i,N+2-i)} \qquad for\ i = 0, 1, \ldots N/2 \tag{4.4}$$

but otherwise vary for different values of *i*. Consequently, the length of the resonator in the equivalent prototype of Figure 4.3(b) respect the symmetry

$$\alpha_i = \alpha_{(N+1-i,N+2-i)} \qquad for\ i = 0, 1, \ldots N/2 \tag{4.5}$$

but otherwise vary for different values of *i*. As discussed in the introduction the requirement for resonators with custom dimensions places challenges in the cost efficient implementation of direct coupled cavity QO filters based on periodic metallized arrays.

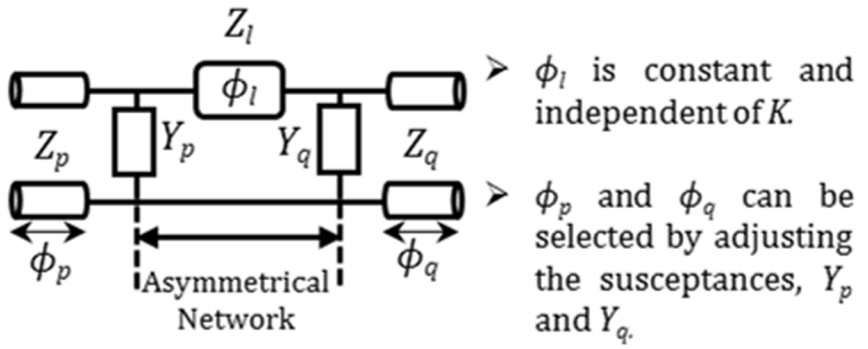

(a)

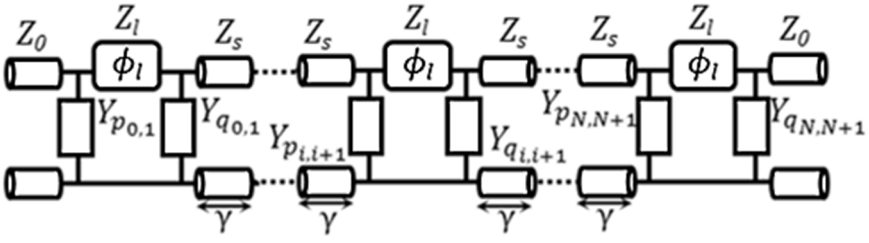

(b)

Figure 4.5 (a) The proposed asymmetrical impedance inverter consists of transmission line with electrical length, ϕ_l and susceptance of Y_p and Y_q that can be implemented using either lumped capacitor or inductor. (b) Bandpass filter network using proposed asymmetrical impedance inverter where now all resonators have the same length as all resonators are absorbing a constant phase. Note also that ϕ_l is constant for all impedance inverters.

4.2.2 Principles of the Proposed Solution

The proposed solution targets the derivation of an equivalent prototype that maintains the compatibility with the classical direct coupled prototype shown in Figure 4.2, where all transmission lines have a fixed length that can be predetermined within a given range. As will be shown in the remaining of this chapter, this can be achieved by exploiting the impedance inverter of Figure 4.5(a). This asymmetrical circuit comprises a transmission line with a predefined electrical length, ϕ_l, in a π-network layout involving shunt susceptance, Y_p and Y_q. Transmission lines of electrical lengths of ϕ_p and ϕ_q are respectively considered at the two ends of the network. We are considering the generic case, where the network is terminated with different characteristic impedances, Z_p and Z_q, respectively.

Unlike the classical impedance inverter network of Figure 4.3(a), which has a single degree of freedom (namely the selection of the shunt susceptance, B) the proposed asymmetrical impedance inverter equivalent network provides two degrees of freedom, namely the selection of the two shunt susceptance, Y_p and Y_q. Using this equivalent circuit, a required equivalent *K*-value from the prototype of Figure 4.2 can be obtained from several combinations of Y_p and Y_q values. Significantly, each pair of Y_p and Y_q values leads to a different pair of electrical lengths ϕ_p and ϕ_q. This flexibility enables to select the electrical lengths associated with the i^{th} resonator such that

$$\phi_{q(i-1,i)} + \phi_{p(i,i+1)} = c\ (constant) \tag{4.6}$$

Once this condition is satisfied, and upon substituting for the proposed *K*-inverter of Figure 4.5(a), the original prototype of Figure 4.2 is transformed to the one shown in Figure 4.5(b). In this prototype all resonators have electrical length of

$$\gamma = \pi + c \tag{4.7}$$

The quasi-optical implementation of Figure 4.5(b) therefore will only require two values of the electrical lengths of the dielectric spacers, namely ϕ_l and γ. It is noted that the values of both ϕ_l in the equivalent network of Figure 4.5(a) and γ in equation (4.7) can be preselected within a range of values, such that the final equivalent prototype in Figure 4.5(b) matches the available dielectric spacers.

In practice, when low-cost manufacturing is targeted using conventional PCB technologies it is convenient to select for ϕ_l the value that corresponds to the preferred dielectric substrate. This will allow etching the *K*-inverter on either side of a doubly metallized PCB substrate and therefore there is no additional complexity in the dielectric stack when compared e.g. with ([38], Fig. 4). The choice of γ relies on the design priorities; it can be based on the availability of high permittivity substrates when profile and angular stability are performance priorities or the availability of low permittivity low loss substrates (e.g. honeycomb or foam) when high unloaded Q is preferred.

4.2.3 Analysis of the proposed Inverter

The equivalent *K*-value from the prototype of Figure 4.5(a) can be obtained by exploiting its ABCD matrix to establish a relation with the ideal *K*-type inverter. In particular, the ABCD matrix for the asymmetrical two-port network shown in Figure 4.5(a), can be express as:

$$\begin{bmatrix} A & jB \\ jC & D \end{bmatrix} = [T]_p \times \begin{bmatrix} A & jB \\ jC & D \end{bmatrix}_{\pi} \times [T]_q \tag{4.8}$$

where the middle term represents the ABCD matrix of the asymmetrical π-network:

$$\begin{bmatrix} A & jB \\ jC & D \end{bmatrix}_{\pi} = [Y]_p \times [T]_l \times [Y]_q \tag{4.9}$$

In (4.8) and (4.9), $[T]_m$ ($m = p, l, q$) are the ABCD matrices associated with transmission lines:

$$[T]_m = \begin{bmatrix} \cos\phi_m & jZ_m \sin\phi_m \\ j\dfrac{1}{Z_m}\sin\phi_m & \cos\phi_m \end{bmatrix} \tag{4.10}$$

while $[Y]_{p,q}$ is the ABCD matrix of the shunt susceptances

$$[Y]_{p.q} = \begin{bmatrix} 1 & 0 \\ jY_{p,q} & 1 \end{bmatrix} \tag{4.11}$$

In order for the network of Figure 4.5(a) to act as *K*-type inverter, the following condition, which accounts for the entire K-inverter equivalent circuit, should hold

$$\begin{bmatrix} 0 & jK \\ \frac{j}{K} & 0 \end{bmatrix} = \begin{bmatrix} A & jB \\ jC & D \end{bmatrix} = [T]_p \times \begin{bmatrix} A & jB \\ jC & D \end{bmatrix}_\pi \times [T]_q \tag{4.12}$$

It can be shown that equation (4.12) holds once electrical lengths at either ends of the network of Figure 4.3(b) are selected as [84]:

$$\phi_p = \frac{1}{2}\tan^{-1}\left[\frac{2\left(\frac{BD}{Z_q} - ACZ_q\right)}{A^2\frac{Z_q}{Z_p} + \frac{B^2}{Z_pZ_q} - C^2Z_pZ_q - D^2\frac{Z_p}{Z_q}}\right] \tag{4.13}$$

$$\phi_q = \frac{1}{2}\tan^{-1}\left[\frac{2\left(\frac{BA}{Z_p} - DCZ_p\right)}{D^2\frac{Z_p}{Z_q} + \frac{B^2}{Z_pZ_q} - C^2Z_pZ_q - A^2\frac{Z_q}{Z_p}}\right] \tag{4.14}$$

The normalized impedance inverter, κ is obtained as

$$\kappa = \frac{K}{\sqrt{Z_pZ_q}} = \frac{1}{|S_{21}|}\left(1 - \sqrt{1 - |S_{21}|^2}\right) \tag{4.15}$$

where, S_{21} is refer as the transmission coefficient of the asymmetrical two port network, which can be expressed as [84]

$$\frac{1}{|S_{21}|^2} = 1 + \frac{1}{4}\left[\left(A\sqrt{\frac{Z_q}{Z_p}} - D\sqrt{\frac{Z_p}{Z_q}}\right)^2 + \left(\frac{B}{\sqrt{Z_pZ_q}} - C\sqrt{Z_pZ_q}\right)^2\right] \tag{4.16}$$

Equations (4.8) - (4.15) enable to identify pairs of (Y_p, Y_q) which produce a required *K*-value. Importantly, each pair of (Y_p, Y_q) corresponds to different values for the pair of electrical lengths (ϕ_p, ϕ_q); as a result a range of (ϕ_p, ϕ_q) pairs is available for every *K*-value that is prescribed in the equivalent circuit. Since the resulting set of equations are non-linear and transcendental, it is practical to solve these equations numerically. This is reported in Figure 4.6, which plots the equivalent normalized *K*-values and associated electrical lengths, (ϕ_p, ϕ_q) when the shunt susceptance (Y_p, Y_q) vary in the range ([-0.03, 0.03], [-0.03, 0.03]). The plots is produced for a prescribed ϕ_l value of 40°. As shown in

Figure 4.6, for each pair of (Y_p, Y_q) there is a corresponding pair of electrical lengths (ϕ_p, ϕ_q) for which the equivalent circuit of Figure 4.5(a) acts as a K-inverter. It is noted that with appropriate selection of (Y_p, Y_q) this network can produce the entire range of the normalized $\kappa \in [0, 1]$. It is further noted that the plot of Figure 4.6 exhibits symmetry associated with the exchange of $Y_p \leftrightarrow Y_q$, hence the 2nd and 4th quadrants of Figure 4.6 are equivalent. Unlike the conventional impedance inverter, the proposed impedance inverter allows flexibility to select range of (ϕ_p, ϕ_q) that can satisfy equation (4.6). Of more practical interest are regions of Figure 4.6, where the phases of either side of the K-inverter are of opposite sign. This is so since for this range $\phi_{q_{i-1,i}}$ will be of opposite sign to $\phi_{p_{i,i+1}}$ and therefore equation (4.6) can be satisfied for a wider range of (ϕ_p, ϕ_q) values. By means of a design example, the next section demonstrate how the Figure 4.6 (and other equivalent figures for different values of ϕ_l) can be used to derive a filter prototype as in Figure 4.5(b), where all transmission line resonators have a fixed and predefined electrical length, γ.

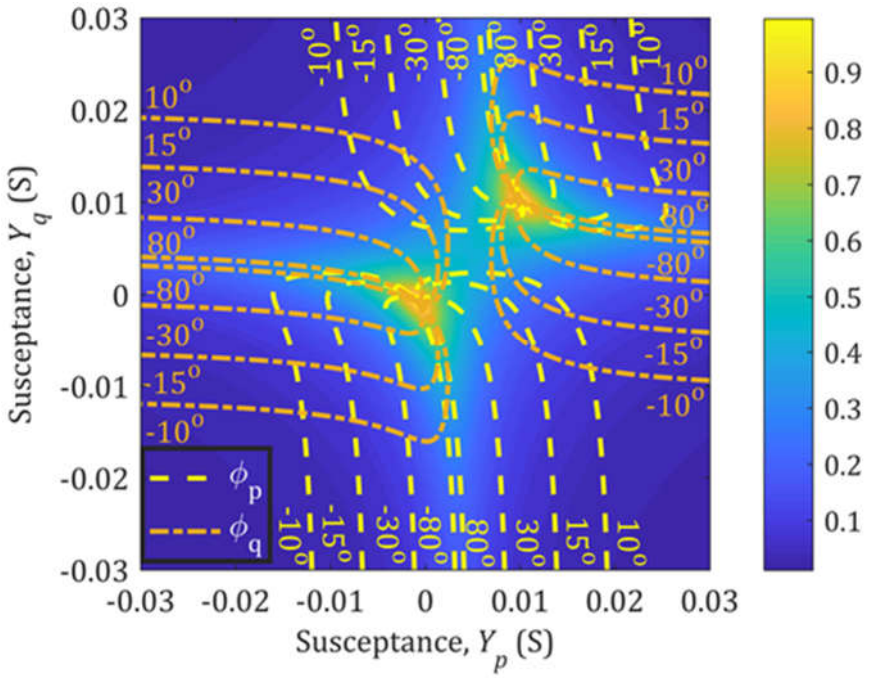

Figure 4.6 Color-map and the contour lines represent the normalized impedance inverter and phases of ϕ_p and ϕ_q respectively for the range of susceptance values assigned to Y_p and Y_q.

4.3 **Design Examples and Validation of Experimental Result.**

In this section a fourth-order Chebyshev bandpass filter with passband ripple of 0.01 dB and fractional bandwidth 5% is used as an example to illustrate the synthesis of the filter

based on the proposed impedance inverter. We are targeting an implementation of this filter at 15 GHz utilizing dielectric spacers with dielectric constant, $\varepsilon_r = 1.07$ as resonators. This is compatible with the available 31-HF Rohacell Foam of thickness, $h = 10$ mm. At this operating frequency, the electrical length, γ of the dielectric spacer corresponds to 186.19° for all four resonators. Commercially available laminates from Taconic TLY-5, with dielectric constant, $\varepsilon_r = 2.2$ and thickness, $l = 1.5$ mm are used to support the two periodic arrays that implement the shunt susceptances, Y_p and Y_q. Using this as an example, subsection 4.3.1 illustrates a generic design methodology for this class of filters. Numerical and experimental results are reported in subsection 4.3.2 to validate the performance.

4.3.1 Design Procedure

Following the theoretical framework reported in [84], the normalized impedances for this prototype can be found as $\kappa_{0,1} = \kappa_{4,5} = 0.3264$, $\kappa_{1,2} = \kappa_{3,4} = 0.08491$ and $\kappa_{2,3} = 0.06236$. The key step of the design procedure is to identify the pairs of (Y_p, Y_q) for each K-inverter and simultaneously equation (4.7) holds for $\gamma = 186.19°$. The electrical length ϕ_l is 40° at the operating frequency and therefore the numerical results reported in Figure 4.6 can directly be utilized. In order to facilitate the design, Figure 4.7 is constructed with the data presented in Figure 4.6, where now contours of κ-values are plotted against the associated phases (ϕ_p, ϕ_q). Only three contours are plotted corresponding to the three κ-values for this prototype. As discussed in the previous subsection, the solutions is searched for the range where the phases of ϕ_p and ϕ_q are opposite sign. The range of (ϕ_p, ϕ_q) from the 2nd or the 4th quadrant of Figure 4.7 are thus the region of practical interest. The design aim now reduces to the identification of points across the three contours where equation (4.6) holds for $c = 6.19°$ for all values of i. Without loss of generality, it is selected that the phases of ϕ_p and ϕ_q are negative and positive respectively, hence this implies the relevant range in this case falls on the 2nd quadrant of Figure 4.7.

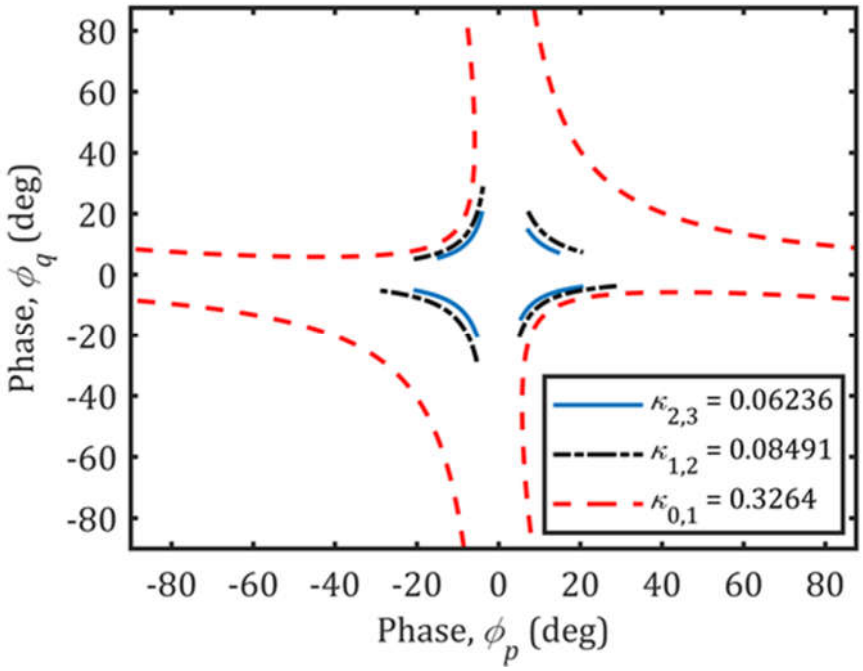

Figure 4.7 Contour of ϕ_p and ϕ_q for specific normalized impedance inverter values.

It is noted that while the highest value of $\kappa_{0,1}$ = 0.3264 provides a wide range of compatible phases (ϕ_p, ϕ_q), the lower values $\kappa_{1,2} = \kappa_{3,4}$ = 0.08491 and $\kappa_{2,3}$ = 0.06236 are limited to a narrower range of associated values for (ϕ_p, ϕ_q). Since equation (6) entails phases associated with successive phase inverters, it is practical to limit the search for solutions in the minimum common range of (ϕ_p, ϕ_q) for all K-inverters. From Figure 4.7 the minimum common range can identified in the range -20° ≤ ϕ_p ≤ 0° and 0° ≤ ϕ_q ≤ 20°. The design can commence with an arbitrary choice of a point along the $\kappa_{0,1}$ contour within this range. Subsequently, from this selected point, the other phases of ϕ_p and ϕ_q for the adjacent impedance inverters are then computed according to the constant phase condition in (4.6). Once all points are identified, the equivalent inductance and capacitance values can be obtained from Figure 4.6. It is noted that unlike the prototype of Figure 4.3(b), the prototype of Figure 4.5(b) obtained by this procedure is not symmetric. This is due to the fact that the K-inverters are not symmetric. Moreover, clearly this procedure leads to an infinite number of solutions to the design problem; the range of capacitance & inductance values that satisfy the design problem is linked with the common range of (ϕ_p, ϕ_q) for all K-inverters. The designer can exploit this flexibility to minimize geometrical tolerances during the implementation of the QO filter.

In order to demonstrate the procedures outlined above, the pair of ($\phi_{p_{0,1}}$, $\phi_{q_{0,1}}$) = (-9.91°, 14.45°) from the contour line correspond to $\kappa_{0,1}$ are selected. Thus, using equation (4.6),

the phase of ϕ_p associate to $\kappa_{1,2}$ is calculated as $\phi_{p_{1,2}}$= -8.26°. Using this methodology, the other phases of ϕ_p and ϕ_q are computed and are listed in Table 4.1 below.

Table 4.1 Computed Phases of Φ_P and Φ_Q

Index	(0,1)	(1,2)	(2,3)	(3,4)	(4,5)
ϕ_p	-9.91°	-8.26°	-6.41°	-6.41°	-9.91°
ϕ_q	14.45°	12.6°	12.6°	16.10°	14.45°

Once the points (ϕ_p, ϕ_q) are identified for all the impedance inverter from Figure 4.7, these are mapped to required susceptances Y_p and Y_q that provide the equivalent κ-inverter value. As mentioned above this can be achieved with the aid of Figure 4.6, which for illustration purposes is redrawn in Figure 4.8. In particular, Figure 4.8 shows the corresponding region of interest where the three κ-value contours involved in the design are plotted together with the identified contours for ϕ_p and ϕ_q. The identified points of (ϕ_p, ϕ_q) for all κ-inverters are marked and as anticipated, they lie at the points where the three related curves cross. The corresponding susceptance values can be read from this plot and is tabulated in Table 4.2 below.

Table 4.2 Susceptance Values For Fourth-Order Filter

Index	(0,1)	(1,2)	(2,3)	(3,4)	(4,5)
Y_p	0.0005	-0.011	-0.016	-0.015	0.0005
Y_q	0.0075	0.0146	0.0152	0.0124	0.0075

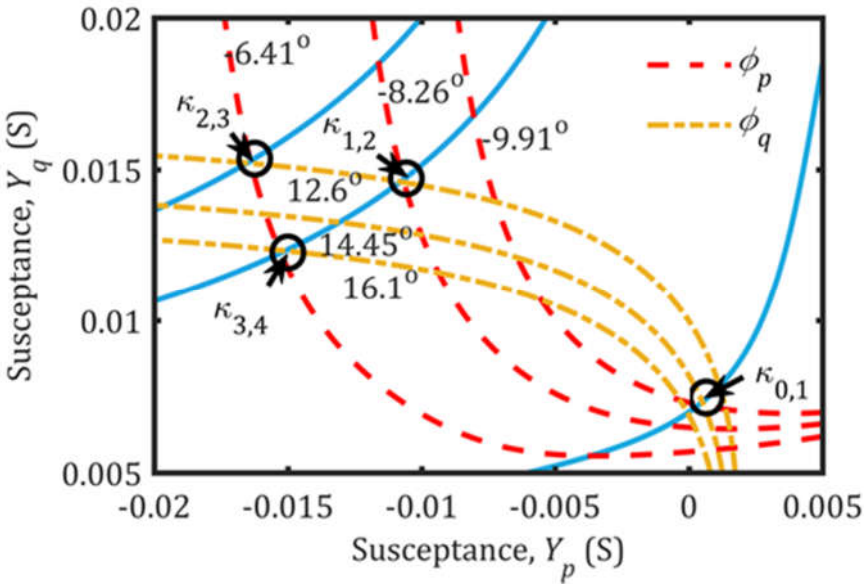

Figure 4.8 Contour lines for specific normalized impedance inverter values and selected phase of ϕ_p and ϕ_q based on Figure 4.6.

As observed above, the equivalent circuit derived with this process is no longer symmetrical; this can be seen since the $\kappa_{1,2}$ point is not identical with the $\kappa_{3,4}$. The asymmetry is attributed to the asymmetry of the K-inverter equivalent circuit in Figure 4.5(a). Using the contour curves in Figure 4.8 and with the aid of equivalent circuit in Figure 4.5(a) one can obtain the inductances and capacitances values by tuning slightly to match the transmission coefficient and reflection phases of the required impedance inverter.

4.3.2 Numerical and Experimental Results

Once the appropriate susceptance, Y_p and Y_q are concluded, the final step is to translate these susceptances to an equivalent physical structure for realization. The asymmetrical network can be physically realized with standard PCB prototyping, where the laminate represent the transmission line sandwiched between two parallel lumped components that can be printed on the two sides of the laminates. The lumped components are the capacitor and inductor that can be implemented with two-dimensional printed periodic array of capacitive patches and inductive wire grids respectively. Figure 4.9 shows typical array unit cells that perform as an inductor and a capacitor respectively when illuminated by a plane wave. The shaded and unshaded area represent conductor and dielectric domain respectively. The orientation of the printed conductor is symmetrical, making it insensitive for both vertical and horizontal polarization plane waves. For simplicity, the periodicity, *D*, is kept the same for both arrays. Closed form expressions for the dimensions of both capacitive and inductive arrays are available in the literature [48]:

$$C_{i,i+1} = \varepsilon_0 \varepsilon_{i,i+1} \frac{2D}{\pi} \ln\left(\csc\left[\frac{\pi s_{i,i+1}}{2D}\right]\right) \tag{4.17}$$

$$L_{i,i+1} = \mu_0 \mu_{i,i+1} \frac{D}{2\pi} \ln\left(\csc\left[\frac{\pi w_{i,i+1}}{2D}\right]\right) \tag{4.18}$$

The physical and geometrical dimension of respective inductive or capacitive FSS are first primarily estimated using equations (4.17) and (4.18). The geometrical dimension are then optimized using EM full wave simulation to match the frequency response of the equivalent circuit of the asymmetrical structure according to Figure 4.5(a). The fine-tuned

shunt susceptance values and final dimension of the FSS are presented in Table 4.3 below. A schematic of the stack-up is shown in Figure 4.10.

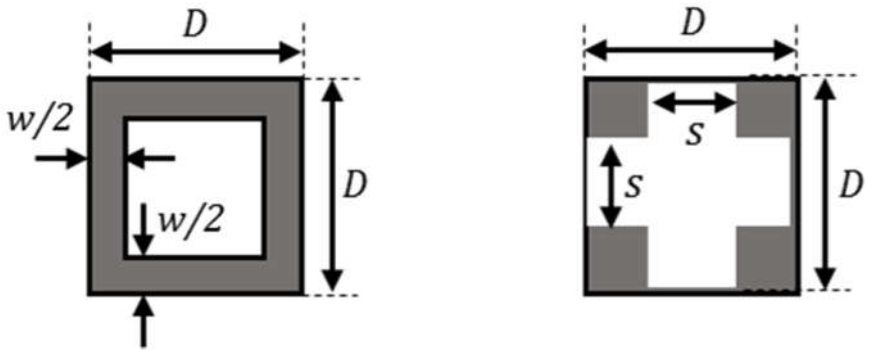

Figure 4.9 (a) FSS unit cell for inductive grids. (b) FSS unit cell capacitive grids.

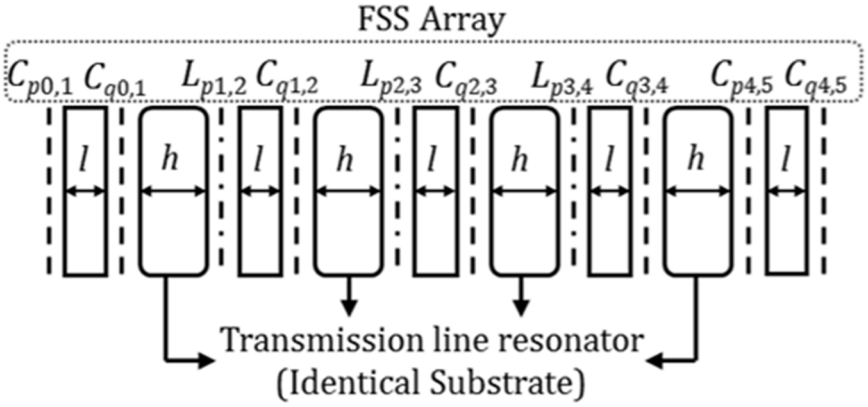

Figure 4.10 Side view of the fourth order bandpass FSS filter depicting relative position of the FSS array, substrate and spacer resonator.

Table 4.3 Circuits Parameters and Geometrical Dimensions for Fourth-Order Filter

Circuit Parameters				
$C_{p0,1}$ (pF)	$C_{q0,1}$ (pF)	$L_{p1,2}$ (nH)	$C_{q1,2}$ (pF)	$L_{p2,3}$ (nH)
0.0049	0.0775	0.992	0.1556	0.6456
$C_{q2,3}$ (pF)	$L_{p3,4}$ (nH)	$C_{q3,4}$ (pF)	$C_{p4,5}$ (pF)	$C_{q4,5}$ (pF)
0.1613	0.6929	0.1300	0.0034	0.0766
Geometrical Dimensions (mm)				
$s_{p0,1}$	$s_{q0,1}$	$w_{p1,2}$	$s_{q1,2}$	$w_{p2,3}$
3.35	0.66	1.16	0.18	1.57
$s_{q2,3}$	$w_{p3,4}$	$s_{q3,4}$	$s_{p4,5}$	$s_{q4,5}$
0.16	1.52	0.28	3.50	0.67
D	l	h		
5.2	1.5	10		

A prototype was fabricated for experimental validation using standard PCB lithography. The periodic arrays and the spacers are bonded together by using Repositionable 75 adhesive spray from 3M^{TM}. The adhesive spray has negligible impact on electrical length of the transmission lines. The overall thickness of the designed filter in terms of guided wavelength is $2.457\lambda_g$, while the unit cell dimensions are $0.26\lambda_0$. A photograph of the fabricated prototype is shown in Figure 4.11.

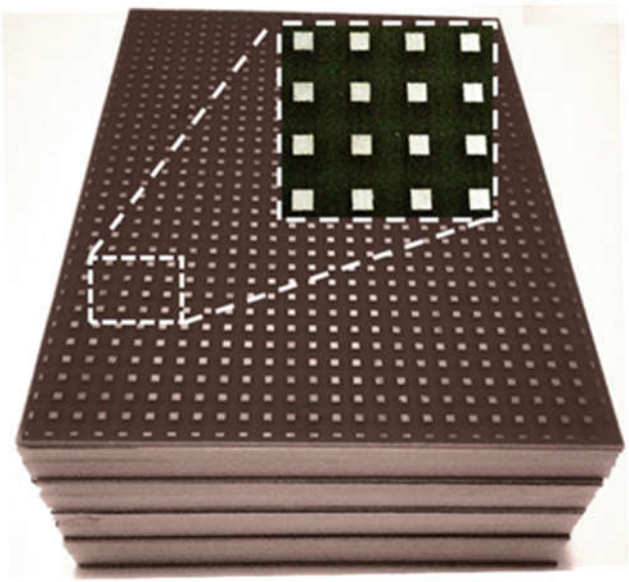

Figure 4.11 Photograph of the fabricated 4th order QO bandpass filter prototype. The inset shows a zoomed area of the first layer array.

The fabricated prototyped was experimentally characterized using standard free space techniques as described e.g. in [36]. In particular, the QO filter is placed in a window of an otherwise absorbing surface. Horn antennas placed on either side of the quasi-optical filter acting as transmitter and receiver accordingly were used for the characterization of the transmission coefficient. The experimental setup is show in Figure 4.12. Time-gating is applied to reduce the effect of standing waves. The measured results are shown in Figure 4.13, where for comparison the full-wave results as well as the results obtained from the synthesized circuit are superimposed. Good agreement with the full wave results is obtained. Some discrepancies are attributed to manufacturing tolerances and also on the measurement imperfections; they are commensurate with measurements reported in the literature [36], [85]. Figure 4.13 also depicts the full-wave and circuit responses for the reflection coefficient, S_{11}. The experimental arrangement to measure reflection is not as trivial, since the transmit and receive horns should physically overlap. However, the overall agreement of the measurement with the simulated results in terms of the transmission coefficient validate the synthesis procedure.

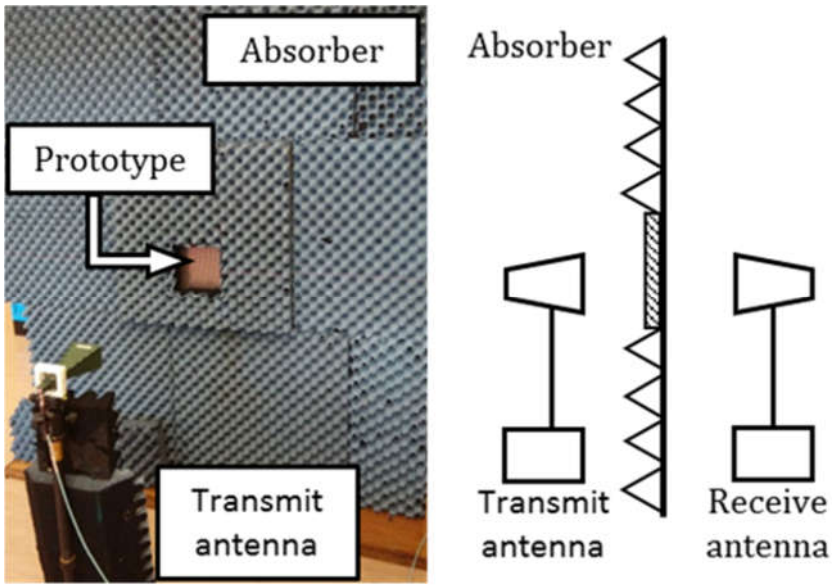

Figure 4.12 (a) Photograph of the measurement setup to characterize the transmission coefficient, S_{21} of the 4th order QO bandpass filter, where the prototype is positioned at the window opening between the transmit and received antennas. (b) Side view of the measurement setup illustrating the relative position of the transmit and received antennas.

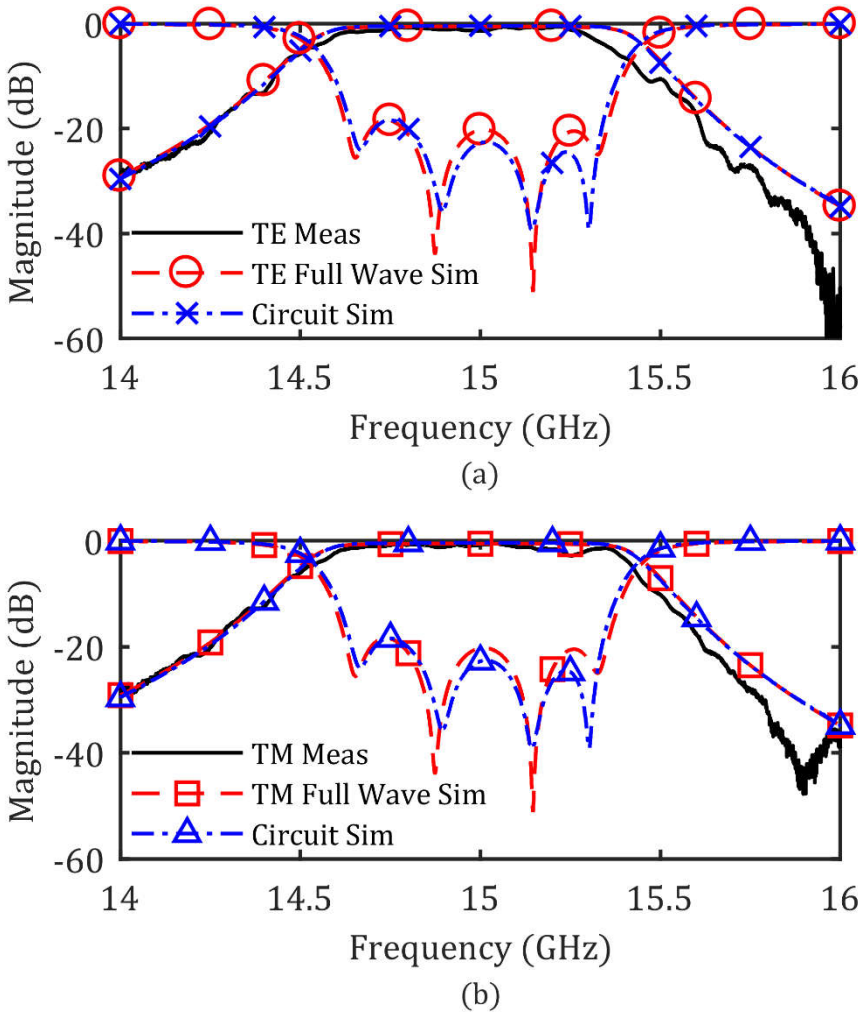

Figure 4.13 Comparison between measured results of the fourth-order prototype with full-wave and circuit simulation for (a) TE polarization. (b) TM polarization.

4.4 **Summary**

A new asymmetrical impedance inverter is proposed that enables the realization of quasi-optical filters with spacers of fixed thickness. A deterministic synthesis procedure for the proposed class of filters is introduced. The proposed technique has the flexibility to adapt to a range of substrate thicknesses. The design methodology is both theoretically and experimentally validated through simulation and measurement. The proposed methodology addresses the limited availability of spacers with custom thickness, hence facilitating the implementation of quasi-optical filters of higher order and at higher frequencies. It is noted that the proposed technique exploits resonators formed as half wavelength cavities and therefore typically results in an increase of overall thickness of the filter structure and consequently, the filter structure is more susceptible to the angle of incidence. However, there are diverse applications that involve QO filters at fixed angle of incidence, for e.g in radiometry and sensing applications, deep space antennas and plasma characterizations. We also note that at higher frequency implementation, for e.g in millimeter wave and THz frequencies, larger substrate thickness can be favorable in manufacturing perspective and significantly in conforming to higher Q-factor. For alternative applications, including more broadband filters, alternative implementation strategies should also be traded-off. Significantly, the proposed impedance inverter also allows to correct by design any small discrepancies in the thickness variation of the spacers. Indeed, this can be accounted in the selection of a different phase to be absorbed in the adjacent resonators, such that the resonant frequency is maintained even for a slightly different thickness of a spacer.

Chapter 5: Design of Quasi-Optical Reflector with Customizable Group Delay

5.1 Introduction

Planar periodic structures are key components in quasi-optical systems due to their advantageous characteristics for multiplexing or de-multiplexing signals. In particular, they offer flexibility to combine or split signals in different domains such as polarization [79], [86], [87] or frequency [9]–[11]. These properties have commonly been employed in radiometry system for imaging [66] and sensing [69] applications. More recently, metallized arrays backed with ground plane have been investigated in [19], [88], [89]. These structures deliver a desired phase shift on the reflection of an incoming wave and have been used as artificial magnetic conductors [77], [90] as low profile surfaces that tailor the radar cross section of physical structures [78], [91] or reflection polarizers [92]–[94]. Realization of such periodic structures comprises various geometries arrangement, which can be implemented using perforation on metal plate [55], [81] or printed conductors on substrates [43], [95].

Aforementioned applications typically do not consider the time domain characteristics of signals and systems. Recently, the capability to control time delays of high frequency signals through components and subsystems is attracting increasing attention. Examples include real-time spectrum analysis [96], [97] and more recent developments in analogue signal processing applications [98]–[100]. The latter exploit periodic structures to control the group delay of signals, which in the narrowband scenario represents the time delay of the amplitude envelopes of the various sinusoidal components of a signal through the device. This approach has also found applications in waveguides to reduce dispersion in antenna feeding systems, [101], dispersive delay structure for the implementation of a compressive receiver in analogue signal processor [98] and resolution improvement in analogue signal processing [100]. These examples rely on a number of synthesis techniques such as distributed impedance analysis [96], coupled resonator theory [102], [103] or metasurfaces [101]. These have been successfully employed for the efficient design of transmission line implementations.

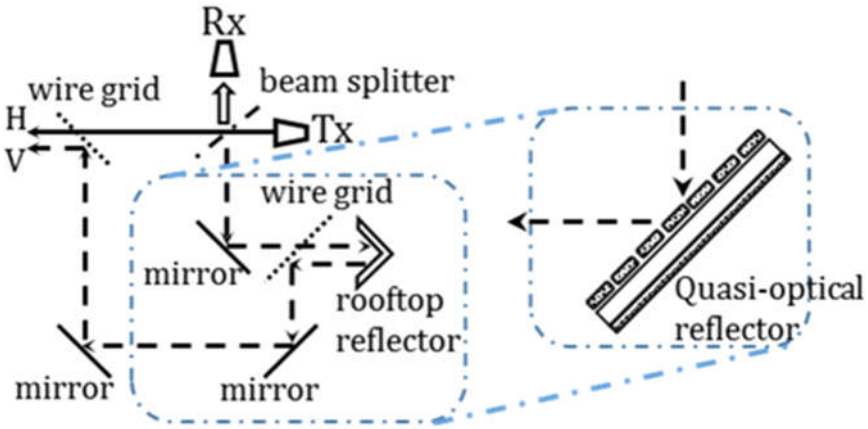

Figure 5.1 Schematic diagram representation of the multiplexing standoff radar system in [41] with proposed replacement using quasi-optical reflector

Aforementioned examples exploit the dispersive characteristics of periodic structures, which enable selective control of the group delay at different frequencies. This is in contrast to the traditional true time delay technique, where longer physical electromagnetic paths are used to adjust the signal delay between two points across the frequency spectrum. True time delay is widely used in antenna beam forming [104]–[106] where it provides advantageous broadband characteristics. More recently, true time delay has also found applications in imaging systems [6], [41], [42] as a means of separating two pulses in the time domain. One disadvantage of true time delay is the requirement for electrically large physical structures, which can be challenging to integrate within compact packages. Instead, periodic structures offer opportunities for more compact integration of the true time delay path.

Motivated by the work in [41], in this chapter the design and implementation of a new class of engineered surfaces is demonstratred that reflect one linear polarization with a significantly higher group delay with respect to its orthogonal, thereby leading to a split of a single incoming pulse into two closely spaced pulses. The operating principle relies on the polarization anisotropy of an engineered periodic reflector that upon reflection exerts a prescribed time delay on one polarization, while the other polarization is virtually unaffected [107]. Selecting the reflection time delay for one component of an incoming linearly polarized pulse, two separate orthogonally polarized pulses will, therefore, be reflected. The implementation in [107] was based exploiting half-wavelength transmission line resonators coupled via single layer doubly periodic arrays, which lead to arbitrary lengths across the structure, thus posing manufacturing challenges as described in chapter 4. Moreover, the design was based on empirical procedures, which can be inefficient for higher time delays. In this chapter, a deterministic framework is

developed for the design of the aforementioned engineered reflectors that are compatible with manufacturing at sub-millimetre waves [83]. Although this application requires a flat group delay along one polarization, it is noted that the proposed approach can be generalized in other dispersive group delay profiles and polarizations.

The rest of the chapter is organised as follows; Section 5.2 provides an overview of the device operation and introduces the synthesis procedures. Subsequently, by means of a design example for a quasi-optical reflector operating at 15 GHz with fractional bandwidth 5% is demonstrated and verified with experimental result in Section 5.3.

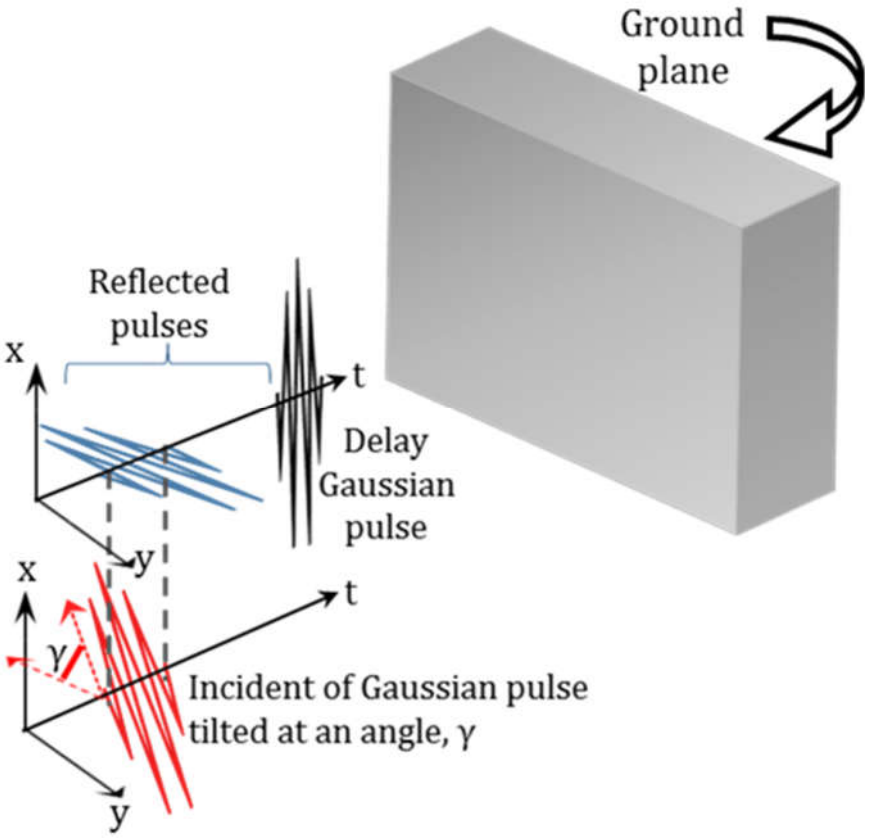

Figure 5.2 Illustration of a reflector surface. An incident of electric field composed of a Gaussian pulse tilted at an angle, γ with respect to y direction. The reflected field decomposes into vertical and horizontal polarization field, where the vertical Gaussian pulse is delay by some amount of time with respect to the incident pulse.

5.2 **Operating Principles and Design Procedures**

The design and implementation of the proposed engineered reflectors is demonstrated by means of an example motivated by the imaging system of [41]. This system involves a time delay in a two beam polarization multiplexing architecture to double the radar frame

rate. This can be achieved by splitting a linear polarized beam into two components with a beam splitter. One of the components propagates through the wire grid unimpeded, while the other component experiences a time delay before recombining with the unimpeded component. This system is illustrated in a simplified diagram in Figure 5.1. Despite the advantages of the proposed architecture in [6], its implementation involves a long optical path for one polarization. In [40] this has been achieved by an assembly of reflectors and true time delay optical paths. The intention here is to demonstrate the capability of substituting the long optical patch with an engineered reflector, as shown in Figure 5.1.

5.2.1 Operating Principles

A schematic representation of the proposed reflector is illustrated in Figure 5.2. The grey block represents the reflector, an anisotropic structure realized with doubly periodic arrays of parallel dipoles backed with a ground plane. Assuming the reflector is illuminated with an incoming plane wave linearly polarized along an angle γ, it can be decomposed into two orthogonal linear polarized components. One component will be polarized in a direction parallel to the dipoles of the arrays and its reflection characteristics, including the associated group delay, will be defined by the interaction with the dipole arrays. The other component will experience minimal delay associated only with the small optical path between the front and the backside of the engineered reflector. If the incoming wave is a pulse, its two constituent components will reflect with a relevant time delay that is practically equal to the group delay imposed by the stack of the dipole arrays. In the subsequent section, the discussion to the reflection properties are limited for the component of the field that is parallel to the dipole arrays.

For this polarization, the reflector can be modelled using the generic one port series coupled-resonator equivalent network shown in Figure 5.3(a). The equivalent network comprises impedance inverters and series resonator across the filter network denoted by $K_{0,1}$ ... $K_{N,N+1}$ and unit element (U.E) respectively. The resonators can be implemented using transmission lines while the inverters can be implemented with the periodic arrays [103]. The short-circuited termination at the end of the network represents the ground plane of the reflector. The impedance inverters control the couplings between successive series resonators as well as between free space and first resonator. By prescribing the

coupling coefficients appropriately between the resonators, the desired group delay upon reflection can be engineered [45].

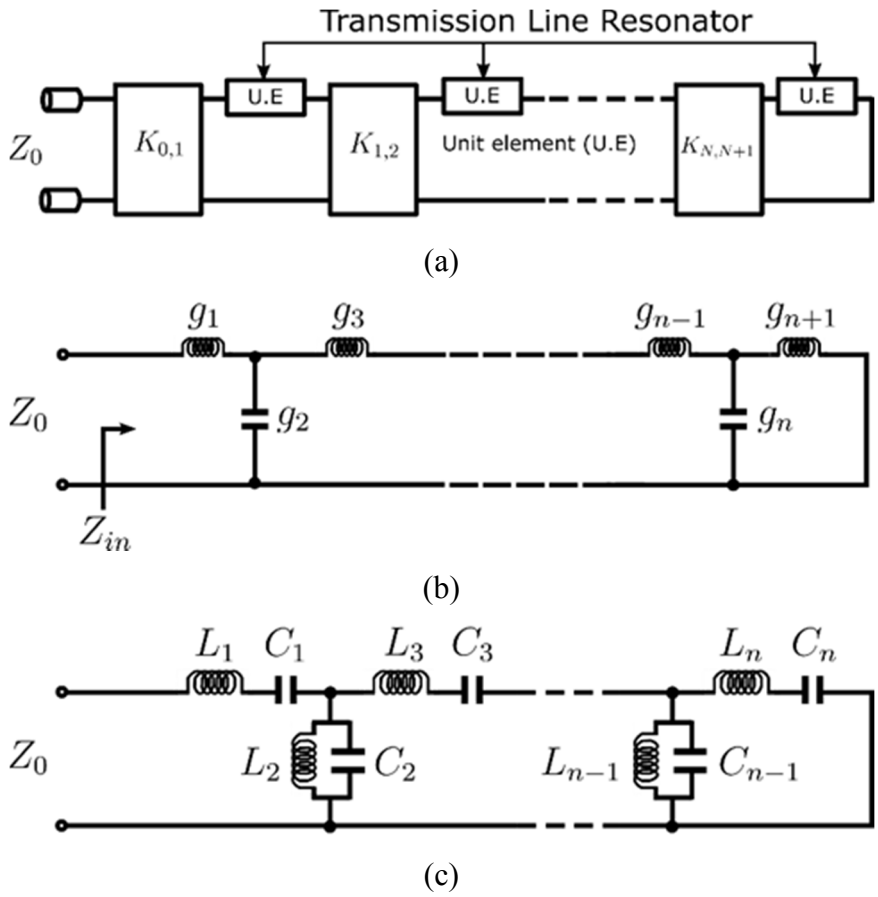

Figure 5.3 (a) Generalized one port series coupled resonator bandpass filter equivalent circuit model. (b) Single port canonical low-pass network (c) Bandpass circuit via frequency transformation of the low-pass network in (b).

5.2.2 Prototype Synthesis Procedure

In order to realize the reflection properties as described in the previous section, techniques originating from filter synthesis [65] can be applied. The design target is to synthesize a network to meet the desired reflection phase characteristic over a defined bandwidth. Ideally, the synthesized network should exhibit linear phase with a predefined gradient to achieve an undistorted and desired delay for reflected output signal when an input signal traverse through the filter network.

In view of the above requirement, the synthesis procedure commences by utilizing the group delay definition, $\tau(\omega)$, which can be expressed as [108]

$$\tau(\omega) = -\frac{d\theta_l}{d\omega} = -\frac{d\theta_l(\Omega)}{d\Omega} \times \frac{d\Omega}{d\omega} \tag{5.1}$$

where, θ_l represents the phase function of the low-pass ladder network in Figure 5.3(b), while Ω and ω represent the low-pass and band-pass angular frequencies respectively [45]. The angular frequency transformation from low-pass to band-pass according to [65]

$$\Omega \leftarrow \frac{\omega_0}{\Delta}\left(\frac{\omega}{\omega_0} - \frac{\omega_0}{\omega}\right) \tag{5.2}$$

is used to obtain the band-pass filter network in Figure 5.3(c) Δ and ω_0 represent the targeted bandwidth and operating frequency of the band-pass filter. Using the frequency transformation definition in equation (5.2), the derivative term $d\Omega/d\omega$ in equation (5.1) can be expressed as

$$\frac{d\Omega}{d\omega} = \frac{1}{\Delta}\left(1 + \frac{\omega_0^2}{\omega^2}\right) \tag{5.3}$$

It is evident that, $d\Omega/d\omega$ is not linear. Therefore it is only possible to assume that $\theta_l(\Omega)$ is linear over a frequency range where $d\Omega/d\omega$ is approximately linear. Therefore, within a narrow bandwidth Δ that centred around the angular frequency ω_0, equation (5.3) can be approximate to [65]

$$\frac{d\Omega}{d\omega} \approx \frac{2}{\Delta\omega_0} \tag{5.4}$$

The operating principle of the reflector calls for a constant group delay $\tau(\omega) = \tau_b$ over a defined Δ and ω_0. Hence, combining (5.1) and (5.4), the phase function of the ladder network in the low-pass domain can be written as

$$\theta_l(\Omega) = -\int_0^{\Omega} \frac{\Delta\omega_0\tau_b}{2} d\Omega = -\frac{\Delta\omega_0\tau_b}{2}\Omega \tag{5.5}$$

Separately, the reflection coefficient for this network can also be expressed in terms of Hurwitz polynomial, $Q(p)$ [103]

$$S_{11}(\Omega) = \frac{Q(-j\Omega)}{Q(j\Omega)} = \exp\left(-j2\theta_Q(\Omega)\right) = \exp(j\theta_l(\Omega)) \tag{5.6}$$

By inspection of equation (5.4), it can be concluded that the phase of the Hurwitz polynomial $\theta_q(\Omega)$ is related to the phase of the ladder network, $\theta_l(\Omega)$ in Figure 5.3(c) according to

$$\theta_Q(\Omega) = -\frac{1}{2}\theta_l(\Omega) = \frac{\Delta\omega_0\tau_b}{4}\Omega \tag{5.7}$$

Significantly, the phase information from (5.5) can be used to define the associated Hurwitz polynomial. According to the framework reported in [109], a specified set of frequency points, $[\Omega_0 \quad \Omega_1 \quad \ldots \quad \Omega_M]$, such that $\{\Omega_0, \Omega_M\} = \{0,1\}$, and the corresponding prescribed phase values $\left[\theta_{Q_0} \quad \theta_{Q_1} \quad \cdots \quad \theta_{Q_N}\right]$ computed from (5.7) enable the formulation of the M[th] order Hurwitz polynomial following the recursive algorithm

$$\begin{aligned} &Q_0(p) = 1, Q_1(p) = p + \beta_0 \\ &Q_M(p) = \beta_{M-1}Q(p) + (p^2 + \Omega_{M-1}^2)Q_{M-2}(p) \end{aligned} \tag{5.8}$$

The coefficients β can be found using recurrence formula

$$\beta_k = \cfrac{\Omega_{k+1}^2 - \Omega_k^2}{\beta_{k-1} - \cfrac{\Omega_{k+1}^2 - \Omega_{k-1}^2}{\beta_{k-2} - \cfrac{\Omega_{k+1}^2 - \Omega_{k-2}^2}{\ddots \\ \beta_0 - \cfrac{\Omega_{k+1}}{\tan\theta_{Q(k+1)}}}}} \quad \Big\} \; k > 0 \tag{5.9}$$

where,

$$\beta_0 = \frac{\Omega_1}{\tan\theta_{Q_1}} \tag{5.10}$$

The Hurwitz polynomials obtained from equation (5.8) are identical to $Q(p)$ of order M in equation (5.4). Generally, the generated Hurwitz polynomial, $Q_M(p)$ can be expressed as

$$Q_M(p) = Q_{M_O}(p) + Q_{M_E}(p) \tag{5.11}$$

where, $Q_{M_O}(p)$ and $Q_{M_E}(p)$ are the odd and even functions which corresponds to the odd and even order terms of $Q_M(p)$, respectively. The normalized input impedance of the ladder network in Figure 5.3(c) can be established by taking the ratio between the odd and even functions of $Q_M(p)$. Subsequently, the low-pass prototype elements (the g values in Figure 5.3(c) are found using a continued fraction technique [110], such that

$$\frac{Q_{M_E}(p)}{Q_{M_O}(p)} = pg_1 + \cfrac{1}{pg_2 + \cfrac{1}{pg_3 + \cfrac{1}{\ddots \\ pg_n + \cfrac{1}{pg_{n+1}}}}} \tag{5.12}$$

Once the coefficients of the low-pass prototype elements have been obtained, the impedance inverter values (K-values in Figure 5.3(a)) can be calculated using generic formulas available in [65], [45]. However, the last inverter $K_{n,n+1}$ has to be modified to involve the reactance slope of the last resonator instead of impedance Z_0 as conventionally seen in generalized two-port coupled resonator circuit model.

$$K_{0,1} = \sqrt{\frac{xZ_0\Delta}{g_0 g_1}}$$

$$K_{i,i+1} = \frac{x\Delta}{\sqrt{g_i g_{i+1}}} \tag{5.13}$$

x = reactance slope parameter of the resonator

The impedance inverters values calculated in the previous step determine the necessary couplings between resonators across the filter network to produce the desired prescribed group delay.

5.2.3 Implementation of Impedance Inverter

There are various impedance inverter networks available in the literature which can be exploited for different filter architecture [45], [65]. A commonly employed impedance

inverter circuit comprises of a shunt reactance terminated symmetrically with identical transmission line at both ends [38], [111]. Thus, the electrical lengths associated with this impedance inverter are then absorbed by the adjacent transmission line resonator. As evident from equation (9), impedance inverters values across the filter structure take distinct values. Consequently, different transmission line resonator will have different electrical length across the filter structure for this impedance inverter implementation. This is also shown in the framework of [103], where all transmission line resonators have different lengths in the waveguide implementation. Although for circuits realized in waveguides or PCBs this does not cause any significant manufacturing challenge, however, customizable spacers for quasi-optical structures pose challenges, particularly in light of low-cost PCB techniques [95].

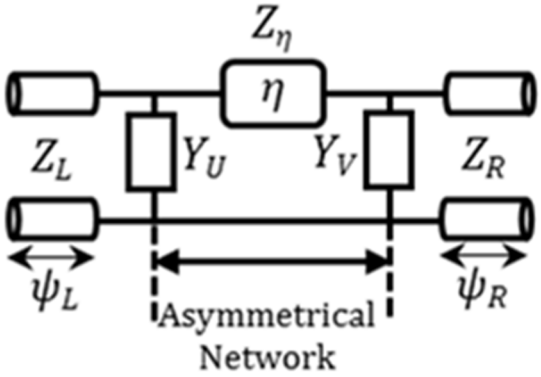

(a)

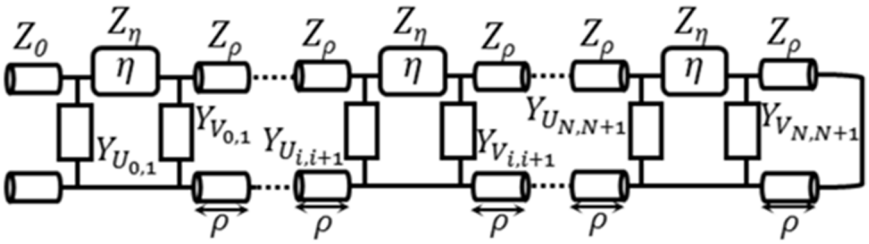

(b)

Figure 5.4 (a) Proposed asymmetrical impedance inverter comprises of a transmission line with electrical length η and susceptance of Y_U and Y_V that can be implemented using either lumped capacitor or inductor. (b) One port reflector network using the proposed asymmetrical impedance inverter, where now all resonators have the same length as all resonators are absorbing a constant phase, δ. Also, note that η is constant for all impedance inverters.

In order to overcome this difficulty, the implementation of asymmetrical impedance inverters followed the framework in chapter 4, as illustrated in Figure 5.4(a). The π-network comprises of a transmission line of fixed electrical length, η placed in between two dissimilar susceptances, Y_U and Y_V, as well as additional transmission lines of electrical lengths ψ_L and ψ_R with characteristic impedance Z_L and Z_R respectively at the two ends. Upon appropriate selection of the suscepance values Y_U and Y_V, it is possible to implement asymmetrical impedance inverters that, when applied to the filter topology in Figure 5.2(a), lead to a prototype where all transmission lines are maintained to a predefined fix length, ρ as illustrated in Figure 5.4(b) [38]. This is next illustrated by means of an example demonstrating the synthesis procedure, including the impedance inverter implementation.

5.3 **Design Examples and Validation of Measurement Results**

5.3.1 Prototype Design

The capability of an engineered reflector to split the two linear polarization components of a Gaussian pulse in the time domain is next illustrated by means of an example involving a Gaussian pulse with half-duration $\sigma = 2$ ns. In an imaging system, such as the one depicted in Figure 5.1, the signal will reflect twice on the reflector, upon transmission and reflection respectively. Consequently in order to distinguish between the vertical and horizontal polarization pulses, the group delay of the component parallel to the dipole arrays should is selected at 4 ns. The required bandwidth of the reflector should be at least $\Delta = 1/\sigma = 500$ MHz [101] such that it contains about 90% of the total power of the Gaussian pulse. Allowing some margin on the bandwidth, a narrow bandpass prototype network is targeted with operating frequency at 15 GHz with 3.5% fractional bandwidth. The desired phase response, $\theta_l(\Omega)$ can then be computed according to equation (5.5). This is plotted in Figure 5.5 and marked as "Prescribed". Subsequently, the filter order is determined by comparing the phase of the generated Mth order Hurwitz polynomial with the prescribed phase for all frequency points, that is to say $\angle Q_M(j\Omega) \approx -\frac{1}{2}\theta_l(\Omega)$. If this condition is not met, the filter order is then incremented and re-examined again. This procedure is repeated until the phase of the Hurwitz polynomial satisfy the prescribed phase requirement.

In order to illustrate the above, the synthesis procedures are begin with the outlined in subsection 5.2.2 utilizing equations (5.7) – (5.10) to generate the Hurwitz polynomial that satisfies the group delay and bandwidth specified above. The phase responses from 1st to 4th order of the Hurwitz polynomials are superimposed with the prescribed phase response in Figure 5.5. It is evident that 4th order is the minimum filter order required to satisfy the time delay and bandwidth specifications. Thus, the generated 4th order Hurwitz polynomial is $Q(p) = p^4 + 2.3110p^3 + 3.0283p^2 + 2.0903p + 0.6350$.

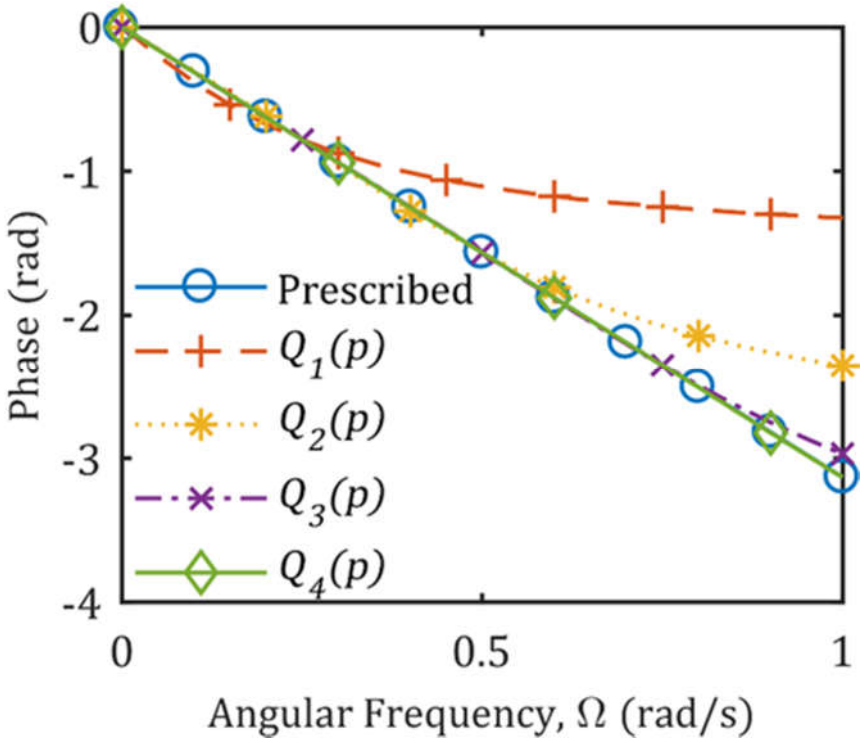

Figure 5.5 Comparison between the prescribed phase and the phases of the first four order of the generated Hurwitz polynomial.

By inspection, the odd and even functions of $Q(p)$ are identified as $Q_{M_O}(p) = 2.3110p^3 + 2.0903p$ and $Q_{M_E}(p) = p^4 + 3.0283p^2 + 0.6350$ respectively. Therefore, taking the ratio of even terms over the odd terms of *Q(p)* leads to the normalized impedance of the ladder network in Figure 5.3(c). Subsequently applying Eq. (12) yields the low-pass prototype (LPP) element values such that $g_1 = 0.4327$, $g_2 = 1.0882$, $g_3 = 1.5178$ and $g_4 = 2.2034$. For validation purposes, these LPP element values are employed in circuit simulation using the setup shown in Figure 5.3(b) to obtain the frequency responses. In particular, the phase and group delay of the LPP is compared with the generated 4th order Hurwitz polynomial, as illustrated in Figure 5.6. The group delay of the LPP network is found by taking the derivative with respect to Ω of equation (5.5)

$$-\frac{d\theta_l(\Omega)}{d\Omega} = \frac{\Delta\omega_0\tau_b}{2} \tag{5.14}$$

As has been stated above, our targeted group delay is 4 ns with 3.5% fractional bandwidth at 15 GHz operating frequency in the bandpass domain. Based on these specifications, the calculated low pass prototype group delay according to equation (5.14), is $-(d\theta_l/d\Omega) = 6.6\ s$. Ideally, this group delay should be constant across the low-pass angular frequency, Ω. However, due to the approximations made, the group delay is expected to exhibit some small variation across the LPP angular frequency. Indeed, as shown in Figure 5.6 the group delay has a deviation of ±0.1 s from 6.6 s across the LPP angular frequency.

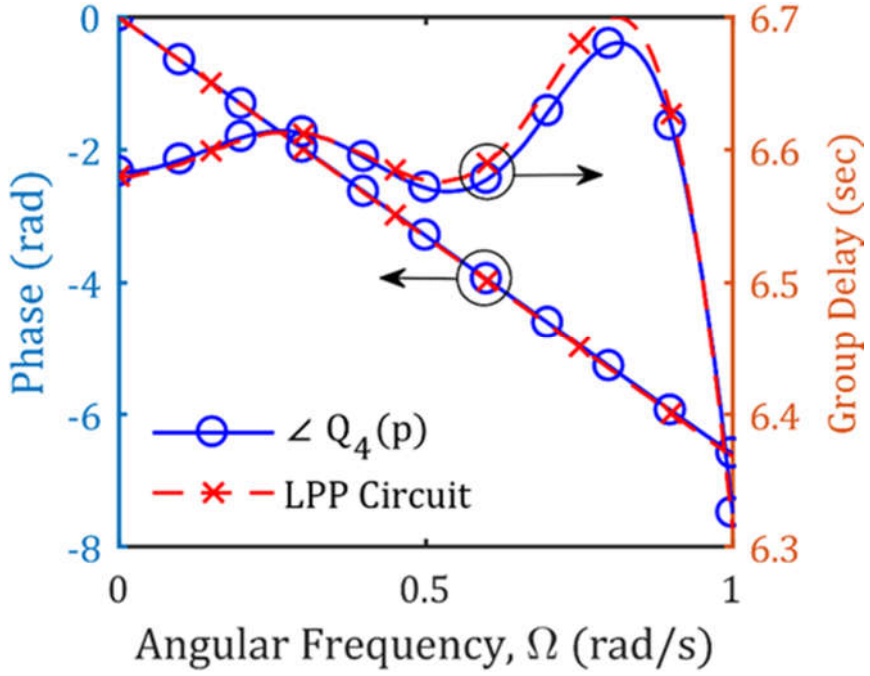

Figure 5.6 Comparison of phase and group delay responses between LPP circuit and prescribed equations.

In what follows, the impedance inverters values can be calculated using equation (13) and subsequently following the theoretical framework in [84], the normalized impedance inverter are found as $\kappa_{0,1} = 0.355$, $\kappa_{1,2} = 0.0801$, $\kappa_{2,3} = 0.0428$ and $\kappa_{3,4} = 0.0301$ respectively. We intend to use the same implementation as demonstrated in chapter 4 such that the electrical length for η and σ corresponds to 40°and 186.19° respectively. For this reason, the presented data from chapter 4, in particular, Figure 4.6 is used to aid the following design. Thus, the following task is to identify the pair of susceptances (Y_U, Y_V) that corresponds to the required κ-values and simultaneously satisfy the condition

imposed by the predefined ρ in Figure 5.4 above. In our case, the selection process begin at κ-value nearest to ground plane. This is because the resonator nearest to the ground plane only absorbs electrical length from the last inverter. To this end, following the procedure developed in in chapter 4, the identified phases (ψ_L, ψ_R) for the calculated κ-values above are found lies within $-10° \leq \psi_L \leq 0°$ and $0° \leq \psi_R \leq 20°$. As a result, the selection of the phases that correspond for all κ-values have been identified and are listed in Table 5.1 below.

Table 5.1 Computed Phases of ψ_U and ψ_V

Index	(0,1)	(1,2)	(2,3)	(3,4)
ψ_L	-8°	-9.24°	-5.29°	-6.71°
ψ_R	15.6°	10.7°	12.9°	6.19°

Subsequently, the data from Table I are utilized to facilitate the search for the relevant susceptances (Y_U, Y_V). To illustrate this, contour plots are presented in Figure 5.7 (extracted from Figure 4.6 in chapter 4) that contain the relevant κ-values and its associated phases (ψ_L, ψ_R) as in Table 5.1. From this plot, the pertinent points are the interception of the three contour lines, which are circled. Therefore, the susceptances (Y_U, Y_V) can be read readily from this plot and their values are tabulated in Table II below.

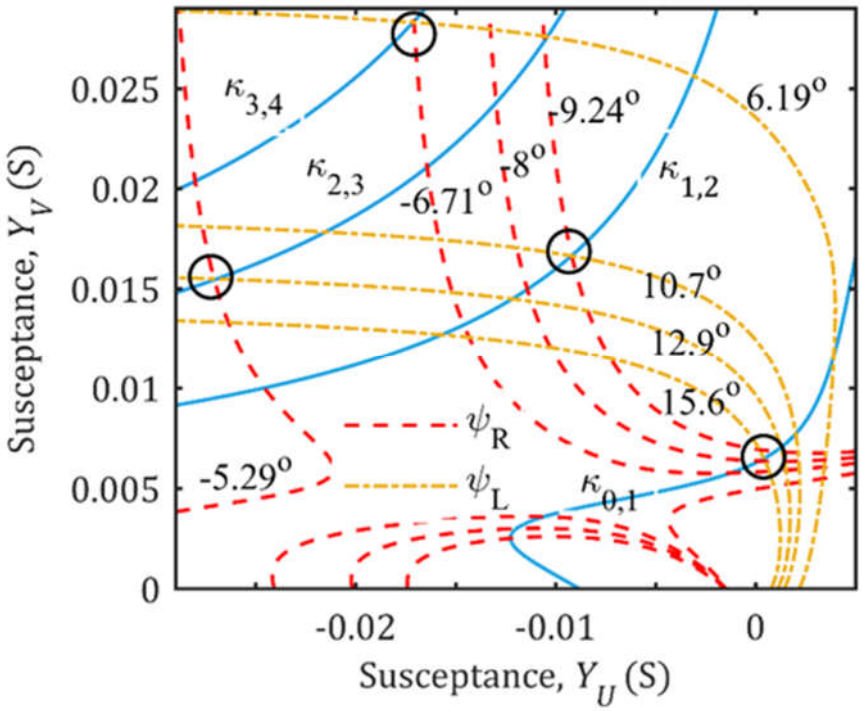

Figure 5.7 Contour lines for specific normalized impedance inverter values and selected phases of ψ_L and ψ_R.

Table 5.2 Susceptance Values For The Asymmetrical Impedance Inverter

Index	(0,1)	(1,2)	(2,3)	(3,4)
Y_U	0.0006	-0.0046	-0.0212	-0.0120
Y_V	0.0039	0.0144	0.0137	0.0278

The determined susceptances (Y_U, Y_V) can be easily translated to equivalent capacitances and inductances for the asymmetrical π-network. The phase and group delay responses for both the L-C and distributed elements bandpass network that corresponds to Figure 5.3(c) and Figure 5.4(b), respectively, are depicted in Figure 5.8. As shown, the two responses are in excellent agreement and provide the specified group delay value of 4 ns.

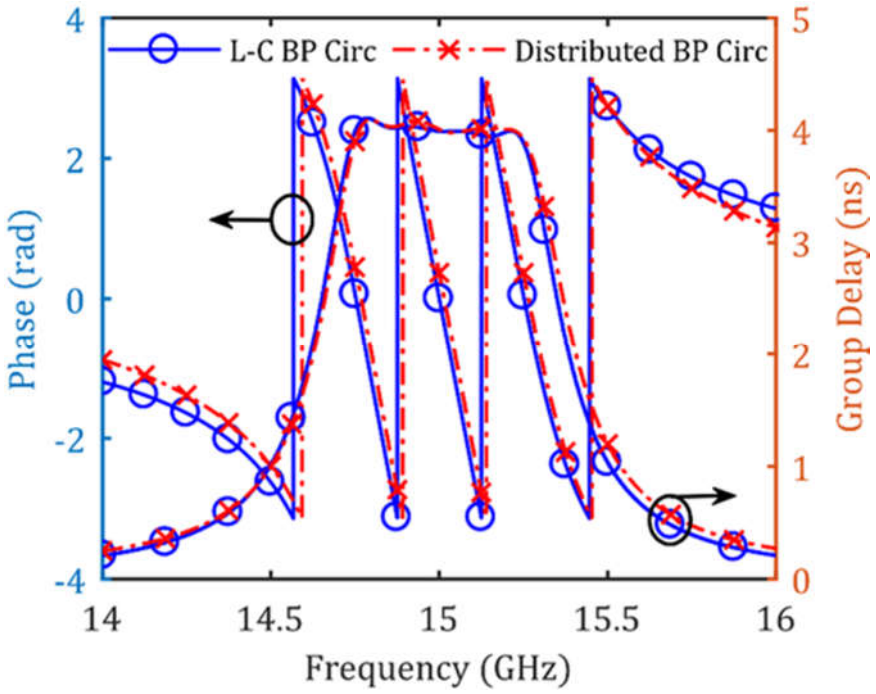

Figure 5.8 Comparison between phase and group delay responses between L-C and distributed bandpass (BP) circuit simulation.

5.3.2 Prototype Implementation

Once, the normalized impedance inverters are determined, the implementation of these inverters followed the proposed asymmetrical network discussed in chapter 4. With reference to the implementation in chapter 4, 31-HF Rohacell Foam with dielectric constant, ε_r = 1.07 and thickness, h = 10 mm is considered for the spacers that implement as resonators. It is noted that at this operating frequency, the electrical length of this dielectric spacer conforms to 186.19°. Laminates from Taconic TLY-5 with a dielectric

constant ε_r = 2.2 and thickness, l = 1.5 mm are exploited to support periodic arrays to realize the asymmetrical impedance inverter.

Next step in the design procedure is to map the desired susceptances obtained above to physical geometry of two-dimensional periodic array for quasi-optical realization. The array can be etched on a doubly metalized laminate using conventional PCB processes. Moreover, the geometrical choice for the arrays are the simple grid inductor and capacitor. This is depicted in Figure 5.9 for array unit cells with the same periodicity. The orientation of the conductor enables the array to behave like inductor and capacitor respectively for a vertically polarized plane wave, while it is transparent for a horizontally polarized plane wave.

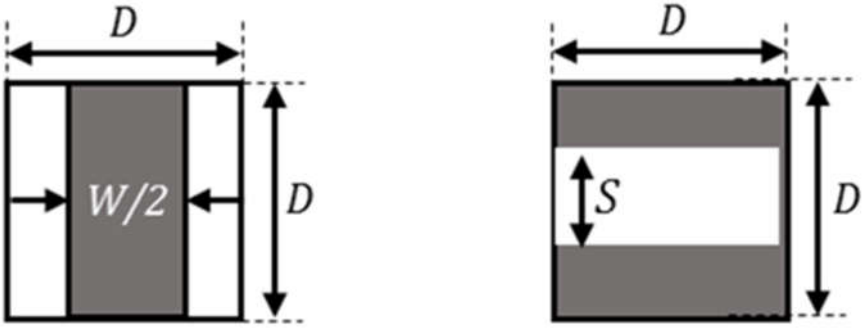

Figure 5.9 (a) FSS unit cell for inductive grids. (b) FSS unit cell capacitive grids.

The dimension of the capacitive and inductive arrays can be initially estimated using closed-form expressions that are available in literature [48]

$$C_{i,i+1} = \varepsilon_0 \varepsilon_{i,i+1} \frac{2D}{\pi} \ln\left(\csc\left[\frac{\pi S_{i,i+1}}{2D}\right]\right) \tag{5.15}$$

$$L_{i,i+1} = \mu_0 \mu_{i,i+1} \frac{D}{2\pi} \ln\left(\csc\left[\frac{\pi W_{i,i+1}}{2D}\right]\right) \tag{5.16}$$

The exact geometrical dimensions for the capacitive and inductive arrays are obtained with optimization using full-wave electromagnetic simulation to match the frequency response of the equivalent asymmetrical π-network in Figure 5.4(a). The optimized circuit values and final geometrical dimensions for the array are tabulated in Table 5.3.

Standard PCB lithography was employed to photo-etch the arrays on the aforementioned laminate. The arrays and the foam spacers are then secured together with adhesive spray from 3M (Repositionable 75). The adhesive spray has a negligible impact on the electrical

length of the transmission lines. The cross-sectional view of the reflector is shown in Figure 5.10.

Table 5.3 Circuits Parameters and Geometrical Dimensions for Fourth-Order Reflector

Circuit Parameters				
$C_{U0,1}$ (pF)	$C_{V0,1}$ (pF)	$L_{U1,2}$ (nH)	$C_{V1,2}$ (pF)	$L_{U2,3}$ (nH)
0.0061	0.0426	2.00	0.1516	0.4975
$C_{V2,3}$ (pF)	$L_{U3,4}$ (nH)	$C_{V3,4}$ (pF)		
0.1456	0.8687	0.3012		
Geometrical Dimensions (mm)				
$S_{U0,1}$	$S_{V0,1}$	$W_{U1,2}$	$S_{V1,2}$	$W_{U2,3}$
4.95	2.70	1.50	0.79	4.05
$S_{V2,3}$	$W_{U3,4}$	$S_{V3,4}$		
0.95	3.17	0.15		
D	l	h		
7.8	1.5	10		

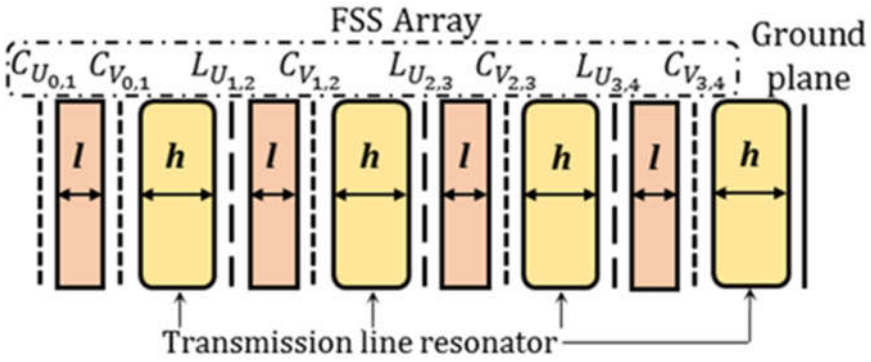

Figure 5.10 Side view of the fourth order bandpass FSS filter depicting relative position of the FSS array, substrate and spacer resonator.

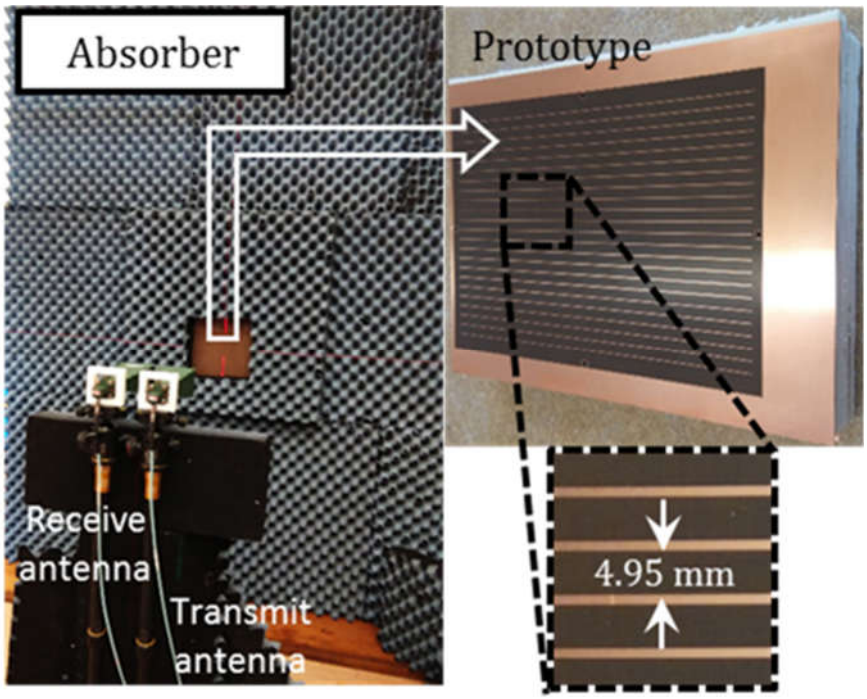

(a) (b)

Figure 5.11 (a) Measurement setup (b) Photograph of the fabricated fourth-order reflector prototype. Inset: zoomed area of the first-layer.

The frequency response of the prototype is verified using free-space measurement based on the procedures outlined in [36], [112]. The measurement setup involved two horn antennas placed on the same plane to characterize the reflection coefficient of the prototype, which is located at an opening of an absorber, as shown in Figure 5.11(a). A photograph of the fabricated prototype is also shown in Figure 5.11(b). The reflection from the group delay reflector is measured and calibrated against an identical measurement from a fully metalized reflector. The measured results are time-gated to reduce the effect of multiple reflections between the two antennas.

The measured magnitude and phase of the reflection coefficient are depicted in Figure 5.12(a) and 5.12(b). For comparison, the results from the full-wave simulation as well as the equivalent circuit are superimposed. From these results, the group delay can be extracted according to equation (5.1) and is plotted in Figure 5.12(c). Good agreement is observed between measured results and simulation despite some discrepancies, which are attributed to manufacturing tolerances and measurement inaccuracies.

In order to demonstrate the practical time-domain results, Figure 5.13 plots the two polarization components of a modulated Gaussian pulse with a carrier frequency at 15 GHz and half-duration $\sigma = 2$ ns when reflected twice by the prototype. The polarization of the incoming wave is linear and approximately at an angle, $\gamma = 75°$. This compensates

for the additional loss experienced by the component parallel to the grid array. As shown, the reflected output is delayed by approximately 7 ns.

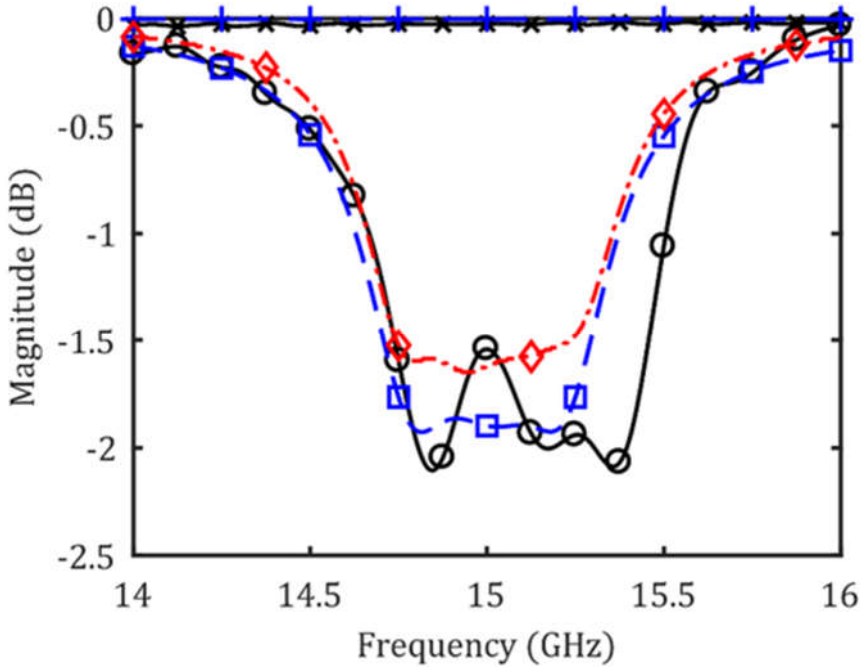

(a)

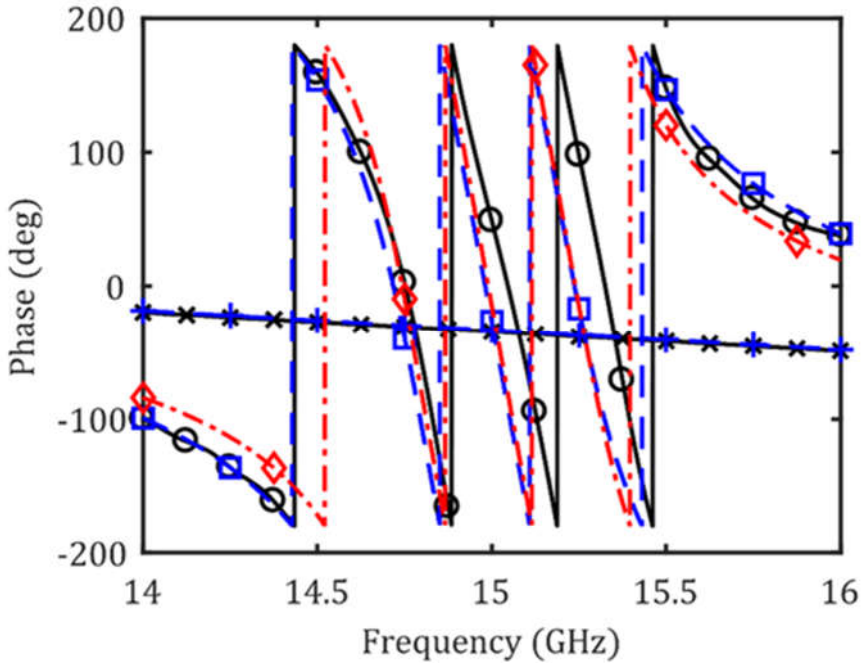

(b)

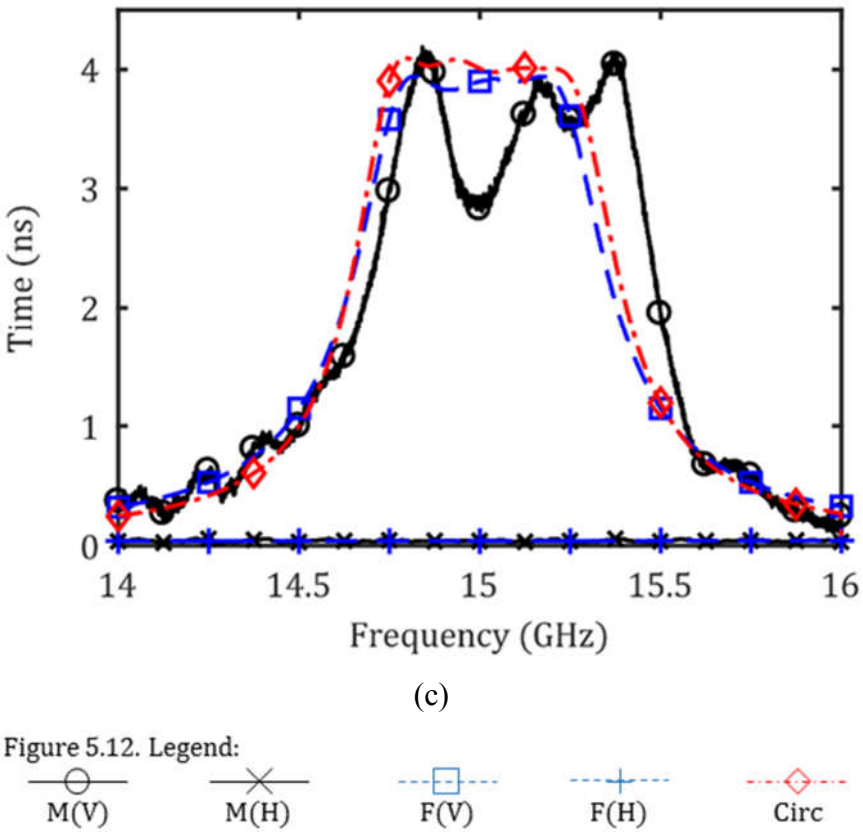

Figure 5.12 Comparison between measured (M) results of the fourth-order reflector prototype with full-wave (F) and circuit simulation (Circ) for both Vertical (V) and Horizontal (H) polarization. (a) Magnitude (b) Phases (degree) (c) Group delay.

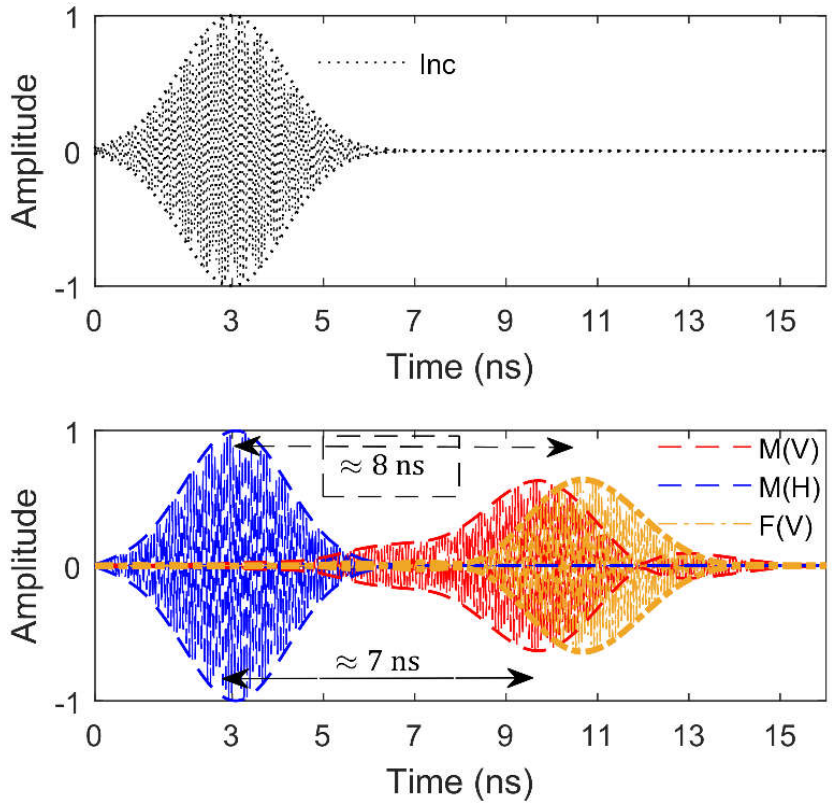

Figure 5.13 Time domain representation of the reflected output measured (M) results and full-wave (F) for both Vertical (V) and Horizontal (H) polarization of the fourth-order reflector prototype for an Incident (Inc) Gaussian pulse.

5.4 **Summary**

Exploiting anisotropy, a quasi-optical reflector is demonstrated that is capable of splitting a linear polarized plane wave pulse into two pulses closely placed in the time domain. A deterministic synthesis procedure has been proposed that facilitate the design to customize a delay for a particular polarization with respect to the other polarization. Furthermore, the proposed technique also leads to the practical design of a quasi-optical reflector with all transmission lines conform to pre-selected fix length. A design example based on the proposed method has been presented with good agreement between the numerical and experimental results. The technique employed for the design of the reflector can be extended to other implementation of dispersion engineering quasi-optical components, which can be particularly suitable for the higher region of the electromagnetic spectrum.

Chapter 6: **Conclusion**

The work presented in this thesis involve design and synthesis techniques for multilayer quasi-optical filter exploiting grid array. The final chapter of this thesis provides a summary of achievements based on the research objectives and recommendation for future work.

6.1 **Conclusion and Summary of Results**

From an overview, this thesis has achieved contribution in two main areas. The first area being, the development of a design method for quasi-optical filters with transmission lines of predefined fixed length based on the filter operating frequency, bandwidth and response type. A prototype of the quasi optical filter and reflector was also done using low-cost standard PCB fabrication techniques.

The methodology entails a proposed implementation on direct coupled cavity filter topology with an asymmetrical π-network for impedance inverter. The asymmetrical π-network comprises a transmission line that is sandwiched between two dissimilar susceptances. As demonstrated in chapter 4, with appropriate selection of the susceptances allow all resonators across the filter structure to have a predefined fix length. The determined susceptances of the asymmetrical inverters are then primarily mapped to geometrical dimensions for the periodic array. Subsequently, the periodic arrays dimensions of the inverter layers are then optimized using full-wave simulations to match the frequency response with its equivalent circuit. Following this the inverters are developed and prototyped by etching on both sides of identical laminates, while the cavities resonators are represented by identical spacer of fix length. The quasi-optical filter is formed by stacking the inverter layers and spacers accordingly. The experimental equipment require for the measurement are a rectangular flat panel, two Ku band horn antennas and vector network analyser with the capability to measure up to at least 20 GHz. The flat panel dimensions are approximately 1 m×1m. The panel is padded with absorbers with an opening at the centre of the panel, where the prototype is installed. The panel is placed in between two horn antenna located at a distance about 80 cm each side with line of sight passed through the centre of the panel.

The research output from this effort results in a developed synthesis procedure to address the limited availability of spacer with custom thickness. As demonstrated in section 4.3, the implementation of the asymmetrical π-network resulted in an overall filter structure to have all transmission line with predefined fixed length. The design technique has been verified theoretically and experimentally with full wave simulations and free space measurement respectively. Both simulation and measurement results corroborate well.

The second area of this research shows the design of quasi-otical reflector capable of producing group delay difference for the two orthogonal linear polarisation. Similarly, performance measurements were conducted on the quasi-optical filter using free-space measurement technique. The experimental equipment requirements are similar to the setup for quasi-optical filter measurement as mentioned above, however with the exception the transmit and received horn antennas are placed on the same plane. In this research work, a transfer function is developed based on a prescribed group delay. The low pass prototype (LPP) element values are then extracted from the transfer function using continued fraction technique. Subsequently, the LPP elements are used to compute the normalized impedance inverter values. The calculated normalized impedance inverter values signify the required coupling between the resonators to provide the desired group delay. Practical realization of the quasi-optical reflector is based on the implementation of the asymmetrical π-network for impedance inverter and half-wavelength cavities as resonator. The experimental equipment require for the measurement are a rectangular flat panel, two Ku band horn antennas and vector network analyser with the capability to measure up to at least 20 GHz. The flat panel dimensions are approximately 1 m×1m. The panel is padded with absorbers with an opening at the centre of the panel, where the prototype is installed. The panel is placed in between two horn antenna located at a distance about 80 cm each side with line of sight passed through the centre of the panel.

The research output from this work results in a deterministic design procedure for a flat reflector that is capable to separate signal in time domain for an incoming of slant 45° polarized pulse into two perpendicular pulses, namely the vertical and horizontal polarization. As shown in subsection 5.3.2, for an incident modulated Gaussian pulse, the reflected vertical polarization is delayed following the prescribed group delay, while the horizontal pulse is unaffected. In addition, the proposed design procedure has led to practical design quasi-optical reflector with all transmission lines conform to pre-selected

fix length. The measured results are in good agreement with full wave and circuit simulations. Overall, the research goals and objectives in this research are fulfilled.

6.2 **Future Work**

Infrared filters are commonly employed in astronomical instruments such as the telescope. Such devices require out-of-band radiation rejection prior to the signal arrival at the detector. This allows noise reduction and increased detection sensitivity. In recent years, the long mid-infrared (MMIR) frequency range has garnered attention due to its ability to allow for observation of highly reddened sources as well as a wide range of molecular and atomic features. The development of filters in this frequency band, however, has been hindered due to several practical issues such as the need for high accuracy fabrication techniques in dielectric interference filters, and reliability issues in air-gap metal mesh filters. A possible solution to this is to employ the concept of resonator coupled spatial filters as described in Chapter 4. The structural rigidity for a self-standing design coupled with a simple and low cost fabrication techniques are attractive features for a filter in space/astronomy applications.

Alternatively, an application as described in Chapter 5 for a reflecting-type spatial filter could be designed for the same purpose. Inspired by monochromators in optics, the general operating mechanism of this device reflects a selected wavelength narrowband of the incident wave to another chosen direction from a wider range of wavelength in the incident waveform.

Another potential niche area to extend this research is to expand on the design of aberration free lenses at optical wavelengths where chromatic aberration is undesirable and present in most lenses operating at optical wavelengths. Overcoming chromatic aberrations is necessary in imaging systems as applied in conventional microscopy, photography, to sophisticated astronomy spectroscopy, and coherence tomography.

Appendix A: Electromagnetics Theory for Periodic Surfaces

In this appendix, basic formulation of electromagnetic wave equations as applied in homogeneous source is presented. Since the majority of the contents of this appendix can be found in a variety of textbooks, many things will be presented briefly, with emphasis only in the points of interest for the formulation of electromagnetic modelling presented in chapter 3. The first subsection A1 gives a brief account of the electromagnetic theory and in particular electromagnetic waves. Subsection A2 briefly introduced the definition of Floquet's theorem and space harmonics for one dimensional case. The following subsection A3 presents the analysis of modal solution for wave propagating in two dimensional planar periodic array following the Floquet's theorem in previous subsection. Lastly, in subsection A4 demonstrate the general formulation of vector Floquet expansion for electric and magnetic fields based on the modal solution obtained in subsection A3.

A1: Overview on Maxwell's Equations and Wave Equation

The basis of all electromagnetic modelling stems from Maxwell equations. The Maxwell's equations consists of four equations relating electric field, $\vec{E}$ and magnetic field $\vec{H}$ as given below [47], [64], [113]:

$$\nabla \times \vec{E} = -\mu \frac{\partial \vec{H}}{\partial t} \tag{A.1}$$

$$\nabla \times \vec{H} = \epsilon \frac{\partial \vec{E}}{\partial t} + \vec{J} \tag{A.2}$$

$$\nabla \cdot \vec{E} = \frac{\rho}{\epsilon} \tag{A.3}$$

$$\nabla \cdot \vec{H} = 0 \tag{A.4}$$

The constants ϵ and μ are associated with the wave propagation through a medium, where

$$\epsilon = \epsilon_r \epsilon_0 \tag{A.5}$$

$$\mu = \mu_r \mu_0 \tag{A.6}$$

The relative permittivity and permeability of a medium are denoted as ε_r and μ_r respectively. While, ϵ_0 and μ_0 are referred as the universal constant permittivity and permeability of free space. Commonly, the steady state solution for the fields of sinusoidal time dependence are considered for most cases. As a result, all vector fields can be represented as complex phasor space vectors [47], [64], [113], which is independent of time. For example, the mathematical representation for time harmonic electric field, $E(x, y, z, t)$ can be expressed as $E(x, y, z)\exp(j\omega t)$. Then by definition

$$\vec{E}(x, y, z, t) = \mathrm{Re}\left[\vec{E}(x, y, z)\exp(j\omega t)\right] \tag{A.7}$$

Applying phasor representation, the time derivative $\frac{\partial}{\partial t}$ is replaced by the factor $j\omega$, since $\frac{\partial}{\partial t}[\exp(j\omega t)] = j\omega\exp(j\omega t)$. The time derivative may then be eliminated by denoting the time dependence $\exp(j\omega t)$ for all quantities. Hence Maxwell's equations with steady state sinusoidal time dependence reduces to [47], [64], [113]

$$\nabla \times \vec{E} = -j\omega\mu\vec{H} \tag{A.8}$$

$$\nabla \times \vec{H} = j\omega\epsilon\vec{E} + \vec{J} \tag{A.9}$$

$$\nabla \cdot \vec{E} = \frac{\rho}{\epsilon} \tag{A.10}$$

$$\nabla \cdot \vec{H} = 0 \tag{A.11}$$

The curl of the Maxwell's phasor representation in equations (A.8) – (A.9) are referred as the coupled equations that comprises the unknown electric field $\vec{E}$ and magnetic field $\vec{H}$, which to be determined. These equations can be uncoupled and leads to wave equation that can be solved for the unknowns electric and magnetic fields [47]. Details derivation of the wave equation have been addressed in many general literatures on electromagnetics and therefore will not be covered in this subsection. In what follows, for an electromagnetic field propagates through a general lossy medium with finite conductivity, σ, the vector wave equation has a form [47], [64], [113]

$$\nabla^2\vec{F}(x, y, z) - \Upsilon^2\vec{F}(x, y, z) = 0 \tag{A.12}$$

The complex propagation constant, $\Upsilon = j\omega\sqrt{\epsilon\mu}\sqrt{1 - j\frac{\sigma}{\omega\epsilon}}$ represent the wavenumber of the medium, while vector $\vec{F}$ can represent either the electric field $\vec{E}$ or magnetic field $\vec{H}$ [47]. For a wave propagate in a source-free, linear, isotropic, homogeneous and lossless medium, then this implies $\sigma = 0$, and equation (A.12) can be rewritten as [47], [64], [113]

$$\nabla^2\vec{F}(x,y,z) + k^2\vec{F}(x,y,z) = 0 \tag{A.13}$$

where, $k = \omega\sqrt{\epsilon\mu} = \frac{2\pi}{\lambda}$ is defined as the real wavenumber of the medium. The vector wave equation in (3.13) holds for each rectangular component of $\vec{F}$ [47], [64], [113]

$$\frac{\partial^2 F_i(x,y,z)}{\partial x^2} + \frac{\partial^2 F_i(x,y,z)}{\partial y^2} + \frac{\partial^2 F_i(x,y,z)}{\partial z^2} + k^2 F_i(x,y,z) = 0 \tag{A.14}$$

where, the index i symbolized the rectangular component of *x*, *y* or *z*. Subsequently, the scalar wave equation in (A.14) is usually solved by separation of variables technique to obtain the electric and magnetic fields.

A2: Floquet's Theorem and Space Harmonics

The fundamental analysis of periodic structures is based on Floquet theorem. This theorem states that for a periodic structure capable of supporting propagating wave, the wave repeats at every terminal plane except for a propagation factor of $\mathrm{e}^{-\gamma d}$, where *d* is the defined length of a unit cell. Consider a one dimensional problem, where the field at unit cell located on the plane between $0 \leq z \leq d$ is $\vec{\varrho}(x,y,z)$. Thus, the field in adjacent unit cell located between $d \leq z \leq 2d$ should be $\mathrm{e}^{-\gamma d}\vec{\varrho}(x,y,z)$ [64].

This implies the field solution in a periodic structure can be expressed as

$$\vec{\varrho}(x,y,z) = \mathrm{e}^{-\gamma z}\vec{\varrho}_p(x,y,z) \tag{A.15}$$

The function ϱ_p is a periodic function of *z* with period *d*, therefore

$$\vec{\varrho}_p(x,y,z+nd) = \vec{\varrho}_p(x,y,z) \tag{A.16}$$

Since $\vec{\varrho}_p(x,y,z)$ is periodic, it is possible to expand it into an infinite complex Fourier series

$$\vec{\varrho}_p(x,y,z) = \sum_{n=-\infty}^{n=\infty} \vec{\varrho}_n(x,y)\mathrm{e}^{-j\frac{2n\pi z}{d}} \tag{A.17}$$

Where $\varrho_n(x,y)$ represent a vector function with spatial *x* and *y* dependency. If the wave propagate through a lossless medium, this implies $\gamma = j\beta$, equation (A.17) can be rewritten as

$$\varrho(x,y,z) = \sum_{n=-\infty}^{n=\infty} \varrho_n(x,y)\mathrm{e}^{-j\left(\beta+\frac{2n\pi}{d}\right)z} = \sum_{n=-\infty}^{n=\infty} \varrho_n(x,y)\mathrm{e}^{-j\beta_n z} \tag{A.18}$$

Each term in this expansion of (A.18) represent the Floquet Space Harmonics and has a unique wavenumber in the direction of *z* [64]

$$\beta_n = \beta + \frac{2n\pi}{d} \tag{A.19}$$

A3: Modal Field Solution for Two Dimensional Periodic Array

Consider a two-dimensional free standing single periodic array lying on *z = 0* plane as depicted in Figure A.1. The surface is assume to be lossless and has periodicities in the direction of *x* and *y* axes, with period d_x and d_y respectively.

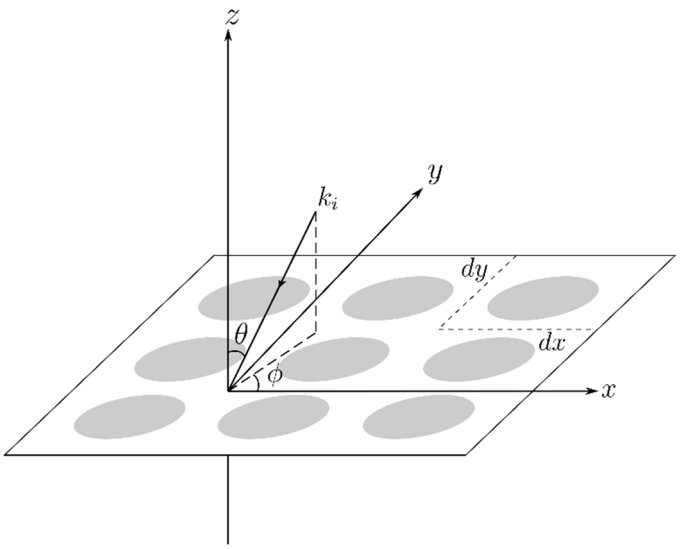

Figure A.1: Arbitrary periodic array between two distinct media

The computation of the scattered fields from this structure begin with solving scalar wave equation (A.14) for periodic boundary condition that is defined for a unit cell.

$$\left(\frac{\partial^2}{\partial x^2}+\frac{\partial^2}{\partial y^2}+\frac{\partial^2}{\partial z^2}+k^2\right)\psi(x,y,z)=0 \tag{A.20}$$

Assuming the wave is travelling in the positive *z* axis direction, the modal field expression $\psi(x,y,z)$ can be written as [47]

$$\psi(x,y,z)=\psi(x,y)\mathrm{e}^{-j\beta z} \tag{A.21}$$

Substituting equation (A.21) into equation (A.20) yields the Helmholtz partial differential equation that can be solved with conventional variable separable methods. Specifically, the scalar potential $\psi(x,y)$ can be rewritten in the form of two product function of $g(x)$ and $h(y)$, i.e. $\varphi(x,y)=g(x)h(y)$. Since $\varphi(x,y)$ is periodic, therefore, $g(x)$ and $h(y)$ should be also be periodic. Hence, the function $g(x)$ and $h(y)$ can be expressed as complex Fourier series, which has a form [58]

$$g(x)=\sum_{n=-\infty}^{n=\infty}a_n\mathrm{e}^{-jk_{x_n}x} \tag{A.22}$$

$$h(y)=\sum_{m=-\infty}^{m=\infty}a_m\mathrm{e}^{-jk_{y_m}x} \tag{A.23}$$

where,

$$k_{x_n}=k_{x_i}+\frac{2\pi n}{d_x}=\sqrt{\epsilon_{r1}}\frac{2\pi}{\lambda}\sin\theta\cos\phi+\frac{2\pi n}{d_x} \tag{A.24a}$$

$$k_{y_m}=k_{y_i}+\frac{2\pi m}{d_y}=\sqrt{\epsilon_{r1}}\frac{2\pi}{\lambda}\sin\theta\sin\phi+\frac{2\pi m}{d_y} \tag{A.24b}$$

The wavenumbers k_{x_n} and k_{y_m} represent the phase shift along *x* and *y* direction respectively. While, the constant k_{x_i} and k_{y_i} present in the above expression are associated with the incident wavenumber directed along *x* and *y* axis respectively. Thus, the modal field solution in equation (A.21) can be written as [58]

$$\psi(x,y,z)=\mathrm{e}^{-j\left(xk_{x_n}+yk_{y_m}+z\beta_{nm}\right)} \tag{A.25}$$

where,

$$\beta_{nm} = \sqrt{k^2 - k_{x_i}^2 - k_{y_i}^2} \tag{A.26}$$

Similar to the one dimensional case reviewed in subsection A2, any component of electric or magnetic field can be expressed in the form of Fourier series [58]

$$F(x,y,z) = \sum_{n=-\infty}^{n=\infty} \sum_{m=-\infty}^{m=\infty} a_{nm}\varphi(x,y,z) = \sum_{nm} a_{nm} \mathrm{e}^{-j\left(xk_{x_n} + yk_{y_m} + z\beta_{nm}\right)} \tag{A.27}$$

where, a_{nm} is the modal amplitude.

A4: Floquet Expansion for Two Dimensional Periodic Array

Array shown in Figure A.2 have periodical arrangement along an arbitrary lattice vector of $\vec{d}_p$ and $\vec{d}_q$ with unit vector direction $\hat{p}$ and $\hat{q}$ respectively. The angle between the two lattice vectors $\vec{d}_p$ and $\vec{d}_q$ is α and $\vec{d}_p$ make an angle α_1 with respect to *x*-axis. The relation of lattice vectors $\vec{d}_p$ and $\vec{d}_q$ with $\hat{x}$ and $\hat{y}$ unit vectors can be acquire as [58]

$$\vec{d}_p = \left|\vec{d}_p\right|(\cos\alpha_1\hat{x} + \sin\alpha_1\hat{y}) \tag{A.28a}$$

$$\vec{d}_q = \left|\vec{d}_q\right|(\cos\alpha_2\hat{x} + \sin\alpha_2\hat{y}) \tag{A.28b}$$

where, $\alpha_2 = \alpha_1 + \alpha$.

The projection (p,q) onto (x,y) [58]

$$\begin{pmatrix} p \\ q \end{pmatrix} = \frac{1}{\sin\alpha} \begin{pmatrix} \sin\alpha_2 & -\cos\alpha_2 \\ -\sin\alpha_1 & \cos\alpha_1 \end{pmatrix} \begin{pmatrix} x \\ y \end{pmatrix} \tag{A.29}$$

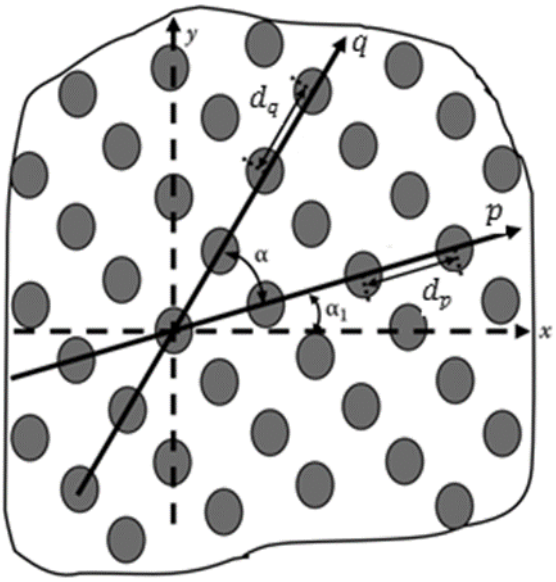

Figure A.2: Periodic array of arbitrary lattice arrangement

The modal solution from equation (A.25) can be rewritten as [58]

$$\psi(x,y,z) = \mathrm{e}^{-jk_p p} \cdot \mathrm{e}^{-jk_q q} \cdot \mathrm{e}^{-j\vec{k}_{t00}\cdot\vec{r}}\mathrm{e}^{-j\beta_{nm}} \tag{A.30}$$

where,

$$\vec{k}_{t00} = \sqrt{\epsilon_{r1}}\frac{2\pi}{\lambda}(\hat{x}\sin\theta\cos\phi + \hat{y}\sin\theta\sin\phi) \tag{A.31a}$$

$$k_\chi = \frac{2\pi\chi}{d_\chi} \qquad \text{, where } \chi = p \text{ or } q \tag{A.31b}$$

$$\vec{r} = x\hat{x} + y\hat{y} \tag{A.31c}$$

Utilizing the transformation matrix of equation (A.29) for the modal solution in (A.30), yields [58]

$$\psi(x,y,z) = \mathrm{e}^{-j(\vec{k}_{t_{nm}}\cdot\vec{r})}\mathrm{e}^{-j\beta_{nm}} = \psi_{nm}(x,y)\mathrm{e}^{-j\beta_{nm}} \tag{A.32}$$

where

$$\vec{k}_{t_{nm}} = \vec{k}_{t_{00}} + n\vec{k}_1 + m\vec{k}_2 \tag{A.33}$$

The phase displacement $\vec{k}_1$ and $\vec{k}_2$ along the lattice directions in Cartesian vector bases are [58]

$$\vec{k}_1 = -\frac{2\pi}{A}\hat{z} \times \vec{d}_q = \left|\vec{d}_q\right|(\hat{x}\sin\alpha_2 - \hat{y}\cos\alpha_2) \tag{A.34a}$$

$$\vec{k}_2 = \frac{2\pi}{A}\hat{z} \times \vec{d}_p = \left|\vec{d}_p\right|(-\hat{x}\sin\alpha_1 + \hat{y}\cos\alpha_1) \tag{A.34b}$$

With reference to equations (A.31a) and (A.34), equation (A.33) can be explicitly rewritten as [58]

$$\begin{aligned}\vec{k}_{t_{nm}} &= \hat{x}\left(\sqrt{\epsilon_{r1}}\frac{2\pi}{\lambda}\sin\theta\cos\phi + \left|\vec{d}_q\right|\sin\alpha_2 - \left|\vec{d}_p\right|\sin\alpha_1\right) \\ &\quad + \hat{y}\left(\sqrt{\epsilon_{r1}}\frac{2\pi}{\lambda}\sin\theta\sin\phi - \left|\vec{d}_q\right|\cos\alpha_2 + \left|\vec{d}_p\right|\cos\alpha_1\right) \\ &= \hat{x}k_{tx} + \hat{y}k_{ty}\end{aligned} \tag{A.35}$$

The notation ψ_{nm} in (A.32) is defined as Floquet phasor. The Floquet phasors are orthogonal over a unit cell area and this implies the Floquet modes are independent and do not couple. Mathematically, this can be expressed using inner product notation [58]

$$\begin{aligned}\langle\psi_{nm}, \psi_{uv}\rangle_{A_{uc}} &= \iint_{A_{uc}} \psi_{nm}\psi_{uv}^{*}\, dxdy \\ &= A_{uc}\delta_{nu}\delta_{mv} = \begin{cases} A_{uc} & \text{when } n = u \ \ \& \ \ m = v \\ 0 & \text{otherwise} \end{cases}\end{aligned} \tag{A.36}$$

A4.1:TM Modes

Transverse magnetic (TM) wave has magnetic field intensity perpendicular to the direction of propagation, while the electric field intensity lies on the plane in the direction of propagation. The longitudinal scalar component of electric field can be cast as [58]

$$E_{z_{nm}}(x,y) = \frac{k_{t_{nm}}}{\beta_{z_{nm}}}\psi_{nm}(x,y) \tag{A.37}$$

Thus, the transverse components can be determined by using the transverse gradient operator, ∇_t for the longitudinal component of (A.37) [58]

$$\vec{E}_{t_{nm}}(x,y) = -j\frac{\beta_{nm}}{k_{t_{nm}}^2}\nabla_t E_{z_{nm}} = \vec{u}_{1nm}\psi_{nm}(x,y) \tag{A.38}$$

$$\vec{H}_{t_{nm}}(x,y) = -j\frac{\omega\epsilon}{k_{t_{nm}}^2}\hat{z}\times\nabla_t E_{z_{nm}} = Y_{1_{nm}}\hat{z}\times\vec{u}_{1nm}\psi_{nm}(x,y) \tag{A.39}$$

where, $\vec{u}_{1nm} = \left(\hat{x}k_{tx} + \hat{y}k_{ty}\right)/\left|\vec{k}_{t_{nm}}\right|$ is the unit vector of the transverse TM components and $Y_{1_{nm}} = k\eta/\beta_{nm}$ is the TM modal admittance associated with the Floquet space harmonic [58].

A4.2: TE Modes

Transverse electric (TE) wave has electric field intensity perpendicular to the direction of propagation, while the magnetic field intensity lies on the plane in the direction of propagation. The longitudinal scalar component of magnetic field can be written as [58]

$$H_{z_{nm}}(x,y) = \frac{\eta k_{t_{nm}}}{k}\psi_{nm}(x,y) \tag{A.40}$$

In a similar manner demonstrated for TM modes, the transverse components of the TE modes can be solve as [58]

$$\vec{E}_{t_{nm}}(x,y) = -j\frac{\omega\mu}{k_{t_{nm}}^2}\hat{z}\times\nabla_t H_{z_{nm}} = \vec{u}_{2nm}\psi_{nm}(x,y) \tag{A.41}$$

$$\vec{H}_{t_{nm}}(x,y) = -j\frac{\beta_{nm}}{k_{t_{nm}}^2}\nabla_t H_{z_{nm}} = Y_{2_{nm}}\hat{z}\times\vec{u}_{2nm}\psi_{nm}(x,y) \tag{A.42}$$

where, $\vec{u}_{2nm} = \left(\hat{y}k_{tx} - \hat{x}k_{ty}\right)/\left|\vec{k}_{t_{nm}}\right|$ is the unit vector of the tangential TE components and $Y_{2_{nm}} = \eta/k\beta_{nm}$ is the TE modal admittance associated with the Floquet space harmonic [58].

The scattered waves from the periodic array as well as the incident waves can be expressed as summation of vector Floquet harmonics (n, m) that include both transverse electric (TE) and transverse magnetic (TM) components. Therefore, the electric and magnetic fields can have form [58]

$$\vec{E}(x,y,z) = \sum_{vnm} a_{vnm}\psi_{nm}(x,y)e^{\pm jk_{z_{nm}}}\vec{u}_{vnm} \tag{A.43a}$$

$$\vec{H}(x,y,z) = \mp \sum_{vnm} Y_{vnm} a_{vnm} \psi_{nm}(x,y) e^{\pm jk_{z_{nm}}} (\hat{z} \times \vec{u}_{vnm}) \tag{A.43b}$$

The notation a_{vnm} represent the amplitude of the Floquet harmonic (n, m) mode, while Y_{vnm} symbolizes the Floquet wave admittance of (n, m) mode. For brevity, the triple summation symbol has been reduce to one as shown in equation (A.43). The index v introduced in equation (A.43) only takes the value 1 and 2, which stands for TM and TE mode respectively. Equally important, the $\pm$ sign designate the wave propagation direction. Specifically, negative sign denote the wave travelling in the positive z direction, while positive sign denote wave travelling in the negative direction [58].

Appendix B: Generalized Scattering Matrix (GSM) for Multilayer FSS

B1: GSM Cascading Rule

In this subsection, formulation for cascading two GSM layer is derived. This formula can be applied repeatedly to compute the entire GSM for a multilayer periodic structure that may consist of several periodic arrays and dielectric slabs. However, in order to employ this formulation, the periodicities and lattice arrangement of the periodic arrays should be identical to ensure the Floquet modal vector function can be applied through all the layers. To this end, consider two layers A and B shown in Figure B.1. Assume N_1 and N_2number of modes are taken into account at port 1 and port 2 of layer A respectively. While, M_2 is the number of modes in port 2 of layer B [59]. The GSM for each layer can be expressed as [59]

$$\begin{bmatrix} a_1^- \\ a_2^- \end{bmatrix} = \begin{bmatrix} [S_{A_{11}}] & [S_{A_{12}}] \\ [S_{A_{21}}] & [S_{A_{22}}] \end{bmatrix} \begin{bmatrix} a_1^+ \\ a_2^+ \end{bmatrix} \tag{B.1}$$

$$\begin{bmatrix} b_1^- \\ b_2^- \end{bmatrix} = \begin{bmatrix} [S_{B_{11}}] & [S_{B_{12}}] \\ [S_{B_{21}}] & [S_{B_{22}}] \end{bmatrix} \begin{bmatrix} b_1^+ \\ b_2^+ \end{bmatrix} \tag{B.2}$$

The goal is to determine the composite GSM that consist of layer A and layer B [59]

$$\begin{bmatrix} a_1^- \\ b_2^- \end{bmatrix} = \begin{bmatrix} [S_{AB_{11}}] & [S_{AB_{12}}] \\ [S_{AB_{21}}] & [S_{AB_{22}}] \end{bmatrix} \begin{bmatrix} a_1^+ \\ b_2^+ \end{bmatrix} \tag{B.3}$$

Expanding algebraically for the matrices in (B.1) and (B.2) yield the following expressions [59]

$$[a_1^-] = [S_{A_{11}}][a_1^+] + [S_{A_{12}}][a_2^+] \tag{B.4}$$

$$[a_2^-] = [S_{A_{21}}][a_1^+] + [S_{A_{22}}][a_2^+] \tag{B.5}$$

$$[b_1^-] = [S_{B_{11}}][b_1^+] + [S_{B_{12}}][b_2^+] \tag{B.6}$$

$$[b_2^-] = [S_{B_{21}}][b_1^+] + [S_{B_{22}}][b_2^+] \tag{B.7}$$

In order to cascade both GSM, the number of input modes on layer B must be equal to the number of output modes from layer A. Hence, the following two conditions must be satisfied [59]

$$[a_2^-] = [b_1^+] \tag{B.8}$$

$$[a_2^+] = [b_1^-] \tag{B.9}$$

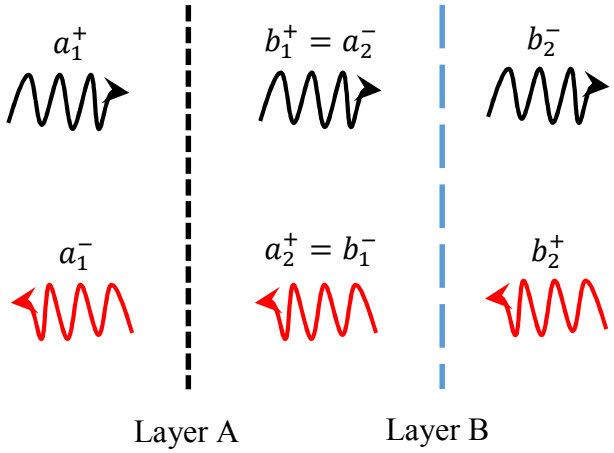

Figure B.1: Incident, reflected, and transmitted voltage vectors of two cascaded layers [59].

Based on the aforementioned two conditions, using equations (B.4) – (B.7), $[a_2^+]$ can be expressed in terms of $[a_1^+]$ and $[b_2^+]$ [59]

$$[a_2^+] = \left[I - S_{B_{11}}S_{A_{11}}\right]^{-1}\left[S_{B_{11}}\right]\left[S_{A_{21}}\right][a_1^+] + \left[S_{A_{12}}\right]\left[I - S_{B_{11}}S_{A_{11}}\right]^{-1}\left[S_{B_{12}}\right][b_2^+] \tag{B.10}$$

The notation I in equation (B.10) represents identity matrix of order $(N_2 \times N_2)$. Subsequently, substitute equation (B.10) for $[a_2^+]$ in equation (B.4) yield [59]

$$\begin{aligned}[a_1^-] = \Big(\left[S_{A_{11}}\right] + \left[S_{A_{12}}\right]\left[I - S_{B_{11}}S_{A_{11}}\right]^{-1}\left[S_{B_{11}}\right]\left[S_{A_{21}}\right]\Big)[a_1^+] \\ + \left[S_{A_{12}}\right]\left[I - S_{B_{11}}S_{A_{11}}\right]^{-1}\left[S_{B_{12}}\right][b_2^+]\end{aligned} \tag{B.11}$$

The expression in (B.11) consist of terms $[a_1^+]$ and $[b_2^+]$, which represent the incident voltage vectors at both ports for the overall GSM. Therefore, the two sub-matrices $[S_{11}]$ and $[S_{21}]$ of the combined GSM can be deduced from (B.11) such that [59]

$$\left[S_{AB_{11}}\right] = \left[S_{A_{11}}\right] + \left[S_{A_{12}}\right]\left[I - S_{B_{11}}S_{A_{11}}\right]^{-1}\left[S_{B_{11}}\right]\left[S_{A_{21}}\right] \tag{B.12}$$

$$[S_{AB_{12}}] = [S_{A_{12}}][I - S_{B_{11}}S_{A_{11}}]^{-1}[S_{B_{12}}] \tag{B.13}$$

In a similar manner, the remaining two sub-matrices $[S_{12}]$ and $[S_{22}]$ are found as [59]

$$[S_{AB_{21}}] = [S_{B_{21}}][I - S_{A_{22}}S_{B_{11}}]^{-1}[S_{A_{21}}] \tag{B.14}$$

$$[S_{AB_{22}}] = [S_{B_{22}}] + [S_{B_{21}}][I - S_{A_{22}}S_{B_{11}}]^{-1}[S_{A_{22}}][S_{B_{12}}] \tag{B.15}$$

B2: Building Blocks for GSM Analysis

Fundamental building blocks of GSM for periodic array, dielectric layer and dielectric interfaces are important for the analysis of multilayer FSS structures. In this subsection, the GSM of these building blocks are discussed [59].

B2.1: FSS Array

The procedures to compute the GSM for a FSS array is only consider EFIE case in this subsection. However, the method described here can be extended to MFIE case as well. In what follows, determined currents coefficients of the FSS array can be utilized in to obtain the reflected and transmitted field amplitudes in region A and B respectively. A scattering coefficient is defined as the projection of total reflected and transmitted fields on to the total incident field direction [58]. To illustrate, assuming plane wave incidence, which can be expressed as

$$\begin{aligned}\vec{E}^i_{total} &= E^i_x\hat{x} + E^i_y\hat{y} + E^i_z\hat{z} \\ &= \psi_{00}\exp\left(-jk_{z_{00}}z\right)\left(B^i_x\hat{x} + B^i_y\hat{y} + B^i_z\hat{z}\right) = \vec{E}^i_{tan} + \vec{E}^i_z\hat{z}\end{aligned} \tag{B.16}$$

The incident tangential electric fields can be expressed as the superposition of TE and TM mode as [58]

$$\vec{E}^i_t = \sum_{v=1}^{2} I_{v00}\psi_{00}\exp(-jk_{z00}z)\,\vec{u}_{v00} \tag{B.17}$$

Following the framework in [58], the direction of the incident field is confined to the y-z plane only, which implies that

$$\left(B_y^i\right)^2 + \left(B_z^i\right)^2 = 1 \tag{B.18}$$

Thus, from the divergence condition, whereby $\hat{k} \cdot \vec{E}_t^i = 0$, the incident y-component can be expressed as [58]

$$B_y^i = \frac{\cos\theta_i}{\sqrt{\cos^2\theta_i + \sin^2\theta_i \sin\phi_i}} \tag{B.19}$$

Subsequently, the z-component of the incident field can be found as [58]

$$B_z^i = \frac{\sin\theta_i \sin\phi_i}{\sqrt{\cos^2\theta_i + \sin^2\theta_i \sin\phi_i}} \tag{B.20}$$

Hence, by expanding equation (B.17) and compare to equation (B.16), one will arrive [58]

$$\begin{bmatrix} I_{100} \\ I_{200} \end{bmatrix} = \begin{bmatrix} u_{y_{100}} & -u_{x_{200}} \\ -u_{y_{100}} & u_{x_{200}} \end{bmatrix} \begin{bmatrix} 0 \\ B_{y_i} \end{bmatrix} \tag{B.21}$$

For the case of pure TE incidence, the applied spherical angles are $\theta_i = \phi_i = 0°$. Thus, for a (n,m) propagation mode, the total reflected field, $\vec{E}_{total}^r$ and transmitted field $\vec{E}_{total}^t$ can be expressed as [58]

$$\vec{E}_{total}^r = \psi_{nm}(x,y) e^{jk_{nm}z}\left(R_x^r \hat{x} + R_y^r \hat{y} + R_z^r \hat{z}\right) \tag{B.22}$$

$$\vec{E}_{total}^t = \psi_{nm}(x,y) e^{-jk_{nm}z}\left(T_x^t \hat{x} + T_y^t \hat{y} + T_z^t \hat{z}\right) \tag{B.23}$$

The scalar components *R* and *T* in equations (B.22) – (B.23) can be computed by solving the EFIE or MFIE. To illustrate, consider the *x*-component correspond to the reflected field of (B.22), thus $R_x^r = R_{vnm} u_{x_{vnm}}$. Subsequently, following the definition of scattering coefficient mentioned above, the co-polar reflection and transmission coefficient for a pure TE incidence can be expressed as [58]

$$R_{TE}^{co} = R_x^r B_{x_{TE}}^i + R_y^r B_{y_{TE}}^i + R_z^r B_{z_{TE}}^i \tag{B.24}$$

$$T_{TE}^{co} = R_x^T B_{x_{TE}}^i + R_y^T B_{y_{TE}}^i + R_z^T B_{z_{TE}}^i \tag{B.25}$$

While, the cross-polar component of the scattered fields can be compute by defining a unit vector, $B_\perp$, which is perpendicular to the incident field B_i [58]

$$\vec{B}_{\perp} = B_i \times \hat{k}_i = B_{x_{\perp}}\hat{x} + B_{y_{\perp}}\hat{y} + B_{z_{\perp}}\hat{z} \tag{B.26}$$

where,

$$B_{x_{\perp}} = \cos\theta_i\, \beta_y^i - \sin\theta_i \sin\phi_i \beta_z^i \tag{B.27}$$

$$B_{y_{\perp}} = \sin\theta_i \cos\phi_i\, \beta_y^i - \cos\theta_i\, \beta_x^i \tag{B.28}$$

$$B_{z_{\perp}} = \sin\theta_i \sin\phi_i\, \beta_z^i - \sin\theta_i \cos\phi_i\, \beta_y^i \tag{B.29}$$

In a similar manner, the cross-polar scattering coefficient can be cast as [58]

$$R_{TE}^{cx} = R_x^r B_{x\perp} + R_y^r B_{y\perp} + R_z^r B_{z\perp} \tag{B.30}$$

$$T_{TE}^{cx} = T_x^t B_{x\perp} + T_y^t B_{y\perp} + T_z^t B_{z\perp} \tag{B.31}$$

Since both TE and TM harmonics may be incident, while the FSS surface allows coupling of energy from one polarization into another, there will be four transmission and four reflection coefficients associated with each pair of incident and reflected harmonics [114]. Thus, for a TM plane wave incidence the applied spherical angles are $\theta_i = 0°$, $\phi_i = 90°$. Similarly, the co-polar reflection and transmission coefficients due to pure TM incidence can be expressed as [58]

$$R_{TM}^{co} = E_x^R B_{x_{TM}}^i + E_y^R B_{y_{TE}}^i + E_z^R B_{z_{TE}}^i \tag{B.32}$$

$$T_{TM}^{co} = E_{x_T} B_{x_{i_{TM}}} + E_{y_T} B_{y_{i_{TM}}} + E_{z_T} B_{z_{i_{TM}}} \tag{B.33}$$

Similarly, for cross-polar reflection and transmission coefficient with respect to TM incidence can be written as [58]

$$R_{TM}^{cx} = E_x^r B_{x\perp} + E_y^r B_{y\perp} + E_z^r B_{z\perp} \tag{B.34}$$

$$T_{TM}^{cx} = E_x^t B_{x\perp} + E_y^t B_{y\perp} + E_z^t B_{z\perp} \tag{B.35}$$

Therefore, the sub-matrices $[S_{11}]$ and $[S_{21}]$ for the FSS array can be expressed as

$$[S_{11}] = \begin{bmatrix} [R_{TE}^{co}] & [R_{TM}^{cx}] \\ [R_{TE}^{cx}] & [R_{TM}^{co}] \end{bmatrix} \tag{B.36}$$

$$[S_{21}] = \begin{bmatrix} [T_{TE}^{co}] & [T_{TM}^{cx}] \\ [T_{TE}^{cx}] & [T_{TM}^{co}] \end{bmatrix} \quad \text{(B.37)}$$

While, the other two sub-matrices $[S_{22}]$ and $[S_{12}]$ can be computed in a similar manner following the method described above. One important note to take into account is that $[S_{11}] \neq [S_{22}]$ and $[S_{21}] \neq [S_{12}]$ for the general case of a FSS lies between two infinite regions of dissimilar medium.

B2.2: Dielectric Layer

An isotropic and homogeneous dielectric slab of thickness, *d* with relative permittivity, ϵ_r is shown in Figure B.2. Assume that N_1 and N_2 number of modes consider at port 1 and port 2 respectively. If the dielectric slab is uniform and constant, propagating waves $[a_1^+]$ that traverses from port 1 through the medium experience no changes. This implies the propagating waves experience no reflection, i.e. $[a_2^+] = [a_1^-] = [0]$. Therefore, the sub-matrix $[S_{11}]$ must be a null matrix, that is to say, $[S_{11}] = [0]$. Similarly, the same situation applies when incident modes travel from port 2 would result in $[a_1^+] = [a_2^-] = [0]$, and therefore $[S_{22}] = [0]$ [59].

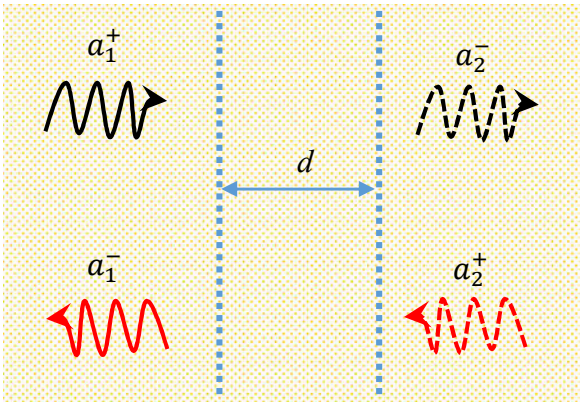

Figure B.2: Travelling waves did not undergo any changes in a dielectric layer of thickness *d*, thus the propagating modes suffer a phase delay only, while evanescent modes are attenuated [59].

Sub-matrix $[S_{21}]$ can be written as [59]

$$[a_2^-] = [S_{21}][a_1^+] \quad \text{(B.38)}$$

The normalized Floquet modal voltage at the terminal ports are travelling waves. Therefore, the waves at the terminal ports are related as [59]

$$a_2^-(k) = a_1^+(k)\exp(-j\beta_k d) \tag{B.39a}$$

$$a_1^-(k) = a_2^+(k)\exp(-j\beta_k d) \tag{B.39b}$$

where $a_2^{\pm}(k)$ and $a_1^{\pm}(k)$ are the k^{th} modal voltages at the output and input ports respectively, while β_k corresponds to the k^{th} mode propagation constant. The propagating modes experiences a phase shift, while the evanescent modes are attenuated since β_k is imaginary. If the thickness of the slab is sufficiently large, the evanescent modes coming from one of terminal port are attenuated entirely and these modes do not reach the other terminal port, thus they can be neglected. Hence, based on equations (B.38) and (B.39) the sub-matrix $[S_{21}]$ can be deduce as [59]

$$[S_{21}] = \begin{bmatrix} p_1 & 0 & 0 & \dots & 0 \\ 0 & p_2 & 0 & \cdots & 0 \\ 0 & 0 & p_3 & \dots & 0 \\ \vdots & \vdots & \vdots & \ddots & \vdots \\ 0 & 0 & 0 & \dots & \ddots \end{bmatrix} \tag{B.40}$$

which is a diagonal matrix of order $N_2 \times N_1$. The diagonal elements p_k are given by [59]

$$p_k = \exp(-j\beta_k d) \tag{B.41}$$

Similarly, $[S_{12}]$ is also a diagonal matrix of order $N_1 \times N_2$ with p_k as diagonal elements. Therefore, the overall GSM for a dielectric slab of thickness, d can be expressed as [59]

$$\begin{bmatrix} a_1^- \\ a_2^- \end{bmatrix} = \begin{bmatrix} [0] & [S_{12}] \\ [S_{21}] & [0] \end{bmatrix} \begin{bmatrix} a_1^+ \\ a_2^+ \end{bmatrix} \tag{B.42}$$

B2.3: Dielectric Interface

Without loss of generality, consider two different isotropic and homogenous dielectric medium with relative permittivity ϵ_{r_1} and ϵ_{r_2} respectively. The dielectrics are bonded at z = 0 plane as depicted in Figure B.3. Assume k^{th} Floquet harmonic impending from z < 0, thus at interface z = 0, the total Floquet modal voltage, v and current, i of the k^{th} harmonic are [59]

$$v(k) = a_1^+(k) + a_1^-(k) \tag{B.43}$$

$$i(k) = \frac{a_1^+(k)}{Z_{F1}(k)} - \frac{a_1^-(k)}{Z_{F1}(k)} \tag{B.44}$$

where, $Z_{F1}(k)$ is characteristic impedance correspond to the k^{th} Floquet harmonic at medium 1. However, the total voltage and current at the interface are related to the characteristic impedances of k^{th} Floquet harmonic at medium 2, namely $Z_{F2}(k)$, which can be obtain as a ratio of [59]

$$\frac{v(k)}{i(k)} = Z_{F2}(k) = Z_{F1}(k)\frac{a_1^+(k) + a_1^-(k)}{a_1^+(k) - a_1^-(k)} \tag{B.45}$$

Solving algebraically from (B.45) to obtain the ratio $a_1^-(k)/a_1^+(k)$ yield the reflection coefficient of the mode incident from medium 1 to medium 2 [59]

$$\frac{a_1^-(k)}{a_1^+(k)} = \Gamma_{21}(k) = \frac{Z_{F2}(k) - Z_{F1}(k)}{Z_{F2}(k) + Z_{F1}(k)} \tag{B.46}$$

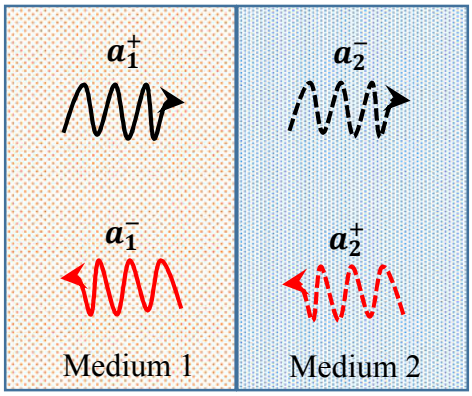

Figure B.3: Incident and reflected voltage vectors at the interface of two dielectric medium [59].

If there are N_1 number of Floquet modes incident at the interface, the sub-matrix $[S_{11}]$ for the interface is therefore [59]

$$[S_{11}] = \begin{bmatrix} \Gamma_{21}(1) & 0 & 0 & \cdots & 0 \\ 0 & \Gamma_{21}(2) & 0 & \cdots & 0 \\ 0 & 0 & 0 & \cdots & 0 \\ \cdots & \cdots & \cdots & \cdots & \cdots \\ 0 & 0 & 0 & \cdots & \Gamma_{21}(N_1) \end{bmatrix} \tag{B.47}$$

which is a diagonal matrix of order $N_1 \times N_1$. The non-diagonal terms are zero by virtue of no couplings between Floquet modes at the interface, assuming that TEz and TMz types of modes are used. Thus, equation (B.43) can be rewritten as [59]

$$v(i) = [1 + \Gamma_{21}(i)]a_1^+(i) \tag{B.48}$$

If medium 2 is infinite extend, this suggest that $[a_2^+] = 0$, because the output port is match terminated. The modal voltage at the interface must be continuous, this implies the total voltage before and after the interface must be the same, i.e. $v(i) = a_2^-(i)$. If N_2 number of modes are consider at port 2, it can be deduce that sub-matrix $[S_{21}]$ can be express as [59]

$$[S_{21}] = \begin{bmatrix} 1+\Gamma_{21}(1) & 0 & 0 & \dots & 0 \\ 0 & 1+\Gamma_{21}(2) & 0 & \cdots & 0 \\ 0 & 0 & 1+\Gamma_{21}(3) & \dots & 0 \\ \cdots & \cdots & \cdots & & \cdots \\ 0 & 0 & 0 & \cdots & \dots \end{bmatrix} \tag{B.49}$$

which, is another diagonal matrix of order $N_2 \times N_1$. From (B.46), it can be deduce that the reflection coefficients looking from port 2 is [59]

$$\Gamma_{12}(i) = -\Gamma_{21}(i) \tag{B.50}$$

Therefore, the remaining sub-matrices $[S_{22}]$ and $[S_{12}]$ at the interface of two different dielectrics are obtain as [59]

$$[S_{22}] = \begin{bmatrix} -\Gamma_{21}(1) & 0 & 0 & \cdots & 0 \\ 0 & -\Gamma_{21}(2) & 0 & \cdots & 0 \\ 0 & 0 & 0 & \cdots & 0 \\ \cdots & \cdots & \cdots & \cdots & \cdots \\ 0 & 0 & 0 & \dots & -\Gamma_{21}(N_2) \end{bmatrix} \tag{B.51}$$

$$[S_{12}] = \begin{bmatrix} 1-\Gamma_{21}(1) & 0 & 0 & \dots & 0 \\ 0 & 1-\Gamma_{21}(2) & 0 & \cdots & 0 \\ 0 & 0 & 1-\Gamma_{21}(3) & \dots & 0 \\ \cdots & \cdots & \cdots & & \cdots \\ 0 & 0 & 0 & \cdots & \dots \end{bmatrix} \tag{B.52}$$

References

[1] P. F. Goldsmith, “Quasi-Optical Techniques,” *Proc. IEEE*, vol. 80, no. 11, pp. 1729–1747, 1992.

[2] P. Besso, M. Bozzi, L. Perregrini, L. S. Drioli, and W. Nickerson, “Deep-space antenna for Rosetta mission: Design and testing of the six band dichroic mirror,” *IEEE Trans. Antennas Propag.*, vol. 51, no. 3, pp. 388–394, Mar. 2003.

[3] R. J. Martin and D. H. Martin, “Quasi-optical antennas for radiometric remote-sensing,” *Electron. Commun. Eng. J.*, vol. 8, no. 1, pp. 37–48, Feb. 1996.

[4] D. L. Woolard, E. R. Brown, M. Pepper, and M. Kemp, “Terahertz frequency sensing and imaging: A time of reckoning future applications?,” *Proc. IEEE*, vol. 93, no. 10, pp. 1722–1743, 2005.

[5] K. B. Cooper *et al.*, “Penetrating 3-D imaging at 4- and 25-m range using a submillimeter-wave radar,” *IEEE Trans. Microw. Theory Techn.*, vol. 56, no. 12, pp. 2771–2778, 2008.

[6] N. Llombart, K. B. Cooper, R. J. Dengler, T. Bryllert, G. Chattopadhyay, and P. H. Siegel, “Time-delay multiplexing of two beams in a terahertz imaging radar,” *IEEE Trans. Microw. Theory Techn.*, vol. 58, no. 7 PART 2, pp. 1999–2007, 2010.

[7] S. A. Kuznetsov *et al.*, “Quasi-optical spectral system for submm-wave radiometry of turbulent plasma,” *2009 Eur. Microw. Conf.*, no. October, pp. 173–176, 2019.

[8] X. Liu, Y. Wang, T. Zhang, L. Gan, J. Nan, and X. Gao, “A Compact Multi-Band Quasi-Optical System for Plasma Detection,” *IEEE Trans. Antennas Propag.*, no. c, pp. 1–1, 2020.

[9] R. Cahill, I. M. Sturland, J. W. Bowen, E. A. Parker, A. C. De Lima, and K. Ct, “Frequency Selective Surfaces For Millimetre And Submilimetre Wave Quasi Optical Demultiplexing,” *Int. J. Infrared Millimeter Waves*, vol. 14, no. 9, Jul. 1993.

[10] R. Dickie *et al.*, “Submillimeter wave frequency selective surface with

polarization independent spectral responses," *IEEE Trans. Antennas Propag.*, vol. 57, no. 7, pp. 1985–1994, Jul. 2009.

[11] B. A. Munk, "Frequency Selective Surfaces: Theory and Design," *New York*, p. 416, 2000.

[12] N. Marcuvitz, *Waveguide Handbook*. The Institution of Engineering and Technology, 1986.

[13] A. M. Melo *et al.*, "Metal mesh resonant filters for terahertz frequencies," *Appl. Opt.*, vol. 47, no. 32, pp. 6064–6069, 2008.

[14] A. C. de C. Lima and E. A. Parker, "Narrow Bandpass Single Layer Frequency Selective Surfaces," *Electron. Lett.*, vol. 29, no. 8, pp. 1–2, 1993.

[15] J. Y. Lee and S. N. Hwang, "A high-gain boost converter using voltage-stacking cell," *Electron. Lett.*, vol. 53, no. 10, pp. 663–665, 2017.

[16] C. Mateo-Segura, G. Goussetis, and A. P. Feresidis, "Resonant effects and near-field enhancement in perturbed arrays of metal dipoles," *IEEE Trans. Antennas Propag.*, vol. 58, no. 8, pp. 2523–2530, 2010.

[17] T. R. Schimert, A. J. Brouns, C. H. Chan, and R. Mittra, "Investigation of Millimeter-Wave Scattering From Frequency Selective Surfaces," *IEEE Trans. Microw. Theory Techn.*, vol. 39, no. 2, pp. 315–322, 1991.

[18] V. D. Agrawal and W. A. Imbriale, "Design of a Dichroic Cassegrain Subreflector," *IEEE Trans. Antennas Propag.*, vol. 27, no. 4, pp. 466–473, 1979.

[19] E. Doumanis, G. Goussetis, J. L. Gómez-Tornero, R. Cahill, and V. Fusco, "Anisotropic impedance surfaces for linear to circular polarization conversion," *IEEE Trans. Antennas Propag.*, vol. 60, no. 1, pp. 212–219, Jan. 2012.

[20] J. C. Vardaxoglou and E. A. Parker, "Performance of two tripole arrays as frequency-selective surfaces," *Electron. Lett.*, vol. 19, no. 18, pp. 709–710, 1983.

[21] L. Musa, P. W. B. Au, E. A. Parker, and R. J. Langley, "Sensitivity of Tripole and Calthrop FSS Reflection Bands to Angle of Incidence," *Electron. Lett.*, vol. 25, no. 4, pp. 284–285, 1989.

[22] A. P. Feresidis, G. Apostolopoulos, N. Serfas, and J. C. Vardaxoglou, “Closely coupled metallodielectric electromagnetic band-gap structures formed by double-layer dipole and tripole arrays,” *IEEE Trans. Antennas Propag.*, vol. 52, no. 5, pp. 1149–1158, 2004.

[23] T. K. Wu, “Four-Band Frequency Selective Surface with Double-Square-Loop Patch Elements,” *IEEE Trans. Antennas Propag.*, vol. 42, no. 12, pp. 1659–1663, 1994.

[24] R. J. Langley and E. A. Parker, “Equivalent circuit model for arrays of square loops,” *Electron. Lett.*, vol. 18, no. 7, p. 294, 2007.

[25] R. J. Langley and E. A. Parker, “Double-square frequency-selective surfaces and their equivalent circuit,” *Electron. Lett.*, vol. 19, no. 17, p. 675, 2007.

[26] M. Euler, V. Fusco, R. Cahill, and R. Dickie, “Comparison of frequency-selective screen-based linear to circular split-ring polarisation convertors,” *IET Microwaves, Antennas Propag.*, vol. 4, no. 11, pp. 1764–1772, 2010.

[27] M. Euler, V. Fusco, R. Cahill, and R. Dickie, “325 GHz Single Layer Sub-MillimeterWave FSS Based Split Slot Ring Linear to Circular Polarization Convertor,” *IEEE Trans. Antennas Propag.*, vol. 58, no. 7, pp. 1–3, Jul. 2010.

[28] M. Euler, V. Fusco, R. Dickie, R. Cahill, and J. Verheggen, “Sub-mm wet etched linear to circular polarization fss based polarization converters,” *IEEE Trans. Antennas Propag.*, vol. 59, no. 8, pp. 3103–3106, 2011.

[29] B. A. Munk and R. J. Luebbers, “Reflection Properties of Two-Layer Dipole Arrays,” *IEEE Trans. Antennas Propag.*, vol. 22, no. 6, pp. 766–773, Nov. 1974.

[30] B. A. Munk, R. J. Luebbers, and R. . Fulton, “Transmission Through a Two-Layer Array of Loaded Slots,” *IEEE Trans. Antennas Propag.*, no. 3, pp. 2–7, 1974.

[31] R. Cahill, E. A. Parker, and C. Antonopoulos, “Design of multilayer frequency-selective surface for diplexing two closely spaced channels,” *Microw. Opt. Technol. Lett.*, vol. 8, no. 6, pp. 293–296, Apr. 1995.

[32] C. Antonopoulos, R. Cahill, E. A. Parker, and M. Sturland, “Multilayer

frequency-selective surfaces for millimetre and submillimetre wave applications," *IEE Proc. Microwaves, Antennas Propag.*, vol. 144, no. 6, pp. 415–420, Dec. 1997.

[33] R. Pous and D. M. Pozar, "A Frequency-Selective Surface Using Aperture-Coupled Microstrip Patches," *IEEE Trans. Antennas Propag.*, vol. 39, no. 12, pp. 1763–1769, Dec. 1991.

[34] A. Abbaspour-Tamijani, K. Sarabandi, and G. M. Rebeiz, "Antenna-filter-antenna arrays as a class of bandpass frequency-selective surfaces," *IEEE Trans. Microw. Theory Techn.*, vol. 52, no. 8 I, pp. 1781–1789, Aug. 2004.

[35] G. Q. Luo *et al.*, "Theory and experiment of novel frequency selective surface based on substrate integrated waveguide technology," *IEEE Trans. Antennas Propag.*, vol. 53, no. 12, pp. 4035–4043, 2005.

[36] M. Joumayly and N. Behdad, "A new technique for design of low-profile, second-order, bandpass frequency selective surfaces," *IEEE Trans. Antennas Propag.*, vol. 57, no. 2, pp. 452–459, Feb. 2009.

[37] N. Behdad and M. A. Joumayly, "A generalized synthesis procedure for low-profile, frequency selective surfaces with odd-order bandpass responses," *IEEE Trans. Antennas Propag.*, vol. 58, no. 7, pp. 2460–2464, 2010.

[38] S. Abadi and N. Behdad, "Inductively-Coupled Miniaturized-Element Frequency Selective Surfaces with Narrowband, High-Order Bandpass Responses," *IEEE Trans. Antennas Propag.*, vol. 63, no. 11, pp. 4766–4774, Nov. 2015.

[39] D. S. Wang, P. Zhao, and C. H. Chan, "Design and Analysis of a High-Selectivity Frequency-Selective Surface at 60GHz," *IEEE Trans. Microw. Theory Techn.*, vol. 64, no. 6, pp. 1694–1703, 2016.

[40] N. Llombart, R. J. Dengler, and K. B. Cooper, "Terahertz antenna system for a Near-Video-Rate Radar Imager," *IEEE Antennas and Propagation Magazine*, vol. 52, no. 5, IEEE, pp. 251–259, Oct-2010.

[41] K. B. Cooper, R. J. Dengler, N. Llombart, B. Thomas, G. Chattopadhyay, and P. H. Siegel, "THz imaging radar for standoff personnel screening," *IEEE Trans. THz Sci. Technol.*, vol. 1, no. 1, pp. 169–182, Sep. 2011.

[42] B. Blazquez, K. B. Cooper, and N. Llombart, “Time-delay multiplexing with linear arrays of THz radar transceivers,” *IEEE Trans. THz Sci. Technol.*, vol. 4, no. 2, pp. 232–239, Mar. 2014.

[43] K. Sarabandi and N. Behdad, “A frequency selective surface with miniaturized elements,” *IEEE Trans. Antennas Propag.*, vol. 55, no. 5, pp. 1239–1245, May 2007.

[44] N. Behdad, M. Joumayly, and M. Salehi, “A low-profile third-order bandpass frequency selective surface,” *IEEE Trans. Antennas Propag.*, vol. 57, no. 2, pp. 460–466, 2009.

[45] J.-S. Hong, *Microstrip Filters for RF/Microwave Applications*, 2nd Editio. New Jersey: WILEY, 2011.

[46] M. A. Joumayly and N. Behdad, “A generalized method for synthesizing low-profile, band-pass frequency selective surfaces with non-resonant constituting elements,” *IEEE Trans. Antennas Propag.*, vol. 58, no. 12, pp. 4033–4041, 2010.

[47] D. M. Pozar, *Microwave Engineering*, Third. John Wiley & Sons, Inc., 2005.

[48] O. Luukkonen *et al.*, “Simple and accurate analytical model of planar grids and high-impedance surfaces comprising metal strips or patches,” *IEEE Trans. Antennas Propag.*, vol. 56, no. 6, pp. 1624–1632, Jun. 2008.

[49] A. R. B.M and D. J. Brian, “Finite-Element Analysis of Optical and Microwave Waveguide Problems,” *IEEE Trans. Microw. Theory Techn.*, vol. 32, no. 1, pp. 20–28, Jan. 1984.

[50] M. N. O. Sadiku, “Simple introduction to finite element analysis of electromagnetic problems,” *IEEE Trans. Educ.*, vol. v, no. n, pp. 85–93, 1992.

[51] P. Harms, R. Mittra, and W. Ko, “Implementation of the periodic boundary condition in the finite-difference time-domain algorithm for FSS structures,” *IEEE Trans. Antennas Propag.*, vol. 3, no. 9, pp. 2144–2147, Sep. 1994.

[52] A. Monorchio and R. Mittra, “A Hybrid Finite-Element Finite-Difference Time-Domain (FE/FDTD) Technique for Solving Complex Electromagnetic Problems,” *IEEE Microw. Guid. Wave Lett.*, vol. 8, no. 2, pp. 93–95, 1998.

[53] H. Wolfgang J. R., “The Transmission-Line Matrix Method— Theory and Applications,” *IEEE Trans. Microw. Theory Tech.*, vol. 10, no. 10, pp. 882–893, Oct. 1985.

[54] Y. Xiong, W. Che, D. Wang, Y. Han, and G. Shen, “Internal Network Boundary Condition Incorporated in TLM for Efficiently Modeling Thin Layer of Periodic Structures,” *IEEE Trans. Microw. Theory Techn.*, vol. 64, no. 9, pp. 2697–2707, 2016.

[55] C. Chao-Chun, “Transmission Through a Conducting Screen Perforated Periodically with Apertures,” *IEEE Trans. Microw. Theory Techn.*, vol. 18, no. 9, pp. 627–632, Sep. 1970.

[56] R. Orta, R. Tascone, and R. Zich, “A unified formulation for the analysis of general frequency selective surfaces,” *Electromagnetics*, vol. 5, no. 4, pp. 307–329, 1985.

[57] D. David B., *Computational Electromagnetics for RF and Microwave Engineering*, Second. Cambridge: Cambridge University Press, 2011.

[58] J. C. Vardaxoglou, *Frequency Selective Surfaces: Analysis and Design*. Taunton Sommerset: Research Studies Press Ltd, 1997.

[59] A. K. Bhattacharyya, *Phased Array Antennas: Floquet Analysis, Synthesis, BFNs, and Active Array Systems*. Hoboken, NJ: John Wiley & Sons, Inc., 2006.

[60] C. Wan and J. A. Encinar, “Efficient computation of generalized scattering matrix for analyzing multilayered periodic structures,” *IEEE Trans. Antennas Propag.*, vol. 43, no. 11, pp. 1233–1242, 1995.

[61] R. F. Harrington, *Field Computation by Moment Methods*, IEEE. New York: John Wiley & Sons, Inc.,Publication, 1968.

[62] C. Mateo-Segura and G. Goussetis, “Near and far fields for an doubly periodic array of metal strips,” in *IEEE Antennas and Propagation Symposium*, 2008, pp. 4–7.

[63] D. S. Lockyer, J. C. J. C. Vardaxoglou, and R. A. Simpkin, “Complementary frequency selective surfaces,” *IEE Proc.-Microw. Antennas Propag*, vol. 147, no.

6, p. 501, Dec. 2002.

[64] R. Collin, *Foundations For Microwave Engineering*, Second. McGraw Hill, Inc, 1992.

[65] G. Matthaei, L. Young, and E. M. T. Jones, *Microwave Filters, Impedance-Matching Networks, and Coupling Structures*. 1980.

[66] R. Dickie, R. Cahill, V. Fusco, H. S. Gamble, and N. Mitchell, "THz frequency selective surface filters for earth observation remote sensing instruments," *IEEE Trans. THz Sci. Technol.*, vol. 1, no. 2, pp. 450–461, Nov. 2011.

[67] E. L. Pelton and B. A. Munk, "A Streamlined Metallic Radome," *IEEE Trans. Antennas Propag.*, pp. 799–803, Nov. 1974.

[68] H. Zhou *et al.*, "Filter-antenna consisting of conical FSS radome and monopole antenna," *IEEE Trans. Antennas Propag.*, vol. 60, no. 6, pp. 3040–3045, Jun. 2012.

[69] V. Sanphuang, W. G. Yeo, J. L. Volakis, and N. K. Nahar, "THz transparent metamaterials for enhanced spectroscopic and imaging measurements," *IEEE Trans. THz Sci. Technol.*, vol. 5, no. 1, pp. 117–123, Jan. 2015.

[70] I. Moreno, J. J. Araiza, and M. Avendano-Alejo, "Thin-film spatial filters," *Opt. Lett.*, vol. 30, no. 8, pp. 914–916, Apr. 2005.

[71] H. A. Macleod, *Thin-Film Optical Filters*, Fourth. CRC Press, 2010.

[72] G. Winnewisser, F. T. Lewen, M. Schall, M. Walther, and H. Helm, "Characterization and application of dichroic filters in the 0.1-3-THz region," *IEEE Trans. Microw. Theory Techn.*, vol. 48, no. 4, pp. 744–749, Apr. 2000.

[73] A. Ebrahimi *et al.*, "Second-Order Terahertz Bandpass Frequency Selective Surface with Miniaturized Elements," *IEEE Trans. THz Sci. Technol.*, vol. 5, no. 5, pp. 761–769, Sep. 2015.

[74] R. Dickie, R. Cahill, H. S. Gamble, V. F. Fusco, A. G. Schuchinsky, and N. Grant, "Spatial demultiplexing in the submillimeter wave band using multilayer free-standing frequency selective surfaces," *IEEE Trans. Antennas Propag.*, vol. 53, no. 6, pp. 1904–1911, Jun. 2005.

[75] S. Biber, M. Bozzi, O. Günther, L. Perregrini, and L. P. Schmidt, “Design and testing of frequency-selective surfaces on silicon substrates for submillimeter-wave applications,” *IEEE Trans. Antennas Propag.*, vol. 54, no. 9, pp. 2638–2645, Sep. 2006.

[76] O. Luukkonen, F. Costa, C. R. Simovski, A. Monorchio, and S. A. Tretyakov, “A thin electromagnetic absorber for wide incidence angles and both polarizations,” *IEEE Trans. Antennas Propag.*, vol. 57, no. 10, pp. 3119–3125, Oct. 2009.

[77] F. Costa, A. Monorchio, and G. Manara, “Analysis and design of ultra thin electromagnetic absorbers comprising resistively loaded high impedance surfaces,” *IEEE Trans. Antennas Propag.*, vol. 58, no. 5, pp. 1551–1558, May 2010.

[78] W. Tang, G. Goussetis, H. Legay, and N. J. G. Fonseca, “Efficient synthesis of low-profile angularly-stable and polarization-independent frequency-selective absorbers with a reflection band,” *IEEE Trans. Antennas Propag.*, vol. 63, no. 2, pp. 621–629, Feb. 2015.

[79] S. Abadi and N. Behdad, “Wideband Linear-to-Circular Polarization Converters Based on Miniaturized-Element Frequency Selective Surfaces,” *IEEE Trans. Antennas Propag.*, vol. 64, no. 2, pp. 525–536, Feb. 2016.

[80] R. Wanatabe, “A Novel Polarization-Independent Beam Splitter,” *IEEE Trans. Microw. Theory Techn.*, vol. M, no. 7, pp. 685–689, Jul. 1980.

[81] R. Dickie *et al.*, “Micromachined 300GHz high Q resonant slot frequency selective surface filter,” *IEE Proc.-Microw. Antennas Propag*, vol. 151, no. 1, pp. 31–36, Feb. 2004.

[82] J. R.Cooper, K. Sangkil, and M. M. Tentzeris, “A Novel Polarization-Independent, Free-Space, Microwave Beam Splitter Utilizing an Inkjet-Printed, 2-D Array Frequency Selective Surface,” *IEEE Antennas Wireless Propag. Lett.*, vol. 11, pp. 686–688, 2012.

[83] J. J. Sanz-Fernandez, R. Cheung, G. Goussetis, and C. Mateo-Segura, “Power stored and quality factors in frequency selective surfaces at THz frequencies,” *IEEE Trans. Antennas Propag.*, vol. 59, no. 6 PART 2, pp. 2205–2216, Jun.

2011.

[84] R. Levy, “A Generalized Design Technique for Practical Distributed Reciprocal Ladder Networks,” *IEEE Trans. Microw. Theory Techn.*, vol. 21, no. 8, pp. 519–526, Aug. 1973.

[85] M. Gao, S. Abadi, and N. Behdad, “A Dual-Band, Inductively Coupled Miniaturized-Element Frequency Selective Surface with Higher Order Bandpass Response,” *IEEE Trans. Antennas Propag.*, vol. 64, no. 8, pp. 3729–3734, Aug. 2016.

[86] W. Tang, G. Goussetis, N. J. G. Fonseca, H. Legay, E. Saenz, and P. de Maagt, “Coupled Split-Ring Resonator Circular Polarization Selective Surface,” *IEEE Trans. Antennas Propag.*, vol. 65, no. 9, pp. 4664–4675, Sep. 2017.

[87] R. Orr *et al.*, “Circular polarisation frequency selective surface operating in Ku and Ka band,” *IEEE Trans. Antennas Propag.*, vol. 63, no. 11, pp. 5194–5197, Nov. 2014.

[88] S. Maci, M. Caiazzo, A. Cucini, and M. Casaletti, “A Pole-zero matching method for EBG surfaces composed of a dipole FSS printed on a grounded dielectric slab,” *IEEE Trans. Antennas Propag.*, vol. 53, no. 1, pp. 70–81, Jan. 2005.

[89] G. Goussetis, A. P. Feresidis, and J. Y. C. Vardaxoglou, “Tailoring the AMC and EBG Characteristics of Periodic Metallic Arrays Printed on Grounded Dielectric Substrate,” *IEEE Trans. Antennas Propag.*, vol. 54, no. 1, pp. 82–89, Jan. 2006.

[90] A. P. Feresidis, G. Goussetis, S. Wang, and J. C. Vardaxoglou, “Artificial magnetic conductor surfaces and their application to low-profile high-gain planar antennas,” *IEEE Trans. Antennas Propag.*, vol. 53, no. 1, pp. 209–215, Jan. 2005.

[91] E. Doumanis, G. Goussetis, G. Papageorgiou, V. Fusco, R. Cahill, and D. Linton, “Design of engineered reflectors for radar cross section modification,” *IEEE Trans. Antennas Propag.*, vol. 61, no. 1, pp. 232–239, Jan. 2013.

[92] W. Tang, S. Mercader-Pellicer, G. Goussetis, H. Legay, and N. J. G. Fonseca, “Low-profile compact dual-band unit cell for polarizing surfaces operating in orthogonal polarizations,” *IEEE Trans. Antennas Propag.*, vol. 65, no. 3, pp.

1472–1477, Mar. 2017.

[93] R. Orr, G. Goussetis, V. Fusco, and E. Saenz, “Linear-to-Circular Polarization Reflector with Transmission Band,” *IEEE Trans. Antennas Propag.*, vol. 63, no. 5, pp. 1949–1956, May 2015.

[94] M. Fartookzadeh and S. H. M. Armaki, “Dual-Band Reflection-Type Circular Polarizers Based on Anisotropic Impedance Surfaces,” *IEEE Trans. Antennas Propag.*, vol. 64, no. 2, pp. 826–830, 2016.

[95] R. C. Hall and R. Mittra, “Scattering from a Periodic Array of Resistive Strips,” *IEEE Trans. Antennas Propag.*, vol. 33, no. 9, pp. 1009–1011, Sep. 1985.

[96] M. A. G. Laso *et al.*, “Real-time spectrum analysis in microstrip technology,” *IEEE Trans. Microw. Theory Techn.*, vol. 51, no. 3, pp. 705–717, Mar. 2003.

[97] S. Gupta, S. Abielmona, and C. Caloz, “Microwave analog real-time spectrum analyzer (RTSA) based on the spectral-spatial decomposition property of leaky-wave structures,” *IEEE Trans. Microw. Theory Techn.*, vol. 57, no. 12, pp. 2989–2999, Dec. 2009.

[98] S. Abielmona, S. Gupta, and C. Caloz, “Compressive receiver using a CRLH-based dispersive delay line for analog signal processing,” *IEEE Trans. Microw. Theory Techn.*, vol. 57, no. 11, pp. 2617–2626, Nov. 2009.

[99] B. Nikfal, S. Gupta, and C. Caloz, “Increased group-delay slope loop system for enhanced-resolution analog signal processing,” *IEEE Trans. Microw. Theory Techn.*, vol. 59, no. 6, pp. 1622–1628, Jun. 2011.

[100] S. Gupta, D. L. Sounas, H. Van Nguyen, Q. Zhang, and C. Caloz, “CRLH-CRLH C-section dispersive delay structures with enhanced group-delay swing for higher analog signal processing resolution,” *IEEE Trans. Microw. Theory Techn.*, vol. 60, no. 12, pp. 3939–3949, Dec. 2012.

[101] G. Goussetis, J. L. Gomez-Tornero, A. P. Feresidis, and N. K. Uzunoglu, “Artificial impedance surfaces for reduced dispersion in antenna feeding systems,” *IEEE Trans. Antennas Propag.*, vol. 58, no. 11, pp. 3629–3636, Nov. 2010.

[102] Q. Zhang, D. L. Sounas, and C. Caloz, “Synthesis of cross-coupled reduced-order dispersive delay structures (DDSs) with arbitrary group delay and controlled magnitude,” *IEEE Trans. Microw. Theory Techn.*, vol. 61, no. 3, pp. 1043–1052, Mar. 2013.

[103] Q. Zhang, S. Gupta, and C. Caloz, “Synthesis of Narrowband Reflection-Type Phasers With Arbitrary Prescribed Group Delay,” *IEEE Trans. Microw. Theory Techn.*, vol. 60, no. 8, pp. 2394–2402, Aug. 2012.

[104] Y. J. Cheng *et al.*, “Substrate integrated waveguide (SIW) Rotman lens and its Ka-band multibeam array antenna applications,” *IEEE Trans. Antennas Propag.*, vol. 56, no. 8, pp. 2504–2513, Aug. 2008.

[105] A. Lambrecht, S. Beer, and T. Zwick, “True-time-delay beamforming with a Rotman-lens for ultrawideband antenna systems,” *IEEE Trans. Antennas Propag.*, vol. 58, no. 10, pp. 3189–3195, 2010.

[106] R. Rotman, M. Tur, and L. Yaron, “True Time Delay in Phased Arrays,” *Proc. IEEE*, vol. 104, no. 3, pp. 504–518, Mar. 2016.

[107] W. Tang, P. K. Loo, and G. Goussetis, “Time-delay reflector for time-domain pulse splitting,” *2014 Loughbrgh. Antennas Propag. Conf. LAPC 2014*, no. November, pp. 132–135, 2014.

[108] R. J. Cameron, C. M. Kudsia, and R. R. Mansour, *Microwave Filters for Communication Systems*, First. New Jersey: John Wiley & Sons, Inc., 2007.

[109] T. Henk, “The generation of arbitrary-phase polynomials by recurrence formulae,” *Int. J. Circuit Theory Appl.*, vol. 9, no. 4, pp. 461–478, Oct. 1981.

[110] M. E. Van Valkenburg, *Introduction to Modern Network Synthesis*. John Wiley & Sons, Inc., 1964.

[111] R. Levy, “Theory of Direct-Coupled-Cavity Filters,” *IEEE Trans. Microw. Theory Techn.*, vol. MTT-15, no. 6, pp. 340–348, Jun. 1967.

[112] H. Fernandez Alvarez, M. E. De Cos Gomez, and F. Las-Heras, “Angular Stability of Metasurfaces: Challenges Regarding Reflectivity Measurements,” *IEEE Antennas and Propagation Magazine*, vol. 58, no. 5, pp. 74–81, Oct-2016.

[113] C. A. Balanis, *Advanced Engineering Electromagnetics*, Second. John Wiley & Sons, Inc., 2012.

[114] R. Mittra, C. H. Chan, and T. Cwik, "Techniques for Analyzing Frequency Selective Surfaces-a Review," *Proc. IEEE*, vol. 76, no. 12, pp. 1593–1615, 1988.